UNIVERSITY OF CALIFORNIA,
IRVINE

LHC Searches for Dark Matter and Exotic Resonances

DISSERTATION

submitted in partial satisfaction of the requirements
for the degree of

DOCTOR OF PHILOSOPHY

in Physics

by

Chase Owen Shimmin

Dissertation Committee:
Professor Daniel Whiteson, Chair
Professor Anyes Taffard
Professor Tim M.P. Tait

2016

DEDICATION

To my parents,

Robert and Lynda

for providing me with the opportunity to succeed

TABLE OF CONTENTS

LIST OF FIGURES

LIST OF TABLES

ACKNOWLEDGMENTS

To my loving girlfriend Janet, I would like to express my profound gratitude. Without her support and care I would have never even started my graduate school journey – let alone seen it through to completion. I am also especially indebted to my wonderful parents Robert and Lynda, for allowing me to live at their home and eat all their food.

I also would like to express my appreciation for the entire High Energy Physics group at UC Irvine, whose students, past and present, and faculty foster a collaborative, creative environment where ideas flow and develop into productive research. In particular I thank Mohammad Abdullah, Anthony DiFranzo, Alex Wijangco, and Professor Tim Tait for countless useful, instructive, and entertaining conversations about theory and phenomenology.

Above all, I owe my academic development and successes to my excellent advisor, Professor Daniel Whiteson.

CURRICULUM VITAE

Chase Owen Shimmin

EDUCATION

University of California, Irvine
Doctor of Philosophy in Physics **2016**
Master of Science in Physics **2015**

University of California, Berkeley
Bachelor of the Arts in Mathematics and Physics **2010**

RESEARCH EXPERIENCE

Graduate Research Assistant **2012–2016**
UC Irvine Department of Physics & Astronomy
Supervisor: Prof. Daniel Whiteson

Research Assistant **2008–2011**
UC Berkeley Department of Physics
Supervisor: Prof. Adrian Lee

Undergraduate Student Researcher **2008**
UC Berkeley Department of Physics
Supervisor: Prof. Stuart Freedman

TEACHING EXPERIENCE

Teaching Assistant **2011–2012**
University of California, Irvine

AWARDS & HONORS

Faculty Endowed Fellowship **2016**
School of Physical Sciences, UC Irvine

Webby Award *(with the CRAYFIS collaboration)* **2015**
Mobile Sites/Apps: Experimental & Innovation Category

REFEREED JOURNAL PUBLICATIONS

Boosting low-mass hadronic resonances **2016**
Phys. Rev. D

Search for Dark Matter in Events with Missing Transverse Momentum and a Higgs Boson Decaying to Two Photons in pp Collisions at $\sqrt{s} = 8$ TeV with the ATLAS Detector **2015**
Phys. Rev. Lett.

Observing Ultra-High Energy Cosmic Rays with Smartphones **2016**
Astropart. Phys.

Search for new phenomena in events with a photon and missing transverse momentum in pp collisions at $\sqrt{s} = 8$ TeV with the ATLAS detector **2015**
Phys. Rev. D

Search for new phenomena in events with a Z boson and missing transverse momentum in pp collisions at $\sqrt{s} = 8$ TeV with the ATLAS detector **2014**
Phys. Rev. D

Systematically Searching for New Resonances at the Energy Frontier Using Topological Models **2014**
Phys. Rev. D

Mono-Higgs: a new collider probe of dark matter **2014**
Phys. Rev. D

Collider searches for dark matter in events with a Z boson and missing energy **2012**
Phys. Rev. D

ABSTRACT OF THE DISSERTATION

LHC Searches for Dark Matter and Exotic Resonances

By

Chase Owen Shimmin

Doctor of Philosophy in Physics

University of California, Irvine, 2016

Professor Daniel Whiteson, Chair

In this work, several phenomenological models for extending the Standard Model are presented, with an emphasis on providing a candidate dark matter particle. These models are specifically designed as benchmark signals in two novel search channels proposed for LHC experiments: mono-Z and mono-Higgs. Searches for dark matter production in these newly-proposed channels are then conducted using data from pp collisions at $\sqrt{s} = 8$ TeV recorded by the ATLAS detector. In both cases, the observed measurements are consistent with the predicted Standard Model rates. Therefore, upper limits are derived on the production cross sections of these dark matter models, which are also translated to limits on theoretical parameters specific to each model. Lastly, a method of searching for hadronic resonances with masses in the 20–500 GeV range at the LHC is described in the context of a minimal leptophobic Z' extension to the Standard Model. The feasibility of this search method is investigated assuming a dataset of 4 fb^{-1} of pp collisions in terms of the sensitivity to the Z' coupling parameter. These searches are expected to provide nontrivial limits on the Z' model in regions that have been either only weakly constrained or never probed by direct measurements.

Chapter 1

Introduction

People have always striven to understand the world around them. In the scientific sense, this understanding is achieved through the development of theories. A theory can be thought of as the compilation of intuitions about a subject into a more rigid framework for reasoning. At a minimum, sound scientific theories must be explanatory, but better still are predictive theories, from which implications may be derived that provide new insight about the world. While curiosity alone is often enough to drive the quest for understanding, it has also occasionally proven to be a worthwhile pursuit from a survival or simply a materialistic perspective. The development of the theory of germs led to tremendous advances in health and medicine, while the development of the theory of semiconductor electronics has led to the computerization of our world.

For example, in order to develop agriculture, it is necessary to first understand the phenomenon of seasons. A very simple theory of seasons is that there are four of them occurring in succession, and that one of them is colder and darker than the others. This is not a very predictive theory, and hence does not lead to many deep insights. But when communicated, it at least may improve the chances of agricultural success if it is also empirically observed

that one should wait until after the cold season before planting crops.

A better theory for seasons is that the Earth orbits around the Sun along an elliptical path, and is tilted relative to this path. This theory is much more predictive. We can predict that there are at least two seasons, corresponding to times when the Earth is tilted towards or away from the Sun. We can predict that seasons in the northern hemisphere are different from those in the southern hemisphere. And we can even predict that if the stars are situated at a finite distance from Earth, their apparent positions in the sky should shift due to parallax as the Earth moves along its orbit.

While it is impossible to say *a priori* what kind of discoveries and benefits will result from the development of knowledge, this simple example illustrates a very important notion: deeper and more fundamental understanding can result in surprising and useful conclusions. This is because building new ideas atop fundamental ones is often easier than trying to connect two seemingly disparate concepts.

The study of particle physics is an attempt to understand how the universe operates at the most fundamental level. In this scope, the universe may be defined as spacetime, the matter that occupies it, and the interactions of this matter. The Standard Model (SM) of particle physics, a theory developed over the course of the 20^{th} century, has provided a phenomenally good description of this universe. It is based on a quantum field theory in which matter is described by the excitation of spacetime fields corresponding to each type of matter; interactions arise from nonlinear couplings between these fields. These couplings in turn arise from a set of symmetries, assumed to be fundamental, which affect the fields depending on their defining properties.

Although the SM has been successful in both accurately explaining and predicting many phenomena with great precision, it is known to be an incomplete description of the universe. One major omission is the lack of a quantum-relativistic explanation of the phenomenon

of gravitation. The theory of General Relativity provides the best description of gravity on macroscopic scales in terms spacetime geometry. However, this has so far not been reconciled with the framework of quantum field theory upon which the SM is built.

The SM also neither predicts nor provides an explanation for the observed amount of dark matter in the universe. Dark matter (DM) is a form of matter in the universe that is not comprised of the baryonic or charged leptonic matter described by the SM. Based on great variety of cosmological and astrophysical evidence [1], non-baryonic DM is now believed to comprise a large fraction of the mass-energy of the universe, approximately five times more abundant than baryonic matter [2]. The most compelling evidence for dark matter comes from galactic rotation curves, which demonstrate that the amount of luminous matter contained in galaxies is not sufficient to explain the observed rotational velocities of galaxies. Measurements of the Cosmic Microwave Background are consistent with large amounts of weakly interacting cold dark matter which is nonrelativistic and therefore massive.

Since all other known matter in the universe can be described by particles, it is reasonable to assume also that dark matter is a particle. Moreover, the reason we are able to detect the existence of dark matter is because it is interacting with our world in some way. All of the standing evidence for dark matter is due to its gravitational interactions; if this is the only interaction it will be impossible to probe the particle nature of dark matter in the laboratory, simply because the gravitational force is too feeble. Therefore, it is interesting to ask whether there are additional interactions between dark matter and the particles of the SM.

The body of evidence is consistent with and potentially even favors [3] weakly-interacting dark matter at electroweak mass scales. If interactions such as scattering between dark matter and the particles of the SM do exist, then it must theoretically also be possible to produce dark matter from these SM particles. In particular, if the interacting dark matter particles have mass at or below the TeV-scale, they may be produced in collisions at the

LHC. This is the topic of Chapter 3, which discusses the development and implementation of two novel searches for dark matter production using the ATLAS detector.

Beyond gravity and dark matter, there are other issues with the standard model. For example, the infamous hierarchy problem arises from the improbably fine-tuned cancellation of the very large corrections to the Higgs self-energy against its bare mass which conspires to give the observed Higgs mass of 125 GeV. This is often interpreted as a clue that some additional physical mechanism is missing from the theory which would explain the effect. These and other clues have encouraged the active development of theoretical models for physics beyond the standard model (BSM). One proposed solution is the introduction of Supersymmetry (SUSY), a spacetime symmetry, which when imposed on the standard model results in a spate of new particles called superparters, one for each particle of the standard model. Because of the symmetric relationship of these particles, the Higgs self-energy corrections largely cancel out between each particle and its superpartner.

Many BSM models of physics, such as those based on SUSY, can be very predictive, and have therefore been the basis of well-motivated searches for new particles at particle colliders. However, despite decades of searching, no evidence for these theories has been observed. One model-independent alternative for seeking out BSM physics is to simply look for new particles in places that have not been examined.

A common example of this is seen in the dijet search channel at hadron colliders. In these searches, the distribution of invariant masses for events containing two high-energy hadronic jets is examined. Quite generically, a short-lived massive particle which decays to quarks or gluons would appear in this distribution as a peak atop an otherwise monotonic background. Therefore, each time a new collider is commissioned at higher energy, this channel provides the first-ever direct test for new particles at that energy.

Regrettably, it is not possible to examine arbitrarily high energies due to technological and

financial barriers. In Chapter 4, we identify a relatively low mass region which has not been probed because of technical challenges. A new method to search for BSM particles in this regime is proposed, and the feasibility of conducting such a search at the LHC is explored.

Chapter 2

The LHC and ATLAS

All of the research described in this thesis is based on the successful construction and operation of two amazing feats of engineering, collaboration, and funding: the Large Hadron Collider (LHC) and the ATLAS detector. Thorough overviews of the design of both instruments may be found in Ref. [4] and Ref. [5], respectively. In this chapter, we provide a brief summary of the aspects of each that are relevant to the studies to follow.

2.1 The Large Hadron Collider

The LHC is a hadron accelerator situated 45–170 m beneath a mostly-rural region of France and Switzerland on the outskirts of Geneva. It is built in the existing 26.7 km tunnel that was previously constructed for and occupied by the LEP machine. Comprised of two parallel rings utilizing 1,232 superconducting dipole magnets to bend beams of charged energetic particles, it is capable of colliding the two beams at four intersection points. Each of the ATLAS, CMS, LHCb, and ALICE experiments is located at one of the large underground caverns surrounding these points. At these locations, quadrupole magnets focus the two

beams into a single interaction point, where collisions may be observed at up to 40MHz, the bunch-crossing frequency.

Although the LHC is capable of accelerating and colliding ion beams, the research discussed here focuses on data from the primary operation mode of proton-proton collisions. Protons from the Super Proton Synchrotron (SPS) are injected into the LHC at an energy of 450 GeV, and are then accelerated by 16 superconducting RF cavities (8 per beam) operating at 400 MHz and providing up to 2 MV accelerating voltage each. The maximum design energy for proton beams is 7 TeV, for a colliding beam center of mass energy of $\sqrt{s} = 14$ TeV. As of 2016 it has been operated at a maximum of $\sqrt{s} = 13$ TeV, with significant earlier runs at $\sqrt{s} = 7$ TeV and $\sqrt{s} = 8$ TeV as well. The peak design luminosity of the LHC for proton-proton collisions is $10^{34}\text{cm}^{-2}\text{s}^{-1}$, although as of June 2016, it has exceeded this luminosity.

2.2 The ATLAS Detector

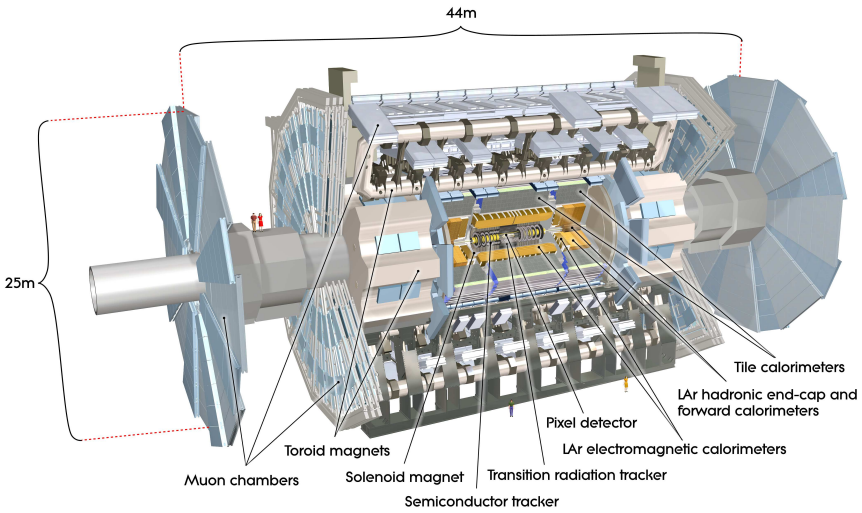

Figure 2.1: Schematic representation of the ATLAS detector. Reproduced from Ref. [5].

The ATLAS detector is a general purpose particle detector designed to observe and withstand

the very high energy and intense fluence of particles produced in collisions provided by the LHC. It has a roughly cylindrical symmetry about the colliding beam axis, which in the standard ATLAS coordinate system defines the z-axis. The x-y plane is transverse to the beam, with azimuthal angles in this plane denoted by ϕ. The angle θ is the polar angle from the beam axis; however, the pseudorapidity $\eta := -\ln\tan(\theta/2)$ is commonly used instead. Angular distances between two objects in an arbitrary plane are often quantified by the pseudo-euclidean metric $\Delta R := \sqrt{\Delta\phi^2 + \Delta\eta^2}$. The symbol p_{T} represents the component of a 3-vector momentum $\mathbf{p}$ which lies in the x-y plane, while the symbol $E_{\mathrm{T}}^{\mathrm{miss}}$ denotes the missing transverse energy. A cut-away view of the ATLAS detector is shown in Figure 2.1.

ATLAS was designed to maximize potential for a diverse program of physics goals at the TeV scale. Perhaps the most notable of these goals was the search for the Higgs boson, which was discovered by ATLAS [6, 7] and CMS [8] in 2012. Given that the mass of the Higgs boson, which greatly affects its experimental signature, was unknown, it was critical that ATLAS be capable of making precise measurements of muons, and electromagnetic and hadronic particles over a broad momentum range. Other motivating physics cases include searches for TeV-scale Supersymmetry (SUSY), exotic bosons such as Z' and W' with masses of up to several TeV, quark compositeness, extra dimensions, and quantum black holes.

A primary topic of this thesis is the search for the production of particle Dark Matter (DM) in collisions at the LHC. If stable DM particles are produced in collisions, they would escape ATLAS without being detected, carrying with them some momentum. Since the protons in the LHC beam are not fundamental particles, the interacting constituents of each collision are actually quarks and gluons (collectively referred to as *partons*). Unlike the protons to which they belong, these particles do not have a definite momentum the z-direction; instead, their longitudinal momentum is a random variable which can only be statistically modeled by parton distribution functions [9]. Because of this incomplete information about the initial state of each LHC collision, the total momentum of invisible particles cannot be extracted

from the rest of the observed event. Instead, we use the fact that the total initial *transverse* momentum of the interacting particles is zero, enabling us to at least calculate the transverse component of the missing momentum, $E_{\mathrm{T}}^{\mathrm{miss}}$.

In order for $E_{\mathrm{T}}^{\mathrm{miss}}$ to be accurately resolved, it is an important design consideration that ATLAS have as close to 4π coverage of the interaction point as possible. This is accomplished by employing a layered design comprising a central cylindrical *barrel* segment sandwiched between two radial *end-cap* segments. The different layers of the detector can be broken into major subcomponents: the Inner Detector, Electromagnetic Calorimeter, Hadronic Calorimeter, and Muon Spectrometer. Each of these components is composed of multiple detector systems, and are discussed in Sections 2.2.2–2.2.4. In addition to these detector systems, a crucial feature of the ATLAS experiment is the design of its magnet system, discussed in Section 2.2.1.

Unfortunately, it is impossible with current technology to process or (permanently) record all of the data from every single collision event observed by ATLAS at rates of up to once every 25 ns. Instead, we must aggressively pare down the data rates by rapidly evaluating events and keeping only the most interesting ones. This is handled by the ATLAS trigger and data acquisition system, described in Section 2.2.5.

Finally, in order to make sense of the interactions observed by the detector, signals from the more than 100 million data channels must be read out and compiled into a representation of the physical particles which may have initiated the observed signals. Practical details about the reconstruction of these physics objects, such as jets, photons, electrons, and muons, are discussed in Section 2.3.

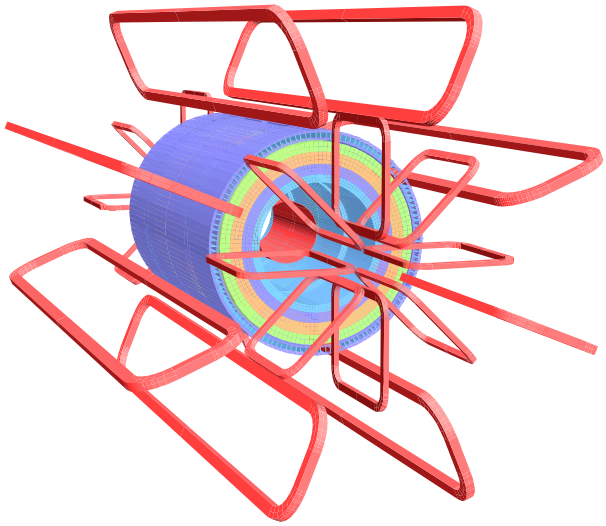

Figure 2.2: Schematic illustration of the ATLAS magnet system. The superconducting coils of the solenoid, barrel toroid, and end-cap toroid magnets are shown in pink. Reproduced from Ref. [5].

2.2.1 Magnet System

The ATLAS magnet system [10] is illustrated schematically in Figure 2.2. The inner detector is entirely enveloped within a superconducting solenoid magnet providing it with an approximately uniform 2 T magnetic field along the z-axis. This magnetic field deflects radially-propagating charged particles so that their momenta may be measured based on the curvature their tracks. The space between the calorimeters and the muon spectrometer contains the barrel and end-cap toroid magnets, a system of superconducting coils providing toroidal magnetic fields of up to 0.5 T and 1 T respectively.

2.2.2 Inner Detector

The inner detector (ID), shown schematically in Figure 2.3, is the closest component of ATLAS to the interaction point. Its purpose is to provide high-efficiency tracking and vertexing for charged particles with p_{T} above approximately 0.5 GeV and within $|\eta| < 2.5$. The design and performance expectations of the ID is described in detail in Ref. [11]; a

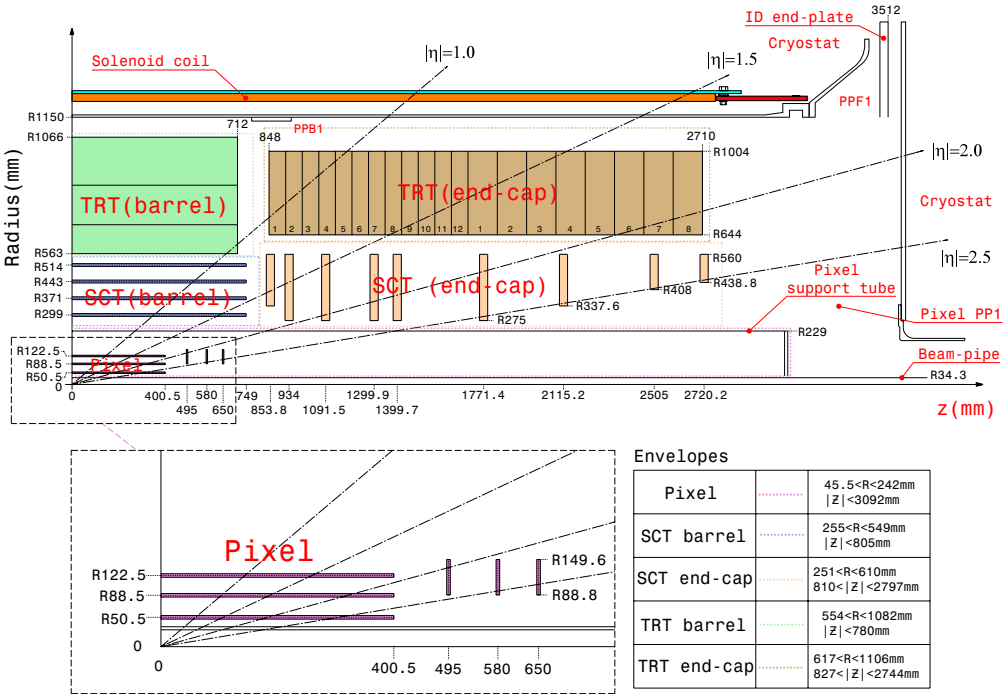

Figure 2.3: Schematic of ID components in the R-z plane demonstrating coverage in η. The IBL, which covers the range $|\eta| < 3$ relative to the interaction point, is not included in this figure. Reproduced from Ref. [5].

summary of recent ID tracking performance in 2015 data is given in [12]. The ID is comprised of three detector systems: a pixel detector, a silicon microstrip tracker, and a transition radiation straw tube tracker; each one further removed from the beam line than the next.

The innermost component is a high-granularity silicon Pixel Detector, initially commissioned with three barrel and three end-cap layers. The nominal size of pixels in these layers is $50\times400\mu\text{m}^2$, although a small fraction are sized $50\times600\mu\text{m}^2$. During the first Long Shutdown (LS1) of the LHC, a new, smaller beampipe was installed and a fourth pixel layer known as the Insertable B-Layer (IBL) [13] was inserted into the center of the existing inner detector. The $50 \times 250\mu\text{m}^2$ IBL pixels are more granular and cover the barrel region $|\eta| < 3.0$. This new layer provides greater precision and efficiency in tracking, especially in the face of higher detector occupancy caused by luminosities which are currently exceeding the original design specification. The IBL adds 6.02 million channels to the inner detector, for a total of 86.4 million pixel channels.

The second component of the ID is the Semi-Conductor Tracker (SCT). It is similar to the Pixel Detector but as it is further removed from the interaction point, it does not require nearly as much spacial resolution to maintain acceptable occupancy. Each SCT module contains 786 active sensor strips that are 80μm wide in the precision (ϕ) direction and 12 cm long in the z direction. The SCT is composed of four layers in the barrel segment and nine layers in each of the end-cap regions, totaling approximately 6.3 million channels. Unlike in the Pixel Detector, SCT modules are mounted in each layer as overlapping pairs oriented at $\pm$20 mrad around an axis normal to their geometrical center. This provides some stereo information in the plane of the sensor strips and enables improved reconstruction of the location of hits in the z–ϕ plane.

The outermost component of the ID is the Transition Radiation Tracker (TRT). This detector is made up of straw-like tubes 4 mm in diameter filled with a Xenon gas mixture threaded through the middle with gold-plated tungsten anode wire. The Al wall of the tube provides the cathode, typically operated at approximately -1.5 kV. These drift chambers have a maximum electron collection time of approximately 48 ns and are capable of discriminating two thresholds: a lower threshold for detecting ionizing particles traversing the tube and a higher threshold for the much stronger signal caused by Xe absorption of transition-radiated photons. In the barrel region, the straws have an active length of up to 71.2 cm and are oriented parallel to the beam axis; therefore, they provide only R–ϕ constraints for tracking hits. In the end-cap region, the straws are oriented radially and provide z–ϕ hits. The TRT contains up to 73 layers of straws in the barrel region and 160 straw planes in the end-cap; a typical central particle track will produce approximately 36 straw hits.

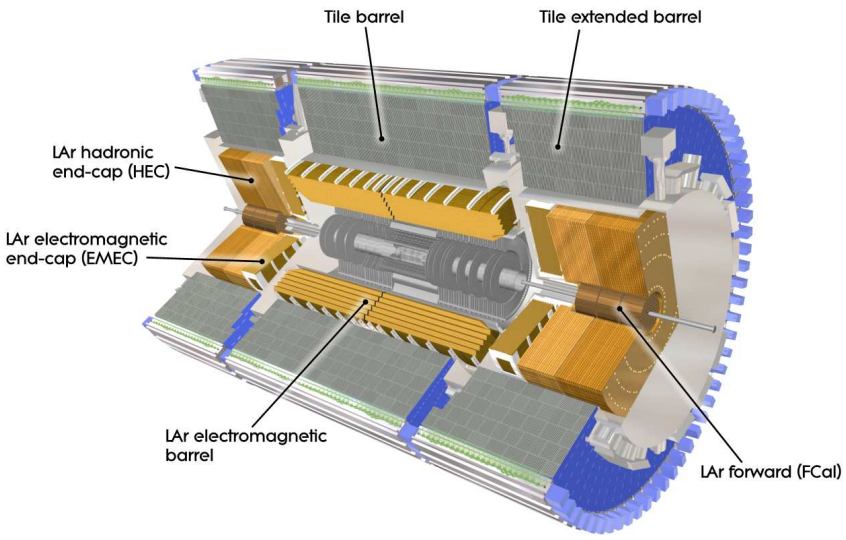

Figure 2.4: Overview of the ATLAS Calorimeter system. Reproduced from Ref. [5].

2.2.3 Calorimeters

The purpose of the ATLAS calorimeter, illustrated in cutaway in Figure 2.4, is to absorb and measure the energies of the particles produced in LHC collisions. In must do this with sufficient resolution and spacial granularity to accurately reconstruct the physical momenta of these particles in order to meet the physics goals of the experiment. To this end, the calorimeter system should ideally stop as many particles as possible (except muons and neutrinos) with energies of up to several TeV within its volume.

The ATLAS calorimeter system is composed of two major calorimeters: the Electromagnetic (EM) Calorimeter and the Hadronic Calorimeter. Additionally, there is a Forward Calorimeter which covers the region nearest the beam line and has integrated EM and hadronic components.

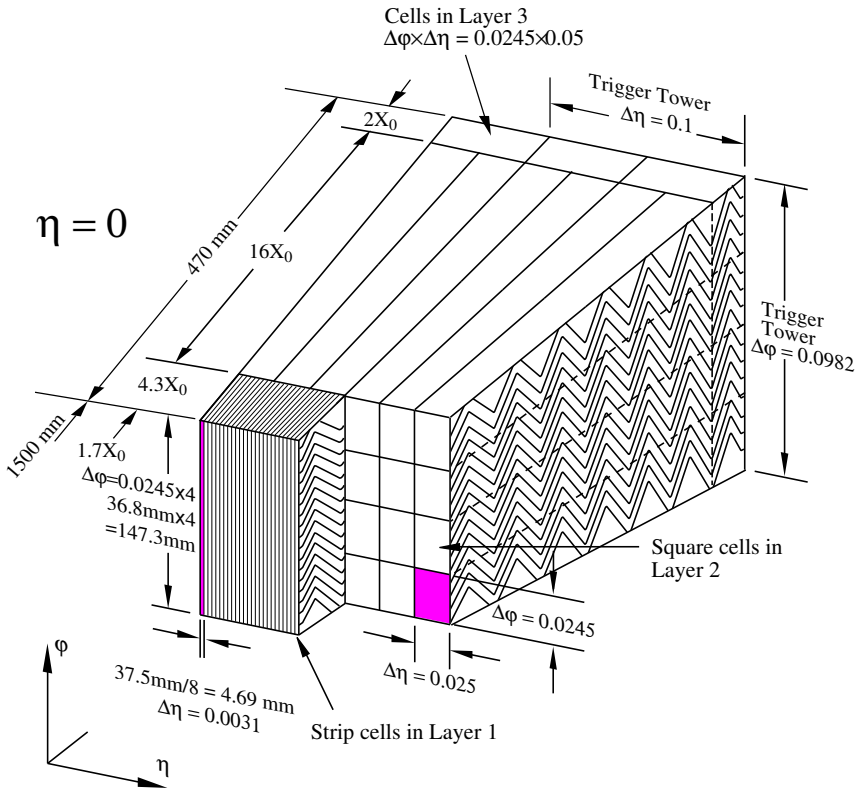

Figure 2.5: A sketch of a barrel module of the EM calorimeter, displaying the accordion structure. Reproduced from Ref. [5].

Electromagnetic Calorimeter

The EM Calorimeter is designed to principally absorb and measure the energies of photons and electrons by inducing electromagnetic cascades. It is a sampling calorimeter based on an accordion-shaped geometry of electrodes and absorbers, illustrated in Figure 2.5. This geometry provides even coverage of ϕ with no gaps, and covers the region $|\eta| < 3.2$. The active material is Liquid Argon (LAr), which fills the 2.1 mm-wide interstices of the electrodes and absorbers. At nominal operating voltage the drift time is about 450 ns. Each module is subdivided into three layers in depth, and each layer's readout cells have a granularity of $\Delta\eta \times \Delta\phi = 0.025 \times 0.025$.

The EM Calorimeter is supplemented by a LAr presampler, located just before the first layer of the calorimeter module. This active layer has a higher granularity than the calorimeter

and is used to help estimate the energy of particles which have begun to shower prior to entry into the calorimeter.

Hadronic Calorimeter

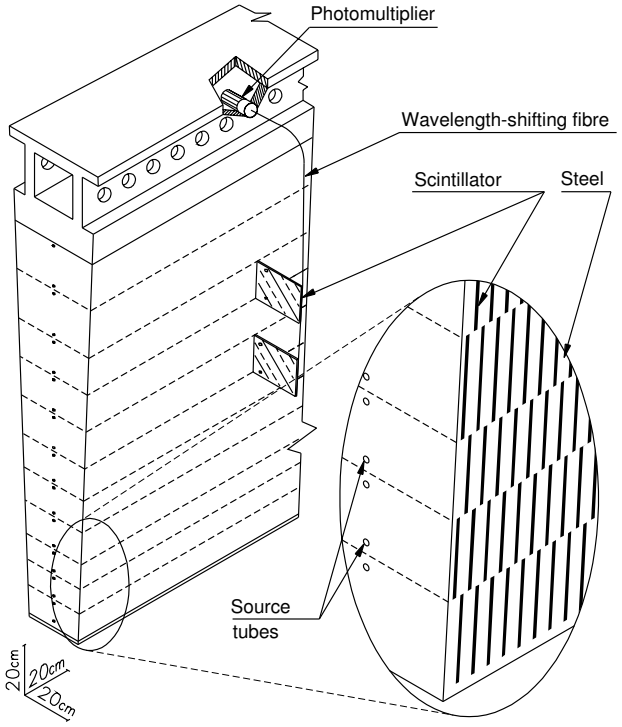

Figure 2.6: A sketch of a tile calorimeter module and its optical readout. Reproduced from Ref. [5].

The Hadronic Calorimeter is placed behind the EM calorimeter, and must absorb and measure the energy of the principally hadronic particles that penetrate the EM calorimeter. To achieve this, it is comprised of large amounts of heavy steel absorber, interspersed with layers of scintillating tiles to sample the charged particles created in the induced hadronic showers. These scintillators are read out by wavelength-shifting optical fibers coupled to photomultiplier tubes. Like the EM calorimeter, it covers the region $|\eta| < 3.2$. The layered scintillating tiles of each module are logically grouped into three layers; the sampling tiles of each layer are further grouped into readout cells that are approximately projective in both ϕ and η. The cell granularity is approximately $\Delta\eta \times \Delta\phi = 0.1 \times 0.1$ in the first two layers,

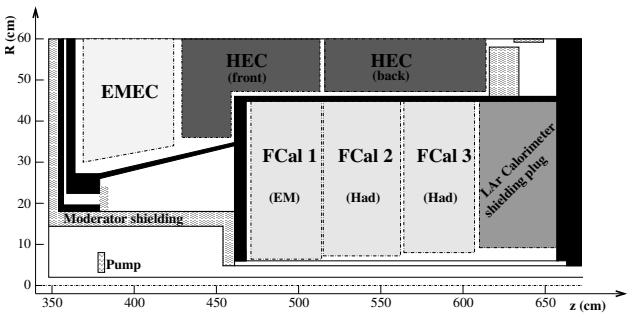

Figure 2.7: Schematic showing the location of the three FCal modules. Reproduced from Ref. [5].

and $\Delta\eta \times \Delta\phi = 0.2 \times 0.1$ in the outermost layer.

Forward Calorimeter

The Forward Calorimeter (FCal) is located in the center of the EM and Hadronic end-cap calorimeters, closer to the beam pipe (Figure 2.7). It covers the region $3.1 < |\eta| < 4.9$. This calorimeter provides both electromagnetic and hadronic measurements and stopping power, integrated into a single cryostat per end-cap. Each is divided into three modules layered in the z-direction. The first module is for electromagnetic calorimetry, with copper absorbers. The second two modules have tungsten absorbers and provide hadronic measurements. Liquid Argon is the active medium in all three modules.

2.2.4 Muon Spectrometer

The Muon Spectrometer (MS) is the outermost component of the ATLAS detector; its layout is illustrated in Figure 2.8. Its purpose is to measure the momentum of charged particles escaping the calorimeters. This is accomplished by making precision tracking measurements of the trajectories of these particles as they are bent by the toroidal magnetic field. The spectrometer provides coverage in the range $|\eta| < 2.7$, with the ability to trigger on particles in the $|\eta| < 2.4$ region. These measurements can be combined with tracking information from

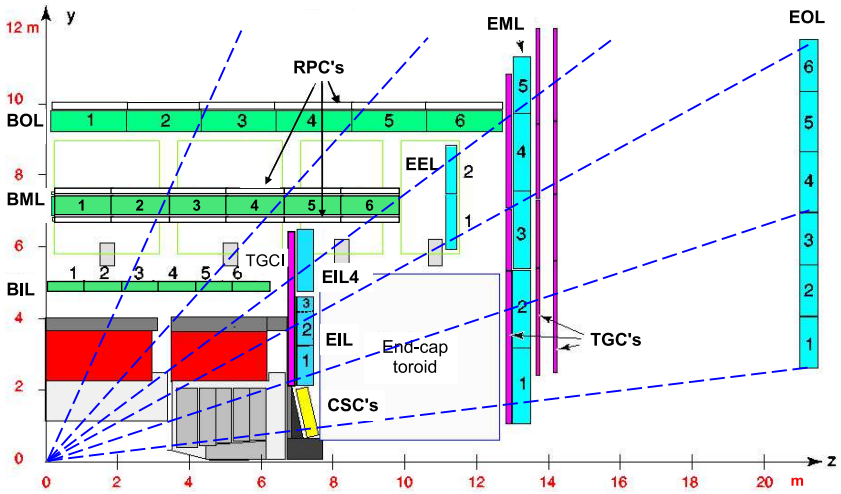

Figure 2.8: Schematic of MS components in the R-z plane demonstrating coverage in η. The green and blue components are MDTs. Reproduced from Ref. [5].

the ID, for improved momentum measurements and particle identification. As a standalone detector it is designed to be able to detect muons with momenta as low as several GeV (below which losses in the calorimeter cannot be neglected), and up to about 3 TeV.

Precision tracking is provided in the barrel and end-cap regions by Monitored Drift Tubes (MDTs), supplemented by Cathode Strip Chambers (CSCs) in the forward region of the end-cap where higher rates are expected. The MDTs are drift tube detectors, with an average resolution of 80 μm per tube at nominal background levels. These chambers have a very rigid and stable mechanical structure, essential for achieving the stringent alignment tolerances of less than 30 μm. The CSCs are multi-wire drift chambers with radially-oriented wires strung between two cathode planes. The cathode planes are segmented into strips; the strips of one plane are oriented perpendicular to the anode wires to give precision measurements in the bending direction, while the strips of the other plane are slightly coarser. The resolution is 60 μm in the bending direction, and 5 mm in the transverse direction.

The trigger system is comprised of Resistive Plate Chambers (RPCs) and Thin Gap Chambers (TGCs) in the barrel and end-cap regions, respectively. These chambers operate much

faster than the drift chambers of the precision tracker, and are capable of delivering track information with latency of only a few tens of nanoseconds. They are widely interspersed in between layers of the rest of the muon spectrometer in order to provide a long lever arm for rapid *in situ* momentum discrimination.

2.2.5 Trigger and Data Acquisition

During LHC Run-1, the ATLAS trigger and data acquisition (TDAQ) system operated as a three-tiered system consisting of the Level-1 (L1) trigger, Level-2 (L2) trigger, and the event-filter (EF) [14]. The L1 trigger is a collection of very fast trigger systems, mostly implemented in specialized hardware, which monitor the calorimeters and muon system for very basic signatures. It must make triggering decisions for collisions occurring at rates of up to 40 MHz, accepting events at no more than 75 kHz (upgradeable to 100 kHz), with a latency of less than 2.5 μs [15]. These requirements are imposed to accommodate design parameters of the readout electronics of the various detector subsystems. The L2 trigger and EF both run in software on computing farms located outside of the main detector cavern. The primary difference between them is the amount of data and processing time used to make triggering decisions. L2 trigger decisions are based only on subsets of the event data defined by Regions-of-Interest (ROIs) identified on-the-fly by a dedicated ROI-builder [16]. After events are accepted by L2, all data for the entire event is read out and further filtering based on the fully-reconstructed event is handled by the EF. Events rejected by the L2 trigger are cleared immediately from the readout buffers.

As part of the Run-2 upgrades carried out during LS1, the L2 and EF stages were combined into a unified, modular trigger system running on a single processing farm. This new design, called the High Level Trigger (HLT) is more efficient and easier to maintain. Instead of forwarding events to a logically and physically separate L2 and EF stage, data is requested

from readout buffers progressively as the HLT decision is processed. Events which pass all stages of the trigger are saved in a RAW format, containing very low-level information from each subdetector with an average size of approximately 1.5 MB per event. The total rate of accepted events from EF/HLT is limited to a maximum of approximately 1 kHz in Run-2 (previously ∼200–400 Hz in Run-1) [17]; this limit is imposed by the long-term data storage capacity at the CERN Tier-0 datacenter, and to a lesser extent, the computing resources.

2.3 Physics Object Reconstruction

2.3.1 Electrons and Photons

Electrons and photons have similar signatures in the ATLAS electromagnetic calorimeter. Fundamentally this is because photons with energy above approximately 10 MeV principally lose their energy in matter via e^+e^- pair creation, while electrons above this energy lose energy via *bremsstrahlung* emission of photons. The key discriminating features between electrons and photons are the shape of the EM cascade within the LAr calorimeter and the existence of tracks in the ID which lead to the activated region of the calorimeter.

Clusters of cells of the EM calorimeter are are seeded by 3×5 cell preclusters from the middle layer of the LAr calorimeter with total energy exceeding 2.5 GeV [18]. Tracks from the ID are then extrapolated to this middle layer and compared to the positions of the seed preclusters. Tracks are considered to match a cluster if they are within 0.05 in η and 0.1 in ϕ of each other; the looser ϕ requirement is to accommodate the bending effect of the solenoid field. Clusters which have at least one matched track are defined as an *electron candidate*; those without a matched track are defined as an *unconverted photon candidate*. Track-matched electron candidates are further distinguished into prompt electron and *converted photon* candidates by checking for pairs of tracks originating from a displaced vertex which lies at the start of

the trajectory of the track-cluster system [19].

Seeds are then reclustered [20] with different algorithms optimized for unconverted photons, converted photons, and prompt electrons. The total energy of the particle candidate is estimated by correcting the measured energy of the cluster cells for effects such as energy leakage outside of the calorimeter cells, energy loss in the ID, and fractional energy estimated by the presampler [21]. For candidates with at least one track hit in either of the silicon detectors, the direction of the 3-vector momentum is taken from the parameters of the matched track. For candidates with only TRT hits, the ϕ coordinate is taken from the track and η is taken from the barycenter of the calorimeter cluster. In the case of unconverted photons, both η and ϕ coordinates are taken from the calorimeter cluster.

2.3.2 Muons

While ATLAS can reconstruct muons using information solely from the MS (known as stand-alone muons), it is possible to use combined information from the MS, ID, and calorimeters, for which there are multiple algorithms [22, 23]. Most ATLAS analyses, including those documented in Chapter 3, utilize a reconstruction algorithm referred to as *combined* or CB muons. For combined muons, tracks are reconstructed independently in both the ID and MS. The MS tracks are then extrapolated inward to the ID, and for each pair of extrapolated and ID tracks, the track parameters are compared and compatibility is ranked by χ^2 value. Starting with the best-matched pairs and continuing for all pairs above a certain χ^2 threshold, the ID and MS track hits of each pair are used together in a global fit to form a new track. During this re-fitting, MS hits may be added or removed in order to improve the overall fit quality.

2.3.3 Jets

Jets are not a fundamental physical object *per se*, but rather a conceptual entity that represents, at minimum, the collective four-momentum of a group of particle-like objects, typically distinguished from a larger collection of such objects. The collection of objects may for example be a listing of stable hadron momenta from a simulated QCD shower, a series of energy and direction measurements from a calorimeter, or track momenta from the inner detector. The purpose of this conceptual device is to provide an approximation of the kinematic properties of quarks and/or gluons, which cannot be observed as fundamental objects in isolation. Therefore, the properties of jets, and their relationship to the quarks and gluons they represent, is dependent on the particulars of how the jet is defined.

Older experiments used sliding-window or cone-based jet definitions, wherein objects contained in a fixed geometrical boundary are inclusively grouped together [24]. Such an algorithm is still used in the ATLAS L1 trigger. However, in modern experiments jets used in analysis are almost exclusively defined using sequential clustering algorithms, wherein individual constituents are iteratively selected and added to a jet based on various conditional requirements relating to properties such as p_{T} and relative angular separation. There are several [25–28] such clustering algorithms; at ATLAS the most commonly used and best-understood [29–31] algorithm is anti-k_t [27] with radius parameter $R = 0.4$.

The standard anti-k_t jets with parameter $R = 0.4$ used in most ATLAS analyses begin with calorimeter *topo-clusters* as inputs [32] to the jet algorithm. Topo-clusters are three-dimensional topological clusters of cells [20] from both the hadronic and electromagnetic calorimeters, defined by the following algorithm:

0. Clusters are first seeded by cells with a signal-to-noise ratio (SNR) greater than 4.

1. For each seed (starting with the highest SNR), all neighboring cells which are not

already identified as a seed or member of another cluster are added to the cluster.

2. If the neighboring cell has a SNR greater than 2, it is added to a neighbor seed list, and if it is adjacent to an existing cluster, the clusters are merged.

3. This process is repeated from step (1) until the seed list is empty.

4. The list of neighbor seeds is then defined as the new seed list and the procedure is repeated again from step (1) until no new neighbor seeds are found.

The calorimeter energies used in reconstructing topo-clusters are measured relative to the EM scale, which accurately measures the energy deposited by particles produced in electromagnetic showers [33]. The resulting jets formed from these topo-clusters are then calibrated [34] to the hadronic energy scale. This calibration also accounts for the effect of pileup by subtracting [35] a factor $\rho \times A$ from the p_{T}, where ρ is the average calorimetric energy density per unit area in the η-ϕ plane, and A is the active jet area [36]. The direction of the reconstructed jet is also corrected to point to the primary event vertex, rather than the geometric center of the ATLAS detector.

2.3.4 $E_{\mathrm{T}}^{\mathrm{miss}}$

The missing transverse energy, $E_{\mathrm{T}}^{\mathrm{miss}}$, is reconstructed by independently summing over the x and y components of momentum of each identified object in the event. Energy deposits in the calorimeter may count towards the reconstruction of multiple different types of physics objects. Therefore, overlapping objects are chosen in a specific order of precedence [37]: electrons, photons, hadronically decaying τ-leptons, jets, and lastly muons[1]. The terms for each of these objects are calculated using calorimeter cells that have been appropriately calibrated in energy for their respective object types. Calorimeter cells not associated to

[1]That is, the portion of energy lost to the calorimeter by muons identified in the MS and/or ID.

any object are also taken into account in the calorimeter $E_{\mathrm{T}}^{\mathrm{miss}}$ term, as are very low-p_{T} ID tracks not associated to any calorimeter cell or where the track momentum measurement is more accurate than the calorimeter measurement.

The contribution to the muon term depends on whether a given muon is isolated from reconstructed calorimeter jets (that is, separated by a distance $\Delta R > 0.3$) to prevent double-counting of energy. Isolated muons are added to the $E_{\mathrm{T}}^{\mathrm{miss}}$ using their calibrated p_{T} which is corrected for calorimeter energy loss, and the calorimeter cells associated to this muon are not added to the calorimeter $E_{\mathrm{T}}^{\mathrm{miss}}$ term. For non-isolated muons, the energy deposited by the muon in the calorimeter cannot be resolved from the energy deposited by the jet. Therefore the stand-alone MS momentum of the muon, measured *after* energy loss to the calorimeter, is used in the muon term, and the calorimeter cells associated to the muon are added to the calorimeter $E_{\mathrm{T}}^{\mathrm{miss}}$ term.

The x and y components of the missing energy vector, E_x^{miss} and E_y^{miss}, are defined as the negative sum of the object $E_{x(y)}$'s as described above:

$$E_{x(y)}^{\mathrm{miss}} = -\sum_{\mathrm{cells}} E_{x(y)}^{\mathrm{cell}} - \sum_{\mathrm{muons}} E_{x(y)}^{\mu}$$

Where for calorimeter cells, we define [38]

$$E_x^{\mathrm{cell}} := E_{\mathrm{cell}} \sin\theta_{\mathrm{cell}} \cos\phi_{\mathrm{cell}} \,,$$
$$E_y^{\mathrm{cell}} := E_{\mathrm{cell}} \sin\theta_{\mathrm{cell}} \sin\phi_{\mathrm{cell}} \,,$$

and for the non-calo muon contributions, $E_{x(y)}^{\mu} := p_{x(y)}^{\mu}$.

The magnitude $E_{\mathrm{T}}^{\mathrm{miss}}$ and azimuthal angle ϕ^{miss} are defined as

$$E_{\mathrm{T}}^{\mathrm{miss}} := \sqrt{(E_x^{\mathrm{miss}})^2 + (E_y^{\mathrm{miss}})^2} \,,$$
$$\phi^{\mathrm{miss}} := \arctan(E_y^{\mathrm{miss}} / E_x^{\mathrm{miss}}) \,.$$

Chapter 3

Searches for Dark Matter with the ATLAS Detector

Prior to 2014, the primary method of searching for dark matter (DM) production at hadron colliders has been in the *mono-jet* and *mono-photon* channels, wherein a single isolated, high-energy jet or photon is recoiling against a large $E_{\mathrm{T}}^{\mathrm{miss}}$ [39–44]. This technique was proposed as a model independent means of probing dark matter interaction cross sections as early as 2004 [45]. Experimental searches in this channel (albeit for related, non-DM signals) were conducted [46, 47] by the DØ[48] and CDF [49] experiments at the Tevatron collider as early as 2003.

In the case where the visible object is simply produced as initial state radiation (ISR), this mono-jet channel is the most sensitive channel, with the mono-photon channel being the next-most sensitive [50, 51]. The radiation of massive vector bosons, by comparison, is much less likely, given their comparatively weak couplings and the effective reduction of phase space due to their mass.

Therefore, prior to this work, measurements of dark matter production in association with

a massive vector boson had not been undertaken. However, these ISR scenarios require the dark matter to be produced by some direct interaction between quarks and/or gluons. If, instead, the dark matter preferentially interacts with other particles, such as the W or Z bosons, channels with these particles in the final state could become relevant discovery modes. In implementing such a search, there are several possibilities to consider: we could consider either the associated production of W or Z particles, as well as leptonic or hadronic decays modes.

The works outlined in this chapter document an effort to expand the coverage of LHC dark matter searches by leveraging such phenomenological models and previously unexamined channels. For our initial work in expanding the mono-X search program, we chose to consider the $Z(\ell\ell) + E_{\mathrm{T}}^{\mathrm{miss}}$ channel (where $\ell = e$ or μ), discussed in Section 3.1. Then, we turn our attention to a brand new collider probe for dark matter, mono-Higgs. After the discovery of the Higgs boson at a mass of 125 GeV in 2012 [7], it became feasible to use this new particle as a visible probe for DM production. The first ever search in this new mono-Higgs channel is discussed in Section 3.2.

3.1 Search for Dark Matter Production in Association with a Z Boson

In Ref. [52], we propose a search for Dark Matter in the channel $Z(\ell\ell) + E_{\mathrm{T}}^{\mathrm{miss}}$ and reinterpret existing ATLAS measurements of the standard model $pp \to ZZ(\ell\ell\nu\nu)$ cross section [53] as limits on the upper bound of dark matter production under various phenomenological hypotheses. This reinterpretation demonstrated that this channel has comparable (albeit weaker) sensitivity to DM production models involving ISR as compared to existing mono-jet and mono-photon searches. In addition, we develop a novel EFT model (discussed in

Section 3.1.1) in which fermionic dark matter particles can be preferentially pair-produced in associate with a Z in the final state.

Given the encouraging results of Ref. [52], we proceed to implement a dedicated search using 20.3 fb^{-1} of ATLAS pp collision data at $\sqrt{s} = 8$ TeV. By conducting a measurement dedicated to the search for DM, we were able to optimize the selection parameters in order to maximize sensitivity to a collection of specific signal models. The details of this experimental measurement, the results of which are published in Ref. [54], are the subject of this section.

We choose to examine the $Z \to \ell^+\ell^-$ decay mode, where $\ell = e, \mu$, although a search in the combined $W/Z(\to q\bar{q}) + E_{\mathrm{T}}^{\mathrm{miss}}$ final state was also carried out by ATLAS simultaneously and reported in Ref. [55]. Both channels provide limits with similar sensitivity, despite the considerably larger branching fraction to quarks and the inclusion of the additional diagrams involving the W boson for the hadronic search. This is largely because the leptonic channel is extremely clean, given the excellent performance of the ATLAS detector in reconstructing electrons and muons with moderate energies and low backgrounds. Moreover, by choosing to search for events with $Z(\ell\ell)$, we can leverage the high mass resolution of this channel to very accurately tag events in the signal region to further reduce dilepton backgrounds.

3.1.1 Signal Models

We consider three basic types of dark matter signal models in this search: quark contact operators, vector boson contact operators, and a scalar mediator.

Quark Contact Operators

The first type is an EFT representing a basic $qq\chi\chi$ contact operator; the Z boson in these events is produced as ISR. See Figure 3.1. These signals are included as a common benchmark

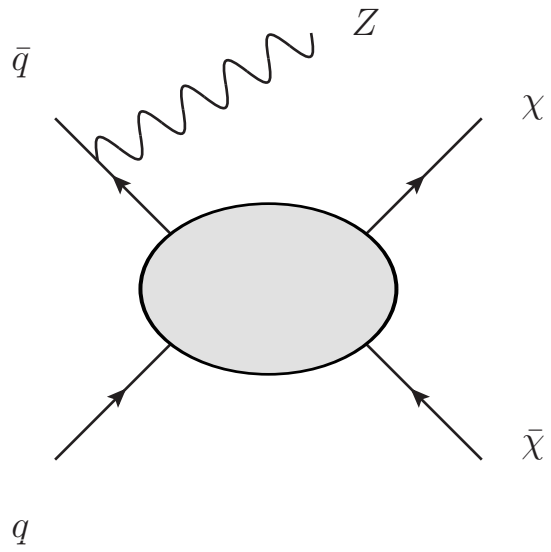

Figure 3.1: Diagram showing dark matter production via an effective quark contact interaction with Z boson ISR.

for comparison with existing and future searches in the more conventional mono-jet and mono-photon ISR channels.

These models were surveyed extensively in [56], and generally have a single free parameter which is proportional to the overall interaction term of the Lagrangian (and hence, the matrix element and cross section). The proportionality relationships for the operators considered in this study are given in Table 3.1.

For the experimental measurement we consider only the D1, D5, and D9 operators. The reason for this choice is that the kinematic distributions of events from any given operator can generally be classified into one of three groups represented by these three operators, as shown in Figure 3.2. For example, the pseudoscalar operator D2 has momentum and $E_{\mathrm{T}}^{\mathrm{miss}}$ distributions that are effectively identical to the related D1 scalar operator. Hence, the different operators within each grouping can not be discriminated solely based on the $E_{\mathrm{T}}^{\mathrm{miss}}$ observed at the collider.

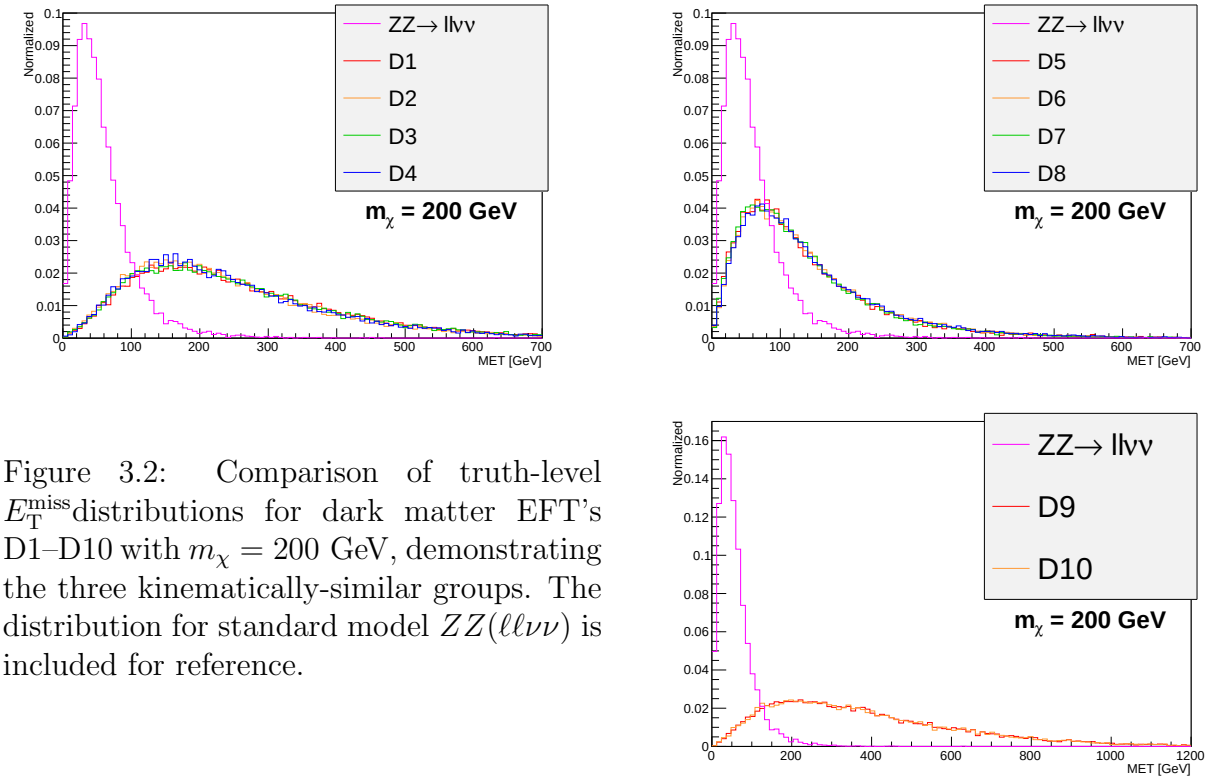

Figure 3.2: Comparison of truth-level $E_{\mathrm{T}}^{\mathrm{miss}}$distributions for dark matter EFT's D1–D10 with $m_\chi = 200$ GeV, demonstrating the three kinematically-similar groups. The distribution for standard model $ZZ(\ell\ell\nu\nu)$ is included for reference.

Name	Operator	Coefficient
D1	$\bar{\chi}\chi\bar{q}q$	$m_q/\Lambda_\star^3$
D5	$\bar{\chi}\gamma^\mu\chi\bar{q}\gamma_\mu q$	$1/\Lambda_\star^2$
D9	$\bar{\chi}\sigma^{\mu\nu}\chi\bar{q}\sigma_{\mu\nu}q$	$1/\Lambda_\star^2$

Table 3.1: The naming scheme of quark contact operators examined in this study. For each operator, the interaction term of the Lagrangian is shown, as well as the overall coefficient for the term. The EFT suppression scale, $\Lambda_\star$, has units of mass and in general the signal cross section will be proportional to the square of this coefficient.

Vector Boson Contact Operators

The second type is also an EFT which describes an interaction between dark matter and the vector bosons, developed in [52]. As shown in Figure 3.3, this process proceeds via the exchange of a virtual Z/γ^*. This intermediate state then decays to an on-shell boson and dark matter pair via a higher-dimensional effective operator.

Two cases of these operators, collectively referred to throughout as $ZZ\chi\chi$ operators, are

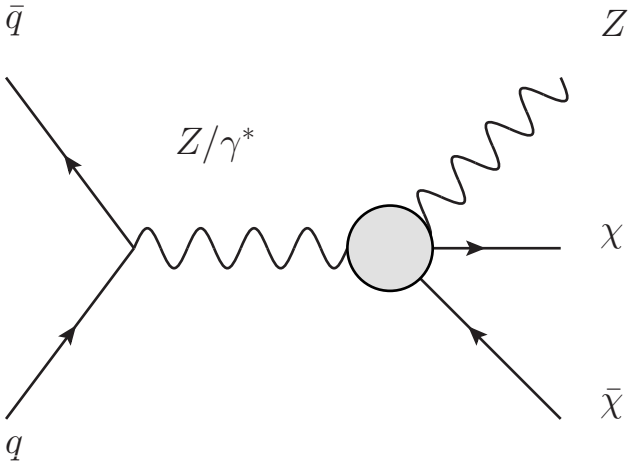

Figure 3.3: Diagram showing dark matter production via an effective interaction with vector bosons. Note that this topology requires a vector boson in the final state.

considered: dimension-5 and dimension-7. In the dimension-5 case, the dark matter couples to both Z and W, the latter of which does not contribute to our signal. These interactions arise from the inclusion of the Lagrangian term:

$$\mathcal{L}^{\text{dim.5}} \supset \frac{1}{\Lambda_5^3}\bar{\chi}\chi(D_\mu H)^\dagger D^\mu H \tag{3.1}$$

Which, upon expanding the covariant derivative D^μ and allowing to Higgs to assume its vacuum expectation value, gives rise to the term:

$$\mathcal{L}^{\text{dim.5}} \supset \frac{m_W^2}{\Lambda_5^3}\bar{\chi}\chi W^{+\mu}W_\mu^- + \frac{m_Z^2}{2\Lambda_5^3}\bar{\chi}\chi Z^\mu Z_\mu \tag{3.2}$$

In the dimension-7 case, the dark matter field χ couples to the gauge kinetic terms:

$$\mathcal{L}^{\text{dim.7}} \supset \frac{1}{\Lambda_7^3}\bar{\chi}\chi \sum_i k_i F_i^{\mu\nu} F^i_{\mu\nu} \tag{3.3}$$

where F_i for $i = 1, 2, 3$ are the field strength tensors for the standard model $U(1)$, $SU(2)$, and $SU(3)$ gauge groups and k_i are free parameters of the theory; we will consider only $k_3 = 0$,

ignoring the case of coupling to gluons. Upon expansion, this gives rise to not only pairs of gauge bosons but also to $Z\gamma$; the couplings to SM gauge bosons are given by:

$$g_{WW} = \frac{2k_2}{s_w^2 \Lambda_7^3} \tag{3.4}$$

$$g_{ZZ} = \frac{1}{4s_w^2 \Lambda_7^3} \left(\frac{k_1 s_w^2}{c_w^2} + \frac{k_2 c_w^2}{s_w^2} \right) \tag{3.5}$$

$$g_{\gamma\gamma} = \frac{1}{4c_w^2} \frac{k_1 + k_2}{\Lambda_7^3} \tag{3.6}$$

$$g_{Z\gamma} = \frac{1}{2s_w c_w \Lambda_7^3} \left(\frac{k_2}{s_w^2} - \frac{k_1}{c_w^2} \right) \tag{3.7}$$

where s_w and c_w are the sine and cosine of the weak mixing angle, respectively. We note that for $k_2 > 0$, the overall scale of these couplings are proportional to k_2/Λ_7^3, but because of the interference of the parameters in Equation (3.7), it is possible to independently adjust the magnitude of $g_{Z\gamma}$. In this analysis, we consider two cases:

1. $k_1/k_2 = c_w^2/s_w^2$, for which there is no Z/γ^* coupling. This is referred to throughout as $ZZ\chi\chi$-min.

2. $k_1 = 0$, for which the Z/γ^* contribution is maximal for a given value of k_2. This is referred to as $ZZ\chi\chi$-max.

Scalar Mediator

The third type of signal considered is a simplified model, comprised of an additional scalar field which carries quark number and a Majorana fermion dark matter particle as proposed in [57]. In this model, dark matter may be produced directly by quark annihilation with any type of ISR, but since the scalar also couples to the Z boson, it may be produced via internal fusion of the scalar exchange as shown in Figure 3.4. The model is described by a

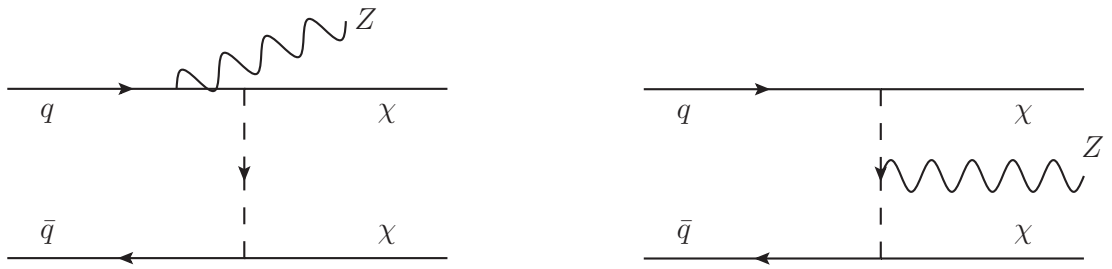

Figure 3.4: Diagram showing dark matter production via t-channel exchange of a scalar mediator. In this model, the Z boson may be produced either as ISR or as a fusion product of the virtual scalar state.

Lagrangian term:

$$\begin{aligned} \mathcal{L} &\supset f_{ud}\bar{Q}_{\mathrm{L}}\eta\chi_{\mathrm{R}} + h.c. \\ &= f_{ud}(\eta_u\bar{u}_{\mathrm{L}} + \eta_d\bar{d}_{\mathrm{L}})\chi_{\mathrm{R}} + h.c. \end{aligned} \tag{3.8}$$

where here the DM field χ is a Majorana fermion, f_{ud} is a coupling strength to up/down quarks, and the scalar field η carries the quantum numbers of the left-handed quark. In this study we also extend this interaction term to include couplings to charm and strange quarks, with a common coupling $f = f_{ud} = f_{cs}$.

3.1.2 Monte Carlo Samples

In order to assess the expected signal sensitivity for a given selection of data, it is necessary to estimate the fiducial contribution of signal and background. To this end, use Monte Carlo simulations for the theoretical signal as well as any backgrounds that are to be estimated by theory.

All $pp \to Z\chi\chi$ signal events are generated at parton-level using MadGraph 5 1.5.2 [58]. The WZ and ZZ background events are generated with POWHEG BOX 1.0 [59]. Parton showering and hadronization is then applied using PYTHIA 8.1 [60] with the AU2 tune [61]. Additional ZZ samples are produced with SHERPA 1.4.1 [62] for the purpose of evaluat-

ing theoretical systematic differences. Finally, these generated events are passed through the ATLAS GEANT4 simulation [63, 64] to emulate the detector response to each event. The simulated detector response for each event is superimposed with a random sample of minimum bias events before digitization, to model the effect of expected pileup conditions (additional inelastic proton collisions occurring in the same or adjacent bunch crossings) in the dataset. As it is impossible to know the exact pileup profile before the completion of data-taking (when the MC simulations are produced), the simulated events are re-weighted *post hoc* to match the distribution observed in data.

For the EFT models we must specify the mass of the DM candidate; for DM masses below $\sim$ 100 GeV the cross sections are largest and mostly insensitive to the mass. As the DM mass approaches the TeV level, the cross sections diminish rapidly, as expected due to the limited probability of initial states with the required momentum fraction. In order to sample the variation in cross section and kinematics, each model is generated with masses $m_\chi = 1, 10, 200, 400, 1000$ GeV.

For the scalar-mediator model, in addition to specifying the mass m_χ, it is also necessary to independently specify the mediator mass m_η. Values are chosen on a grid to probe both mediator and DM masses up to the TeV scale, above which LHC cross sections become negligible. The schedule of masses generated for this search are:

$m_\chi = 10$ GeV, $\quad m_\eta = 200, 500, 700, 1000$ GeV

$m_\chi = 200$ GeV, $\quad m_\eta = 500, 700, 1000$ GeV

$m_\chi = 400$ GeV, $\quad m_\eta = 500, 700, 1000$ GeV

$m_\chi = 1000$ GeV, $\quad m_\eta = 1200$ GeV

3.1.3 Physics Objects and Event Selection

This analysis is split into two separate sub-channels: dielectron (ee) and dimuon ($\mu\mu$), each of which have their own criteria for selecting events and the leptons which reconstruct the

Z candidate in each event. First, events are required to satisfy either a single- or di-lepton trigger. They must also contain at least one reconstructed vertex associated with at least three tracks of $p_{\mathrm{T}} > 400$ GeV, in order to suppress non-collision backgrounds.

Next, we reconstruct a Z candidate by requiring two same-flavor, opposite-sign leptons, with an invariant mass in the range 76 GeV $< m_{\ell\ell} <$ 106 GeV. To suppress events with spurious $E_{\mathrm{T}}^{\mathrm{miss}}$ arising from mis-measured jets, we require that the azimuthal angle between the dilepton system momentum and the $E_{\mathrm{T}}^{\mathrm{miss}}$, $\Delta\phi(E_{\mathrm{T}}^{\mathrm{miss}}, p_{\mathrm{T}}^{\ell\ell}) > 2.5$. Similarly, since we expect the momentum of the real $E_{\mathrm{T}}^{\mathrm{miss}}$ from our signal process to balance the recoiling Z, we require $|p_{\mathrm{T}}^{\ell\ell} - E_{\mathrm{T}}^{\mathrm{miss}}|/p_{\mathrm{T}}^{\ell\ell} < 0.5$. This recoil effect, combined with the generally high p_{T} distributions of the signal process, tends to create more central Z's relative to the backgrounds, so we also require $|\eta^{\ell\ell}| < 2.5$.

To suppress top-quark backgrounds, we veto any event containing a selected jet with $p_{\mathrm{T}} >$ 25 GeV. Similarly, to reduce the diboson background, events containing a third lepton of any flavor or sign with $p_{\mathrm{T}} > 7$ GeV are removed.

Finally, events satisfying all these criteria are categorized into four overlapping signal regions depending on the magnitude of $E_{\mathrm{T}}^{\mathrm{miss}}$ in the event. This is because the different signal models have considerably different $E_{\mathrm{T}}^{\mathrm{miss}}$ spectra, in some cases depending on the hypothetical mass of the dark matter particle. Each signal sample is assigned to the $E_{\mathrm{T}}^{\mathrm{miss}}$ signal region which maximizes its expected sensitivity. The $E_{\mathrm{T}}^{\mathrm{miss}}$ thresholds for the four regions are 150, 250, 350, and 450 GeV.

The definitions of the various physics objects used in the evaluation of these event selection criteria are detailed in the subsections below.

Trigger

The lowest-threshold unprescaled single- and di-lepton triggers are used in this analysis, of which there are three in each channel. In the ee channel, the two single-lepton triggers have p_{T} thresholds of 24 and 60 GeV, with the former satisfying more stringent requirements on hadronic and track isolation. The di-lepton trigger has a p_{T} threshold of 12 GeV, with hadronic isolation requirements on both objects and a slightly looser EM identification criteria than the single-lepton triggers.

In the $\mu\mu$ channel, the single-lepton p_{T} thresholds are 24 GeV (track-isolated) and 36 GeV. The di-lepton threshold is 13 GeV, with a looser identification requirement.

Electrons

Reconstructed electrons are required to have a momentum in the range $p_{\mathrm{T}} > 20$ GeV and $|\eta| < 2.47$. They must pass identification criteria [21] on hadronic calorimeter leakage, EM calorimeter shower shape, and number of inner detector hits, that are designed to reject jets and photons. They are also required to pass certain quality requirements which depend on the conditions of the calorimeter, such as whether the calorimeter cluster in question contains cells which are known to have high noise.

Electrons are required to be isolated from other tracks in the ID. The total momentum of all tracks with $p_{\mathrm{T}} > 1$ GeV within $\Delta R < 0.2$ of the electron track is computed, and must satisfy $p_{\mathrm{T}}^{\sum \mathrm{tracks}}/p_{\mathrm{T}}^{e} < 0.1$.

For the purposes of the third-lepton veto, electrons with $p_{\mathrm{T}} > 7$ GeV are retained, but are not considered for the dilepton system used to construct the Z candidate.

Muons

Muons are reconstructed using the *combined* method of matching and refitting ID and MS tracks together, where the MS-measured momentum accounts for energy loss in the calorimeter. Muons within the momentum range $p_{\mathrm{T}} > 20$ GeV and $|\eta| < 2.5$ are considered. Various quality requirements on the number and quality of inner detector hits are imposed [22].

Muons must also be isolated from other tracks in the ID; the requirement is identical to the one used in the electron isolation: $p_{\mathrm{T}}^{\sum \mathrm{tracks}}/p_{\mathrm{T}}^{\mu} < 0.1$.

To remove candidates caused by cosmic ray hits or which do not originate from the primary vertex, we require a transverse impact parameter $|d_0| < 1$ mm and longitudinal impact parameter $|z_0| < 10$ mm. The primary vertex is defined as the one for which the $\sum p_{\mathrm{T}}^2$ of all tracks associated with it is greatest.

For the purposes of the third-lepton veto, muons with $p_{\mathrm{T}} > 7$ GeV are retained, but are not considered for the dilepton system used to construct the Z candidate.

Jets

Jets are reconstructed from calorimeter topo-clusters using the anti-k_t algorithm with radius parameter $R = 0.4$, and required to have $p_{\mathrm{T}} > 25$ GeV and $|\eta| < 4.5$. Pileup jets originating from collisions other than the hard interaction of interest in the event are removed by requiring that most of the tracks in the jet are compatible with the primary vertex. This is quantified by the *jet vertex fraction* (JVF), defined as the scalar p_{T} sum of tracks that are associated with the jet and which originate from the primary vertex, divided by the scalar p_{T} sum of all tracks associated to the jet [65]. The JVF is required to be at least 0.5 for all jets with momentum in the range $p_{\mathrm{T}} < 50$ GeV, $|\eta| < 2.4$. As with electrons, there are various additional quality requirements on jets dependent on the instrument condi-

tions. However, certain jets fall into categories identified by ATLAS performance experts as particularly poorly-reconstructed. Because these jets can have adverse effects on the $E_{\mathrm{T}}^{\mathrm{miss}}$ reconstruction, any events containing such jets are removed.

Missing Transverse Momentum

As described in Section 2.3.4, the $E_{\mathrm{T}}^{\mathrm{miss}}$ is measured from energy deposited in the calorimeters and from reconstructed muons. The energy and momenta are calibrated as appropriate for the objects to which they are associated. The objects included in this calculation are muons, electrons, photons, and taus with $p_{\mathrm{T}} > 10$ GeV, and jets with $p_{\mathrm{T}} > 20$ GeV. Low-p_{T} tracks not associated to a calorimeter cluster, as well as topo-clusters not associated with a jet are included in the calculation as well.

Overlap Removal

Once all the above physics objects have been defined and selected, we apply an additional filtering to remove overlap between different types of objects. This is to prevent double counting of single objects that may be successfully reconstructed as multiple different types, as well as to prevent poor-quality measurements in cases where multiple physical objects do actually overlap in the detector. The overlap removal proceeds in the following sequence:

1. Electrons within $\Delta R < 0.2$ of a muon are rejected.
2. Jets within $\Delta R < 0.2$ of any remaining electron are rejected.
3. Electrons are again filtered to remove any within $\Delta R < 0.4$ of any the remaining jets.
4. Muons within $\Delta R < 0.4$ of a jet are removed.

3.1.4 Backgrounds

In this search, the primary background is standard model $ZZ \to \ell^+\ell^-\nu\bar{\nu}$ production, wherein one Z boson decays to leptons while the other decays neutrinos. This background is irreducible; that is, on an event-by-event basis, this background mimics exactly the signature of our signal events. However, all of the dark matter signals generally tend to create events with larger $E_{\mathrm{T}}^{\mathrm{miss}}$, as shown in Figure 3.5. Therefore the best mitigation against this background is to cut aggressively on $E_{\mathrm{T}}^{\mathrm{miss}}$. However, cutting on $E_{\mathrm{T}}^{\mathrm{miss}}$ does have a cost; there is a trade off between increasing the signal-to-background ratio and limiting the statistical power of the available data sample. The optimal choice is the one which maximizes the statistical significance of the final result.

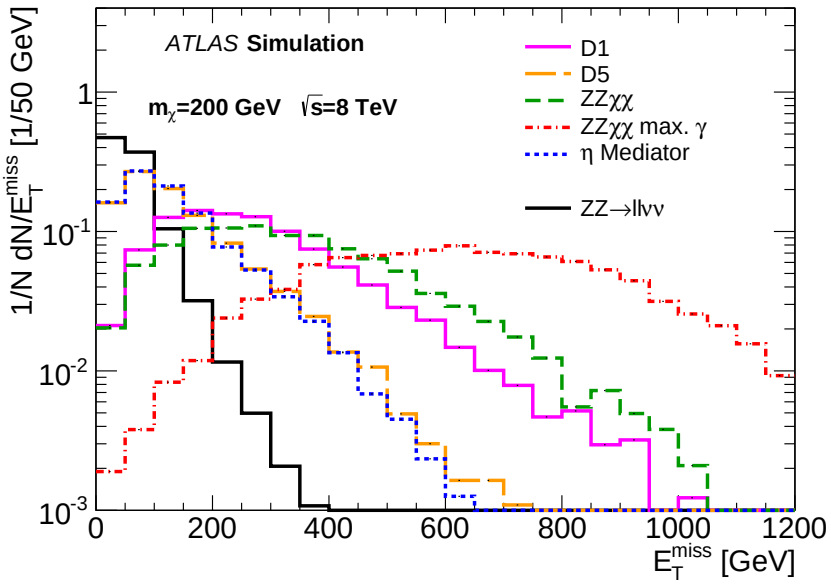

Figure 3.5: Comparison of $E_{\mathrm{T}}^{\mathrm{miss}}$ distributions for the primary ZZ background and the different signal models, after full simulation as described in Section 3.1.2. Each distribution is normalized to unity.

The second largest background is standard model WZ production, wherein the Z boson decays to leptons while the W boson either decays leptonically to a lepton plus neutrino, or to jets. If either the charged lepton or the jets from W decay are not correctly reconstructed

(for example, because it was very soft, or because of high detector occupancy), we observe an event with a reconstructed Z boson and $E_{\mathrm{T}}^{\mathrm{miss}}$ from the neutrino, mimicking our signal.

Other subdominant backgrounds include $WW(\ell\nu\ell\nu)$ production, where there are two real leptons and $E_{\mathrm{T}}^{\mathrm{miss}}$, and top quark production. The WW background is also irreducible, but is strongly mitigated by the requirement that the $\ell^+\ell^-$ system must have an invariant mass near m_Z. In the case of top quark pair-production, real leptons and $E_{\mathrm{T}}^{\mathrm{miss}}$ are produced in the decay of the top quarks. However, the top decays also produce jets which can be vetoed in the signal region.

Finally, there are fake backgrounds caused by $Z+\mathrm{jets}$ and $W+\mathrm{jets}$ production. In the case of $W+\mathrm{jets}$, fake events arise when a jet is reconstructed as an electron, which gets selected along with a real lepton from the W decay. Strictly speaking, for the purposes of our background estimate the single real lepton and single fake lepton could occur in semileptonic $t\bar{t}$, Wt, and WW events as well. However, for brevity and simplicity we refer to all of these collectively as $W+\mathrm{jets}$, as this process has a much higher cross section than the others.

In the case of $Z+\mathrm{jets}$, the leptons are both real and fall within the Z mass window; however, the limited resolution of the calorimeters results in an imperfect cancellation of momentum in observed particles. This creates a $E_{\mathrm{T}}^{\mathrm{miss}}$ signal that is not caused by the actual presence of invisible particles. These backgrounds are greatly suppressed by the $E_{\mathrm{T}}^{\mathrm{miss}}$ cuts already imposed by the primary ZZ background, as well as the jet veto discussed in Section 3.1.3. However, providing an estimate of their contribution in the signal region is tricky since these events are caused by imperfect detector effects which by definition we have no ability to model using *a priori* theoretical models. This background estimate is discussed in detail in Section 3.1.5.

The WZ and ZZ backgrounds are estimated from Monte Carlo simulation. For both processes, we use the POWHEG BOX [59], a next-to-leading-order generator. These MC pre-

dictions are validated in control regions where the expected signal is negligible. The ZZ prediction is validated by generating $ZZ \to \ell\ell\ell\ell$ events using the same MC tools and comparing to data in a four-lepton control region. Similarly, WZ prediction is validated by generating $WZ \to \ell\nu\ell\ell$ events and comparing to data in a three-lepton control region.

In order to estimate the contribution from WW, $t\bar{t}$, Wt, and $Z \to \tau\tau$ processes, a control region similar to the signal region, but consisting of an $e\mu + E_{\mathrm{T}}^{\mathrm{miss}}$ final state is defined. Because the leptons from these processes are real, we exploit the relative branching ratios of $1:1:2$ for the channels $ee:\mu\mu:e\mu$ to estimate that the number of events in this control channel is twice the number in either the ee or $\mu\mu$ signal channels.

The $W+$jets background is estimated by loosening the lepton identification requirement and reversing the isolation cut of the second electron in the event. The jet overlap removal is also omitted for this electron object. This provides a sample from data in which jets have been reconstructed as (low-quality) electrons. The $E_{\mathrm{T}}^{\mathrm{miss}}$ distribution of this control region is then fitted with an exponential shape, which is then re-normalized to match data subjected normal electron requirements in the low-$E_{\mathrm{T}}^{\mathrm{miss}}$ control region. Finally, the resulting function is integrated over the $E_{\mathrm{T}}^{\mathrm{miss}}$ range corresponding to the signal region in order to produce an estimate.

A summary of the predicted backgrounds and observed number of events is listed in Table 3.2.

3.1.5 $Z+$jets Background Estimation Method

The expected signal region contribution from $Z+$jets events is quite small, given the fairly low amount of fake $E_{\mathrm{T}}^{\mathrm{miss}}$ typically produced in these events, as well as the suppression by the jet veto. Nonetheless, it is a difficult background to model, since the jets in these events are generated from matrix elements calculated at leading-order in QCD using the ALPGEN [66]

Process	$E_{\mathrm{T}}^{\mathrm{miss}}$ threshold [GeV]			
	150	250	350	450
ZZ	41 ± 15	6.4 ± 2.4	1.3 ± 0.5	0.3 ± 0.1
WZ	8.0 ± 3.1	0.8 ± 0.4	0.2 ± 0.1	0.1 ± 0.1
$WW, t\bar{t}, Z(\tau\tau)$	1.9 ± 1.4	$0^{+0.7}_{-0.0}$	$0^{+0.7}_{-0.0}$	$0^{+0.7}_{-0.0}$
W + jets	0.5 ± 0.3	—	—	—
Z + jets	0.1 ± 0.1	—	—	—
Total Predicted	52 ± 18	7.2 ± 2.8	1.4 ± 0.9	$0.4^{+0.7}_{-0.4}$
Observed	45	3	0	0

Table 3.2: Expected SM backgrounds in each signal region, along with the number of events observed in the data sample. Fields containing "—" were deemed negligible. The stated uncertainties are the quadrature sum of statistical, systematic, and luminosity uncertainties.

generator. Moreover, since the fake $E_{\mathrm{T}}^{\mathrm{miss}}$ in these events is purely a detector effect, it is impossible to impose cuts on this variable until after events have been fully simulated, making it extremely inefficient to sample Monte Carlo near our signal region. Consequently, the ATLAS MC statistics available were insufficient to provide reliable estimate.

In order to produce this estimate, we develop a novel *ad hoc* parametric model, with parameters fitted to observed data. The key idea is to exploit the relative abundance of events in the low-$E_{\mathrm{T}}^{\mathrm{miss}}$ region (available in both data and MC) to model the behavior of some variable(s) vs. $E_{\mathrm{T}}^{\mathrm{miss}}$. Then, we may fit to these events in the control region and extrapolate into the high-$E_{\mathrm{T}}^{\mathrm{miss}}$ signal region. It is helpful if the dependence of these variable(s) demonstrates a simple dependence on $E_{\mathrm{T}}^{\mathrm{miss}}$.

To this end, we consider the $\Delta\phi_{Z,E_{\mathrm{T}}^{\mathrm{miss}}}$ distribution; that is, the difference in azimuthal angle between the momentum of the reconstructed Z boson and the direction of the $E_{\mathrm{T}}^{\mathrm{miss}}$. We choose to model the $\Delta\phi_{Z,E_{\mathrm{T}}^{\mathrm{miss}}}$ distribution as a Gaussian centered at π, with a constant offset:

$$f_{\Delta\phi}(x) = A + B \exp\left(-\frac{(x-\pi)^2}{2\sigma^2}\right) \tag{3.9}$$

This model reasonably reproduces the Z + jets distribution, as shown in Figure 3.6. The geometric interpretation of each of these parameters is also clear from this figure. We may

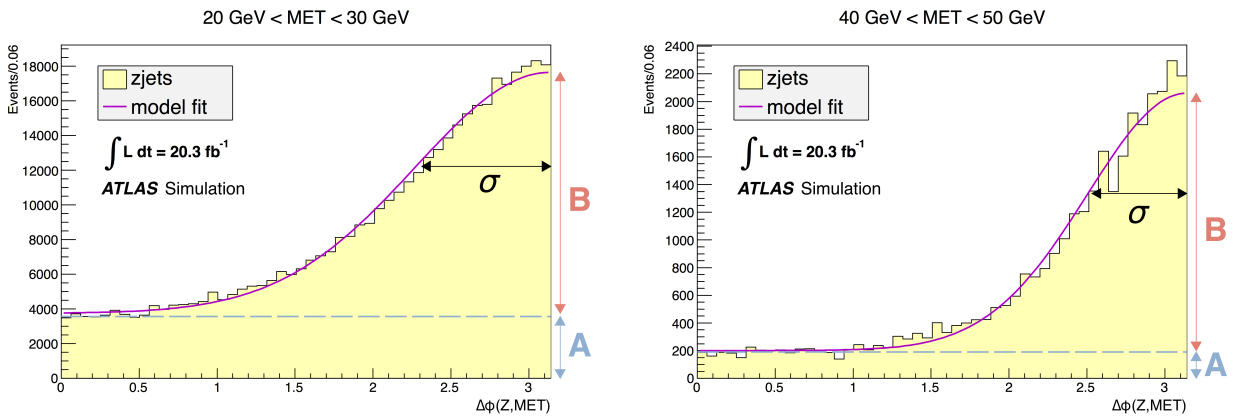

Figure 3.6: Demonstration of the Gaussian $\Delta\phi$ model fitted against $Z+$jets Monte Carlo, for two different slices in $E_{\mathrm{T}}^{\mathrm{miss}}$. The geometric interpretation of the parameters (A, B, σ) are sketched for illustration.

also motivate the model by considering a physical interpretation of these parameters. The parameter A represents the fraction of events with $E_{\mathrm{T}}^{\mathrm{miss}}$ from mis-measured jets, occurring in random directions relative to the Z boson. Parameter B represents the fraction of jets produced in opposition to the momentum of the Z boson. In the presence of momentum-balance cuts, increasing $E_{\mathrm{T}}^{\mathrm{miss}}$ is correlated to increasingly boosted Z's, which should be balanced by one or more jets on the opposite side of the detector. Hence the error in jet measurements contributing to the $E_{\mathrm{T}}^{\mathrm{miss}}$ should also be along this axis; therefore we expect the ratio A/B to decrease monotonically with $E_{\mathrm{T}}^{\mathrm{miss}}$.

In order to demonstrate the validity of the model throughout the control region, we validate the method on $Z+$jets MC. For a data-driven estimate, the parameters (A, B, σ) are to be determined by fitting in the low-$E_{\mathrm{T}}^{\mathrm{miss}}$ control region. Because the $Z+$jets process dominates over other backgrounds in this region (Figure 3.7), this gives us a highly pure sample of $Z+$jets events from data.

Figure 3.6 demonstrates that our model Equation (3.9) at least captures the shape of the $\Delta\phi_{Z,E_{\mathrm{T}}^{\mathrm{miss}}}$ distribution. However, two issues must be addressed in order to justify a fitting and extrapolation from data:

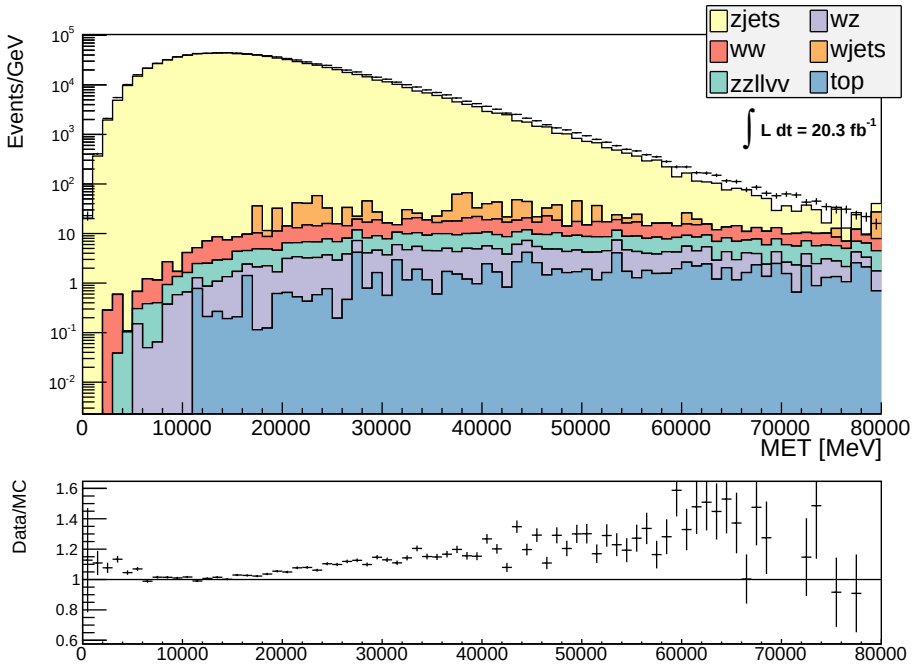

Figure 3.7: Comparison of different MC background processes against data in the low-$E_{\mathrm{T}}^{\mathrm{miss}}$ control region. The $Z+$jets backgrounds is overwhelmingly dominant at lower $E_{\mathrm{T}}^{\mathrm{miss}}$. Shown here is the electron ($Z \to ee$) channel.

1. Although the Gaussian model describes the distribution well at any $E_{\mathrm{T}}^{\mathrm{miss}}$, the shape is not fixed. We must understand how the parameters (A, B, σ) vary w.r.t $E_{\mathrm{T}}^{\mathrm{miss}}$.

2. Although Z+jets events dominate in the low-$E_{\mathrm{T}}^{\mathrm{miss}}$ region, there could be contamination from other processes that may affect the fit. We address this systematic effect by comparing the performance of the fitting method in pure $Z+$ jets MC against the combined background MC.

To address the first point, we will promote the constant parameters (A, B, σ) to continuous functions of $E_{\mathrm{T}}^{\mathrm{miss}}$. Figure 3.8 shows the best-fit (constant) parameters in different bins of $E_{\mathrm{T}}^{\mathrm{miss}}$, demonstrating the dependence of these parameters on $E_{\mathrm{T}}^{\mathrm{miss}}$. Inspecting these figures, we find that a simple and reasonable prescription is to model each parameter as a decaying

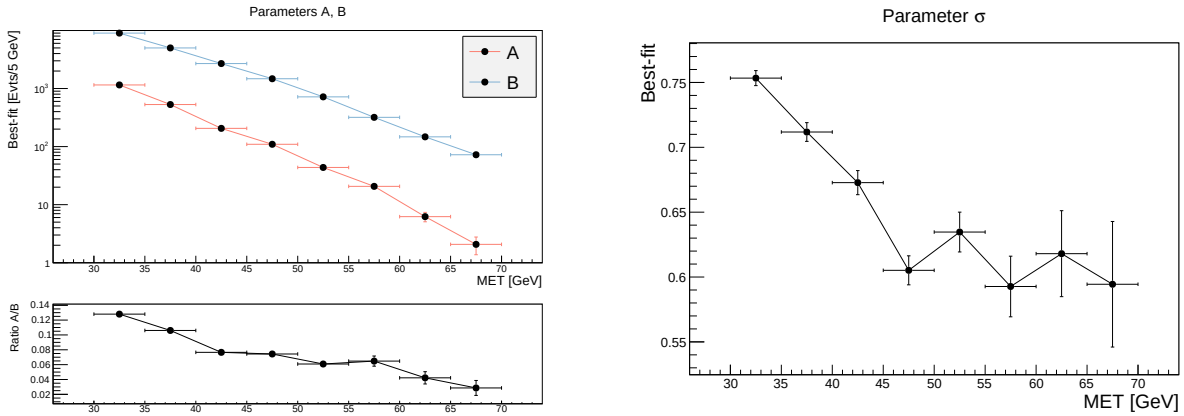

Figure 3.8: Best-fit shape parameters (A, B, σ) vs. $E_{\mathrm{T}}^{\mathrm{miss}}$, measured from $Z+$jets MC. We note that as $E_{\mathrm{T}}^{\mathrm{miss}}$ increases, the ratio A/B of randomly-oriented to collimated mis-measured energy decreases. The width σ of the peak appears to decay somewhat slowly from 0.75 to 0.6, although limited statistics in the higher $E_{\mathrm{T}}^{\mathrm{miss}}$ bins leads to large uncertainty and fluctuations.

exponential:

$$A \to A(x) = \exp[a_0 + a_1 x]$$

$$B \to B(x) = \exp[b_0 + b_1 x]$$

$$\sigma \to \sigma(x) = \exp[s_0 + s_1 x]$$

Then we are left with a six-parameter model for the two-dimensional distribution of $\Delta\phi_{Z,E_{\mathrm{T}}^{\mathrm{miss}}}$ vs. $E_{\mathrm{T}}^{\mathrm{miss}}$:

$$\begin{aligned} f_{[E_{\mathrm{T}}^{\mathrm{miss}},\Delta\phi]}(x,y) &= A(x) + B(x)\exp\left[-\frac{(y-\pi)^2}{2\sigma^2(x)}\right] \\ &= \exp[a_0 + a_1 x] + \exp\left[b_0 + b_1 x - \frac{(y-\pi)^2}{2\exp[s_0 + s_1 x]^2}\right] \end{aligned} \tag{3.10}$$

In order to obtain a numerical estimate from this model, we first fit for the six parameters in the low-$E_{\mathrm{T}}^{\mathrm{miss}}$ control region. Then we simply integrate the model over the phase space

representing the signal region:

$$N_{\text{S.R.}}^{Z+\text{jets}} = \int_{120\ \text{GeV}}^{\infty} \int_{2.5}^{\pi} dxdy f_{\left[E_{\text{T}}^{\text{miss}},\Delta\phi\right]}(x,y) \tag{3.11}$$

To address the second point and verify the model, we first test this new model's ability to fit pure $Z+$ jets MC. Then we check that the fit is robust against the small amount of contamination by non-$Z+$ jets backgrounds by fitting to the complete MC background model including all background processes. The results of these fits are shown in Figure 3.9. The reduced χ^2 of the fit in MC is high due to low statistical power of the sample and large number of bins required. Nonetheless, the predicted SR value in both cases is consistent with the $Z+$ jets MC. The $\sim$35% overestimation caused by inclusion of non-$Z+$ jets background contamination is assigned as a systematic error in the data-driven estimate.

The fit to data is shown in Figure 3.10. The reduced χ^2 of the fit is considerably better given the greatly enhanced statistical sample available in data. In Figure 3.11, the fitted model is integrated in various bins of $E_{\text{T}}^{\text{miss}}$ along the control region, and compared with MC and data. This comparison includes sub-regions of the low-$E_{\text{T}}^{\text{miss}}$ control region which were not used to fit the model, in order to validate against the data. It also illustrates that the model is able to accurately predict the $Z+$ jets background rates consistently along the $E_{\text{T}}^{\text{miss}}$ axis, and not just over large integrated regions. As expected, above approximately 80 GeVthe data diverges from the predicted $Z+$ jets background as the diboson backgrounds begin to dominate the event rates.

A summary of the final results for the $Z+$ jets model estimates derived by fits on MC and data are presented in Table 3.3. Note that the uncertainties become larger in the higher-$E_{\text{T}}^{\text{miss}}$ region, but the estimate itself becomes so small as to be negligible. Therefore, these large uncertainties have no impact on the overall sensitivity of the search.

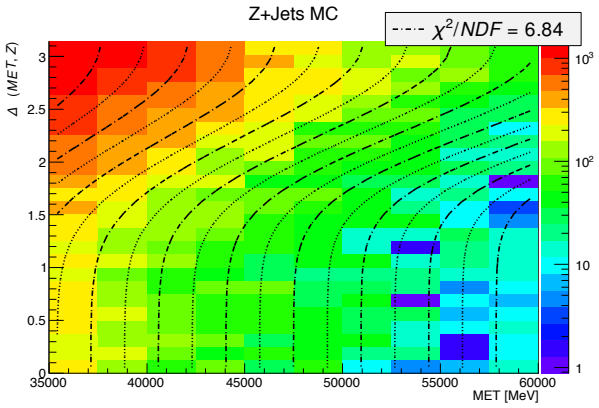

Model Extrapolation: 0.17 ± 0.02
MC Events in SR: 0.88 ± 0.94

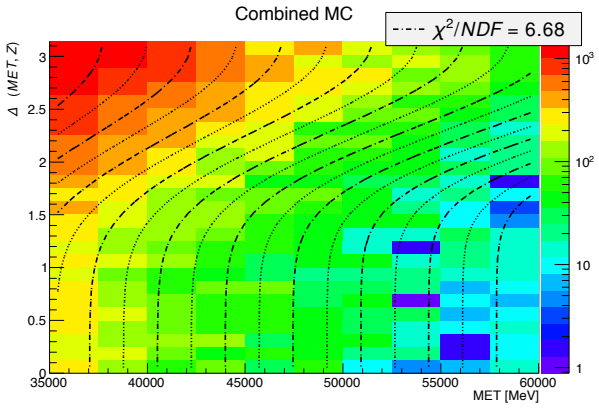

Model Extrapolation: 0.23 ± 0.03
MC Events in SR: 51.7 ± 7.19

Figure 3.9: The model of Equation (3.10) is fitted to MC distributions for Z + jets (left) and all backgrounds (right) in the $Z \to ee$ channel. In each case, the extrapolated model prediction of Z + jets events in the $E_{\mathrm{T}}^{\mathrm{miss}} > 120$ GeV region is also shown, along with the weighted number of MC events observed in the high-$E_{\mathrm{T}}^{\mathrm{miss}}$ region.

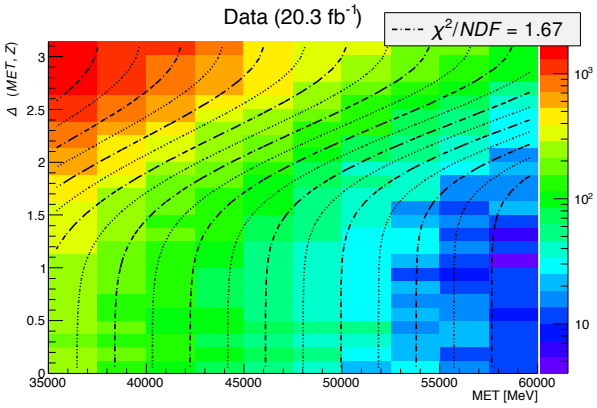

Model Extrapolation: 0.295 ± 0.025

Figure 3.10: The model of Equation (3.10) fitted to data in the low-$E_{\mathrm{T}}^{\mathrm{miss}}$ control region. The extrapolated model prediction of Z + jets events in the $E_{\mathrm{T}}^{\mathrm{miss}} > 120$ GeV region is indicated.

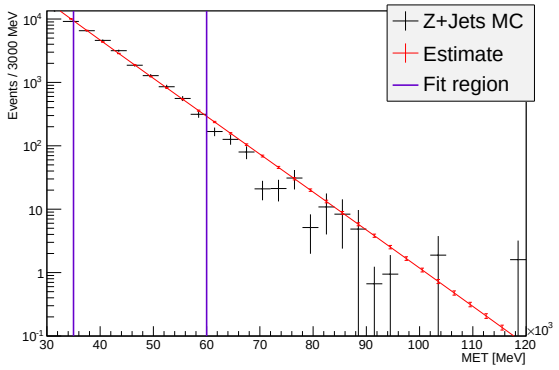

(a) MC Fit, ee channel

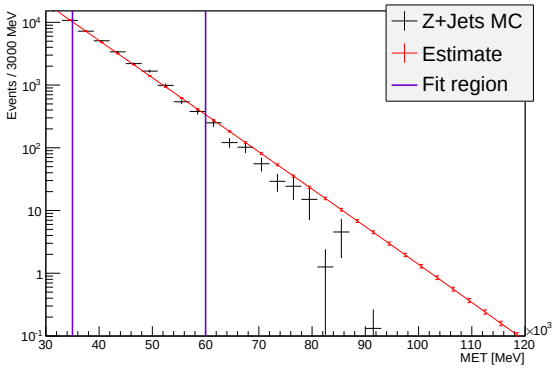

(b) MC Fit, $\mu\mu$ channel

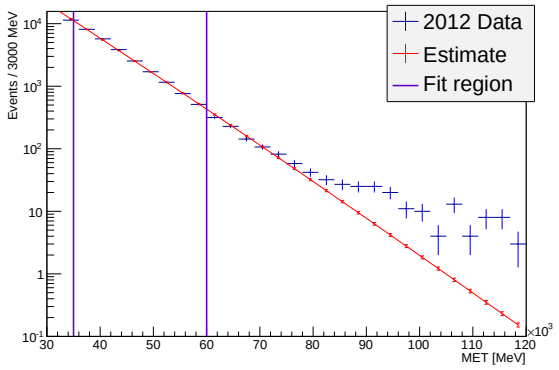

(c) Data Fit, ee channel

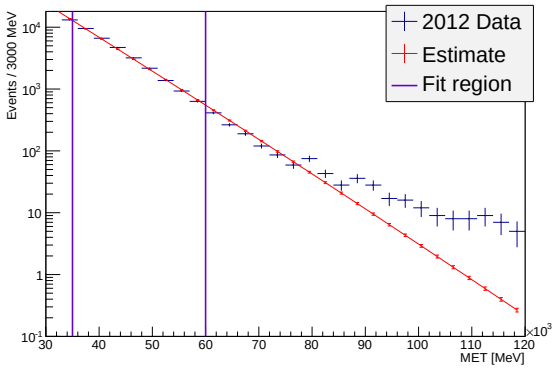

(d) Data Fit, $\mu\mu$ channel

Figure 3.11: Validation of the fitted $Z+$jets background model against pure $Z+$jets MC and data. The violet bars indicate the region used for fitting the model parameters. The region between 60 and 120 GeVis neither used for fitting, nor part of the signal region.

	$E_{\mathrm{T}}^{\mathrm{miss}} > 150$ GeV	
	ee	$\mu\mu$
$Z+$jets MC	$2.48 \times 10^{-3} \pm 15\%$ stat.	$2.80 \times 10^{-3} \pm 14\%$ stat.
Combined MC	$3.66 \times 10^{-3} \pm 15\%$ stat.	$4.81 \times 10^{-4} \pm 13\%$ stat.
Data	$\mathbf{4.57 \times 10^{-3}} \pm 11\%$ (stat.) $\pm 47\%$ (syst.)	$\mathbf{9.76 \times 10^{-3}} \pm 11\%$ (stat.) $\pm 31\%$ (syst.)

	$E_{\mathrm{T}}^{\mathrm{miss}} > 250$ GeV	
	ee	$\mu\mu$
$Z+$jets MC	$1.79 \times 10^{-9} \pm 28\%$ stat.	$1.90 \times 10^{-9} \pm 26\%$ stat.
Combined MC	$3.59 \times 10^{-9} \pm 28\%$ stat.	$3.09 \times 10^{-9} \pm 25\%$ stat.
Data	$\mathbf{4.13 \times 10^{-9}} \pm 21\%$ (stat.) $\pm 100\%$ (syst.)	$\mathbf{1.48 \times 10^{-8}} \pm 21\%$ (stat.) $\pm 63\%$ (syst.)

Table 3.3: Extrapolated $Z+$jets background estimates in the lowest two signal regions for $\int Ldt = 20.3\mathrm{fb}^{-1}$. The fractional difference between the extrapolated values from $Z+$jets MC and the full background MC are assigned as systematic errors in the respective channels. Statistical errors are propagated by the fitted parameter uncertainties.

3.1.6 Results

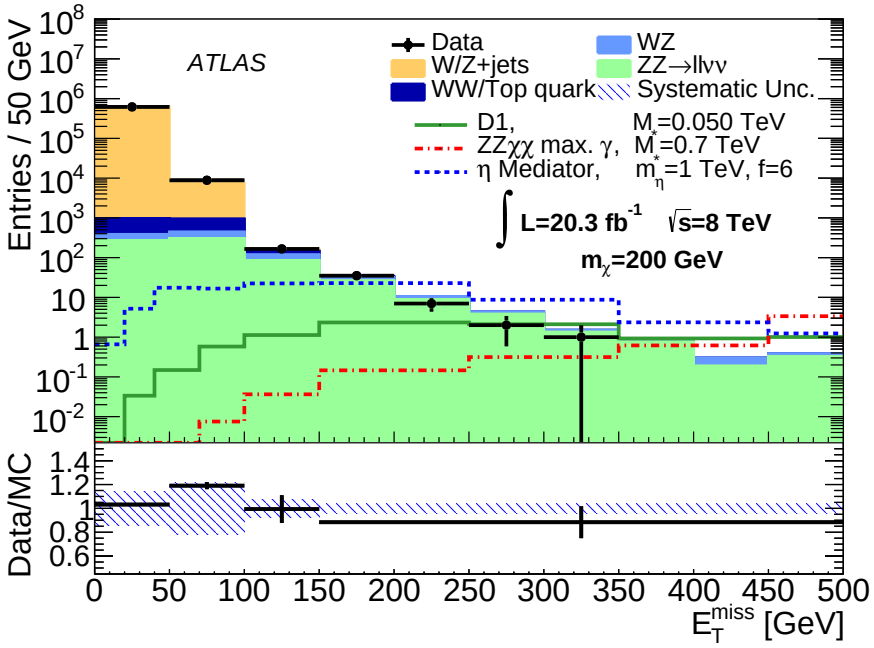

Figure 3.12: Final $E_{\mathrm{T}}^{\mathrm{miss}}$ distribution observed in data for combined $ee, \mu\mu$ channels, after all selections applied as in Section 3.1.3. The rightmost bin includes all events with $E_{\mathrm{T}}^{\mathrm{miss}} >$ 450 GeV. Expected SM backgrounds from MC are included for reference, along with MC distributions of selected signal hypotheses.

No excess over the predicted SM background in any of the $E_{\mathrm{T}}^{\mathrm{miss}}$ regions is observed. Upper limits on the number of possible events N^{lim} originating from non-SM processes consistent with this observation are calculated by constructing a profile likelihood ratio [67] from the unbinned yields and uncertainties in each signal region. This limit is independent of the particular BSM model, but can be converted into an upper limit on the cross section of a given model with the relation:

$$\sigma^{lim} = \frac{N^{lim}}{\mathcal{L} \times \epsilon A} \tag{3.12}$$

where ϵA represents the product of signal reconstruction efficiency and the fiducial acceptance of the signal region, which will depend on the signal model and signal region in question.

In the case of the EFT models, the cross section for a given sample will scale as

$$\sigma_{\mathrm{EFT}} \sim \left(\frac{1}{\Lambda}\right)^{2p} \sigma_0 \tag{3.13}$$

for some fixed constant σ_0 depending on the details of the matrix element and the fiducial phase space, and power p depending on the coefficient of the relevant Lagrangian term. Hence, for a particular sample generated with scale parameter Λ_{gen} resulting in some cross section σ_{gen}, we may convert the cross section limit into a corresponding limit on the scale parameter of the theory:

$$\Lambda_{lim} = \left(\frac{\sigma_{gen}}{\sigma_{lim}}\right)^{1/2p} \Lambda_{gen} \tag{3.14}$$

These limits are shown in Figure 3.13. Using the method of Ref. [56], it is possible to interpret these limits as limits on χ-nucleon scattering cross sections in the limit of momentum transfer $Q^2 \to 0$. This allows the results to be compared with existing direct-detection searches, as shown in Figure 3.14.

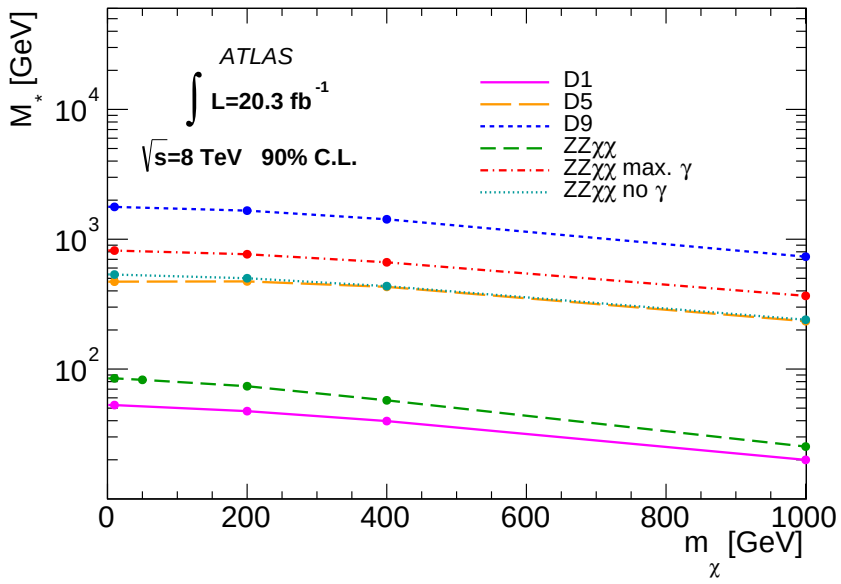

Figure 3.13: Observed 90% C.L. lower limits on the suppression mass scale (here denoted M_*) vs. m_χ for the EFT theory models.

An *upper* limit on the coupling f of the scalar-mediator model is also calculated in a manner

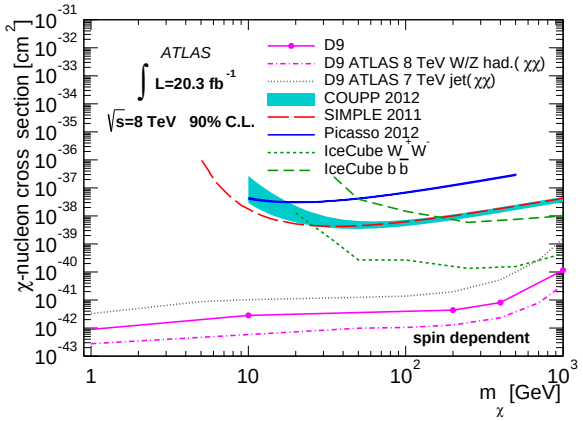

(a) Spin-dependent limits from mass-scale limits on the D9 operator. Published results from ATLAS hadronic $W/Z + E_{\mathrm{T}}^{\mathrm{miss}}$ [55] and mono-jet [40], COUPP [68], SIMPLE [69], PICASSO [70], and IceCube [71], are included for comparison.

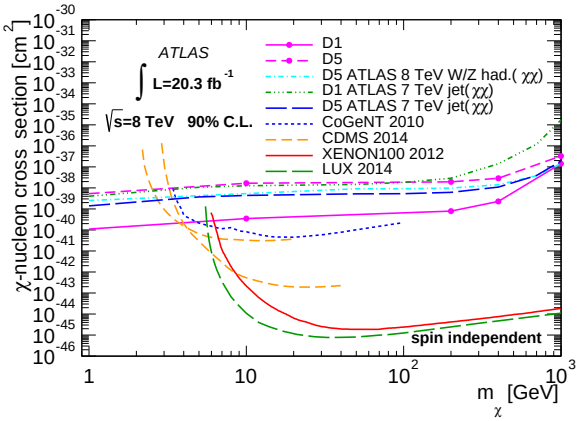

(b) Spin-independent limits from mass-scale limits on the D1 and D5 operators. Published results from ATLAS hadronic $W/Z + E_{\mathrm{T}}^{\mathrm{miss}}$ [55] and mono-jet [40], CoGeNT [72], XENON100 [73], SuperCDMS [74, 75], and LUX [76] are included for comparison.

Figure 3.14: Observed 90% C.L. upper limits on the χ-nucleon scattering cross section as a function of m_χ, as interpreted from the observed EFT mass scale limits using the method of [56]. These limits are compared with the published limits of various direct-detection experiments.

similar to the EFT mass scales; the only difference is in the cross section scaling relation $\sigma \sim f^4$, resulting in a limit defined by:

$$f_{lim} = \left(\frac{\sigma_{lim}}{\sigma_{gen}}\right)^{1/4} f_{gen} \tag{3.15}$$

If we are to assume this model is a viable and complete theory to explain the dark matter observed in the universe today, it must also possess a self-annihilation cross section compatible with the observed relic density [1, 77]. This implies a *lower* limit on the coupling f, which can be calculated for any given (m_χ, m_η). If the lower limit from the relic density constraint is greater than the upper limit from this result, the model is excluded. This exclusion in the (m_χ, m_η) plane is shown in Figure 3.15.

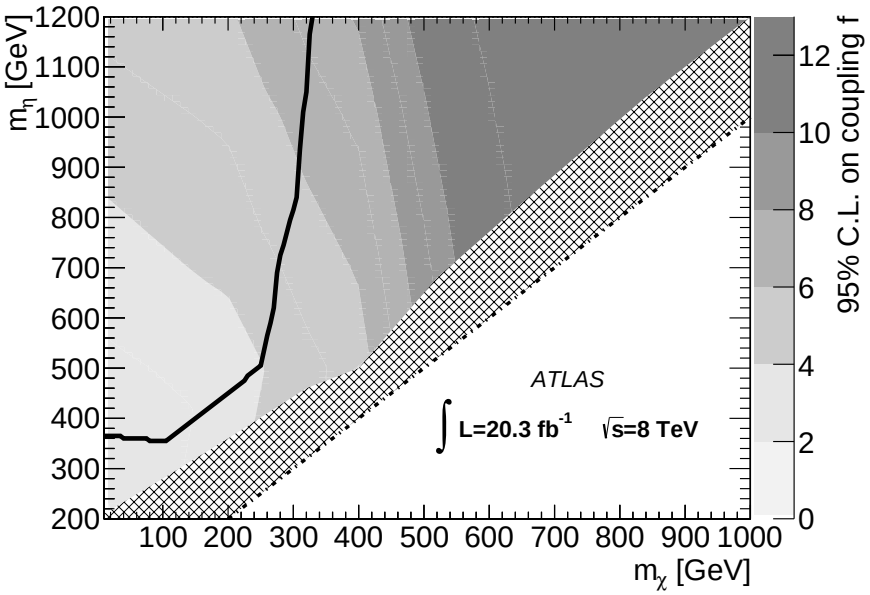

Figure 3.15: Observed 95% C.L. limits on the coupling constant f of the scalar-mediator theory in the (m_χ, m_η) plane. The white region, where $m_\chi > m_\eta$, is forbidden in order to maintain the stability of the dark matter species χ. The upper-left corner, bounded by the black line, is the region excluded because of tension with lower limits required by the thermal relic abundance. The hatched region is not studied in this analysis but remains valid parameter space.

3.2 Search for Dark Matter Production in Association with a Higgs Boson

In Ref. [78], we explore the phenomenology of dark matter pair production in association with a 125 GeV Higgs boson in collision events at the LHC. From an experimental perspective, this is a natural progression of the mono-X collider dark matter program, as such searches have been performed for $X = g, \gamma, W, Z$, that is, all previously known fundamental bosons in the Standard Model. With the confirmation of the existence of the Higgs boson, it remains the only probe that has not yet been explored. As discussed in the introduction to this chapter, we do not expect the Higgs+$E_{\mathrm{T}}^{\mathrm{miss}}$ final state to be competitive with mono-jet and mono-photon searches in the case where the visible probe is merely radiated from the interaction via a standard model vertex. Instead, we consider the case in which the Higgs

field is involved directly in the dark matter interaction, ensuring the presence of a visible Higgs probe in the final state.

In addition to these experimental considerations, many DM candidates have been proposed as a natural consequence of new physics at the EWSB scale [1, 79]. Moreover, in the so-called "WIMP miracle", a weakly-coupled DM particle with mass at this scale naturally explains the relic abundance of dark matter in the universe [3]. To this end, a suite of phenomenological models describing possible DM-Higgs interactions is introduced in Section 3.2.1.

The remaining discussion in Sections 3.2.3–3.2.7 focuses on the implementation of the first ever experimental search in this channel. This search is performed with the ATLAS detector with 20.3 fb^{-1} of pp collision data at $\sqrt{s} = 8$ TeV. The results of this search are published in Ref. [80].

3.2.1 Signal Models

Unlike in other mono-X searches, the possibility for Higgs bosons to be radiated from the initial state is quite negligible owing to its very small mass-dependent couplings to the quarks. Hence, models of direct $qq\chi\chi$ contact interactions wherein the visible object is produced from ISR are not considered in this case, as existing channels such as mono-jet would be much more sensitive. Instead, in all cases considered here, the DM couples to SM particle via a vertex involving a Higgs boson, for example as illustrated in Figure 3.16. As in the previous sections, we consider two classes of signal models: effective field theories (EFTs) and simplified UV-complete models.

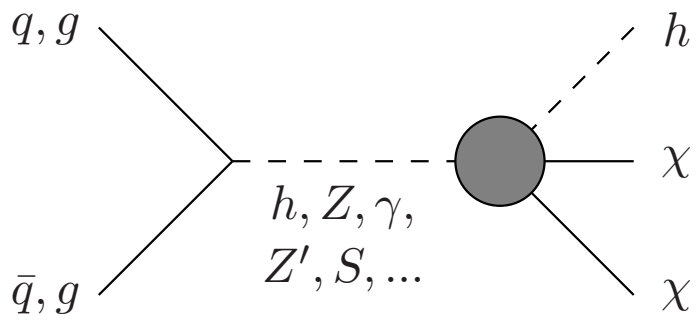

Figure 3.16: A diagram illustrating an effective operator (represented by the shaded gray circle) that couples dark matter to the Higgs boson and producing a mono-Higgs signature at the LHC.

EFT Models

The simplest operators involve coupling DM particles to the Higgs boson through the Higgs portal $|H|^2$ [81–87]. The most straightforward example occurs at dimension-4, with the interaction term:

$$\lambda |H|^2 \chi^2. \tag{3.16}$$

Here χ is a real scalar field and λ a dimensionless coupling constant.

For the case of a (Dirac) fermion DM field χ, the simplest Higgs portal interactions are the dimension-5 operators:

$$\frac{1}{\Lambda}|H|^2 \bar{\chi}\chi, \quad \frac{1}{\Lambda}|H|^2 \bar{\chi} i\gamma_5 \chi. \tag{3.17}$$

The suppression scale Λ has units of mass and represents the scale at which such an interaction would be realized in a UV-complete theory.

In both these cases the mono-Higgs signal can arise from the process $gg \to h^* \to h\chi\chi$. However, these operators also induce a $h \to \chi\chi$ decay mode, whenever $m_\chi < m_h/2$. Preexisting constraints [88] on the $h \to$invisible branching ratio of $\mathcal{B}_{\text{inv}} < 38\%$ imply that we must have $\lambda < 0.016$ and $\Lambda > 10$ TeV for the real and fermion DM models, respectively. As we shall see, the expected mono-Higgs signal is simply not sensitive to this level of suppressed cou-

plings. In the case where $m_\chi > m_h/2$, the invisible Higgs decay is kinematically forbidden, and therefore the allowed couplings are bounded above only by the perturbative limit.

At dimension-6, several effective operators involving h-Z-DM coupling are possible; For the case of scalar DM we have

$$\frac{1}{\Lambda^2}\chi^\dagger i\overleftrightarrow{\partial\mu}\chi H^\dagger i D_\mu H, \tag{3.18}$$

and for Dirac DM

$$\frac{1}{\Lambda^2}\bar{\chi}\gamma^\mu\chi H^\dagger i D_\mu H, \quad \frac{1}{\Lambda^2}\bar{\chi}\gamma^\mu\gamma_5\chi H^\dagger i D_\mu H. \tag{3.19}$$

Expanding the Higgs doublet and covariant derivative in the unitary gauge, the Higgs bilinear term becomes

$$\frac{1}{\Lambda^2}H^\dagger i D_\mu H \;\rightarrow\; -\frac{g_2 v^2}{4 c_w \Lambda^2} Z_\mu \left(1+\frac{h}{v}\right)^2, \tag{3.20}$$

where g_2 is the $SU(2)_{\rm L}$ gauge coupling and c_w is the cosine of the weak mixing angle.

With these dimension-6 operators the mono-Higgs arises from the process $qq \to Z^* \to h\chi\chi$. However, in analogy with the dimension-4/5 cases, these operators imply a $Z \to \chi\chi$ decay mode when $m_\chi < m_Z/2$, which is constrained by measurements of the $Z \to$invisible decay width [89]. These constraints impose an *a priori* bound of $\Lambda > 400$ GeV for the scalar model and $\Lambda > 500$ GeV for the fermion model.

Finally, at dimension-8 many operators can be constructed involving additional SM fields. We consider one such operator,

$$\frac{1}{\Lambda^4}\bar{\chi}\gamma^\mu\chi B_{\mu\nu} H^\dagger D^\nu H, \tag{3.21}$$

where the DM field χ is a fermion and $B^{\mu\nu}$ is the SM $U(1)_{\rm Y}$ field strength tensor. When expanded, this generates the mono-Higgs signal via the process $qq \to Z^*/\gamma^* \to h\chi\chi$.

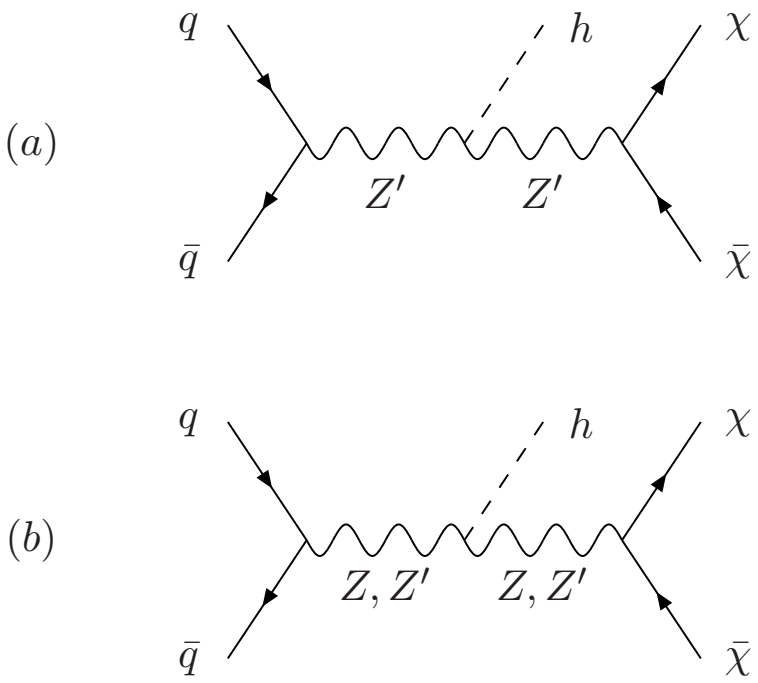

Figure 3.17: Diagrams showing possible mono-Higgs production modes in a simplified model including a Z' boson which decays to $\chi\bar{\chi}$.

Simplified Models

In addition to the above EFTs, we explore simplified models representative of scenarios where the dark and visible sectors are coupled through a new massive mediator particle. This particle may be either a vector (Figure 3.17) or a scalar (Figure 3.18). Mono-Higgs signals are a prediction of these scenarios when the new mediator is allowed to couple to the Higgs boson.

The Z' vector boson is a common feature of many BSM models, arising as a minimal extension of the gauge structure of the SM [90]. In scenarios where the DM couples to the SM only via the Z', the associated $U(1)'$ symmetry ensure the DM particle's stability, making it a natural starting place for model building. For our simplified model, we suppose that the baryon number B is gauged and that the DM particle χ carries baryon number. The resulting leptophobic Z' is then the gauge boson associated with the $U(1)_B$ symmetry, coupling to both quarks and χ. Although generally extending the standard model to include

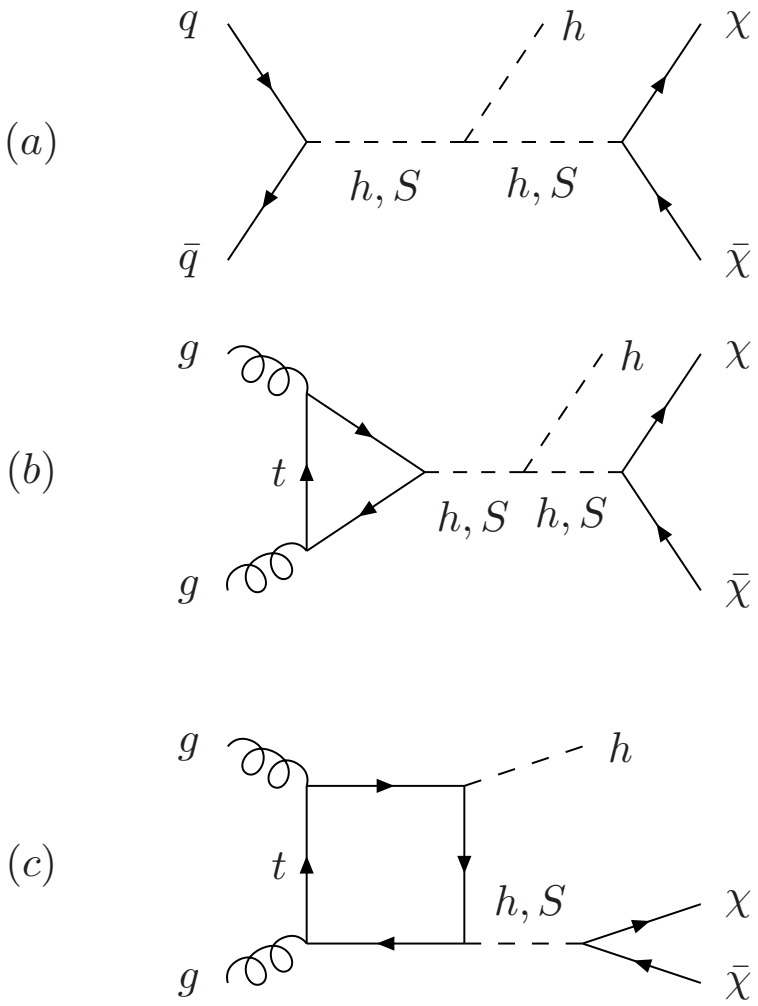

Figure 3.18: Diagrams showing possible mono-Higgs production modes in a simplified model including a scalar S boson which decays to $\chi\bar{\chi}$.

$U(1)_B$ introduces gauge anomalies, these anomalies can be canceled by the judicious addition of extra fermion fields [91]. Often the consistency of such theories implies the existence of stable baryonic states that are neutral under the SM gauge groups, providing excellent DM candidates [92, 93].

The relevant interaction term of the Lagrangian, coupling the quarks to either scalar or fermion DM is

$$g_q \bar{q} \gamma^\mu q Z'_\mu + \begin{cases} i g_\chi \chi^\dagger \overleftrightarrow{\partial^\mu} \chi Z'_\mu + g_\chi^2 |\chi|^2 Z'_\mu Z'^\mu & \text{(scalar)} \\ g_\chi \bar{\chi} \gamma^\mu \chi Z'_\mu & \text{(fermion)} \end{cases} . \tag{3.22}$$

The Z' couplings to quarks and DM are related to the $U(1)_B$ gauge charge g_B by $g_q = g_B/3$ and $g_\chi = B_\chi g_B$, where B_χ is the baryon charge of the χ field.

So far it is not obvious how the Higgs field interacts with these particles. To generate the Z' mass, we can introduce a "baryonic Higgs" to spontaneously break $U(1)_B$ with a vacuum expectation value v_B. In the unitary gauge this results in a physical scalar particle h_B and term

$$\frac{1}{2} m_{Z'}^2 \left(1 + \frac{h_B}{v_B}\right)^2 Z'_\mu Z'^\mu \tag{3.23}$$

coupling this baryonic Higgs to the Z'. Generically, h_B will mix with the SM Higgs boson, giving rise to an interaction term

$$- g_{hZ'Z'} h Z'_\mu Z'^\mu, \qquad g_{hZ'Z'} := \frac{m_{Z'}^2 \sin\theta}{v_B} , \tag{3.24}$$

where the mixing angle θ is a free parameter describing the extent of $h - h_B$ mixing. This $hZ'Z'$ vertex allows the SM Higgs to be radiated from the s-channel state during DM production as shown in Figure 3.17.

The scalar mediator S is handily motivated by the fact that it is simple to write down a

potential for such particles that couple to the SM only through the Higgs. The relevant terms included in the potential are

$$a|H|^2 S + b|H|^2 S^2 + \lambda_h |H|^4 \,, \tag{3.25}$$

where the couplings a, b are free parameters and λ_h is the usual Higgs quartic self-coupling. No other vertices with SM fields are allowed due to gauge invariance. We diagonalize the two scalars by a field rotation defined by

$$h \to c_\theta h + s_\theta S, \quad S \to c_\theta - s_\theta h \,, \tag{3.26}$$

where the angle θ is defined by $\sin 2\theta = 2av/(m_S^2 - m_h^2)$. If we then assume the simplest case of Yukawa coupling of the scalar S to the DM field with coupling strength y_χ, the new scalar vertices become

$$- y_\chi \bar{\chi}\chi(c_\theta S - s_\theta h) - \frac{m_q}{v}\bar{q}q(c_\theta h + s_\theta S) \,. \tag{3.27}$$

The mixing angle θ is constrained by existing Higgs data. Current measurements are consistent with $\cos\theta = 1$ to within $\sim 10\%$ [88, 94–97], corresponding to an upper bound of about $\sin\theta < 0.4$.

The remaining terms from the Higgs potential coupling the h and S together $(h^2 S, S^2 h)$ allow radiation of a Higgs from the S-channel, as shown in Figure 3.18 (a) and (b). Finally, in order to account for Higgs radiation directly from the top-quark loop (Figure 3.18 (c)), the model includes an effective $gghS$ vertex derived in the large m_t limit [78].

3.2.2 Monte Carlo Samples

For all $H + E_{\mathrm{T}}^{\mathrm{miss}}$ signal models, events are simulated with MadGraph5 [58] version 1.4.8.4, with showering and hadronization modeled by PYTHIA 8.1 [60] with the AU2 tune [61]. In each model, the dark matter mass m_χ is a free parameter. Simulated events generated with values of m_χ ranging from 1 to 1000 GeV are considered.

The standard model WZ and ZH production is modeled with PYTHIA8, for a Higgs boson mass $m_H = 125$ GeV. These samples are normalized to cross sections for WH and ZH calculated at next-to-leading order (NLO) [98], and next-to-next-to-leading order (NNLO) [99] in QCD, respectively, with NLO electroweak corrections [100] in both cases.

All simulated physics events are passed through the full ATLAS detector simulation infrastructure [64] based on GEANT4 [63].

3.2.3 Physics Objects and Event Selection

Events are first selected using a diphoton trigger that requires two photon candidates: one with $E_{\mathrm{T}} > 35$ GeV and a second with $E_{\mathrm{T}} > 25$ GeV. These trigger-level photons satisfy the *loose* identification criteria, described in the subsection on photons below.

Data quality is enforced by applying standard ATLAS event cleaning cuts. These cuts remove problematic events, for example with incomplete detector information, data integrity errors, or power supply trips. Additionally, since this analysis depends on accurate $E_{\mathrm{T}}^{\mathrm{miss}}$ reconstruction, any events which contain jets that are known to be poorly measured are removed.

Events are then required to contain at least two reconstructed loose photons with $E_{\mathrm{T}} > 25$ GeV and $|\eta| < 2.37$, excluding the transition region $1.37 < |\eta| < 2.37$ between the barrel

and end-cap calorimeters. Of these photons, the two with the highest p_{T} define the *Higgs candidate*, with invariant mass $m_{\gamma\gamma}$ and transverse momentum $p_{\mathrm{T}}^{\gamma\gamma}$.

In lieu of the default primary vertex definition used by most ATLAS analyses, the two photons selected for reconstruction of the Higgs candidate are used to locate the primary vertex of the event. This was found to improve the diphoton mass resolution and track isolation performance. The determination of this vertex is based on the photon pointing, where the vertex position along the beam axis is determined by combining the trajectories of each photon, measured using the longitudinal segmentation of the calorimeter, as well as the position of the photon conversion vertex if tracks from the conversion have hits in the silicon ID layers. The final vertex is chosen based on this pointing by an artificial neural network algorithm, described in Ref. [101], which also takes as input information about the other ID tracks and their relative azimuthal coordinates.

The Higgs candidate photons are then corrected relative to this vertex, and required to pass additional isolation and tight identification requirements as described below. Finally, the two candidate photons must satisfy the following kinematic requirements:

$$\begin{aligned} p_{\mathrm{T}}^{\gamma_1} &> 0.35 m_{\gamma\gamma} \\ p_{\mathrm{T}}^{\gamma_2} &> 0.25 m_{\gamma\gamma} \\ 105 \text{ GeV} < m_{\gamma\gamma} &< 160 \text{ GeV} \,. \end{aligned}$$

Lastly, events are required to have

$$\begin{aligned} E_{\mathrm{T}}^{\mathrm{miss}} &> 90 \text{ GeV} \\ p_{\mathrm{T}}^{\gamma\gamma} &> 90 \text{ GeV} \,. \end{aligned}$$

The high $E_{\mathrm{T}}^{\mathrm{miss}}$ threshold greatly reduces the fake-$E_{\mathrm{T}}^{\mathrm{miss}}$ backgrounds caused by errors in the

calorimetry rather than invisible particles, while the symmetric requirement on $p_{\mathrm{T}}^{\gamma\gamma}$ helps to enforce the momentum balance expected in our signal events.

The main analysis-level physics objects for this study are of course the photons and $E_{\mathrm{T}}^{\mathrm{miss}}$, both of which have slightly modified reconstruction relative to the ATLAS standard. They are described in the following two subsections.

Photons

As described in previous section, photon reconstruction is seeded from topological clusters of energy deposits in the electromagnetic calorimeter. These clusters are matched against tracks reconstructed in the inner detector, and classified as electrons, converted photons, and unconverted photons. The energies of the clusters are calibrated separately for converted and unconverted photons candidates using an MVA calibration tool to account for energy losses upstream of the calorimeter and for energy leakage outside the cluster cells. A photon cleaning prescription is also applied that removes clusters with a significant contribution of energy from detector cells known to give poor measurements. In addition, the energy measurement of converted photons is improved with corrections based on MC simulations modeling the radius of conversion.

Reconstructed photons used in analysis are further categorized against two reference sets of cuts: *loose* and *tight*. These provide two working points to impose separation between isolated photons and fake signatures from QCD jets and are described in detail in Ref. [19]. The *loose* photon cuts are based on shower shapes in the second layer of the electromagnetic calorimeter, as well as energy deposition in the hadronic calorimeter, and are also used at trigger level. *Tight* identification cuts adds information from the finely segmented strip layer of the calorimeter, which provides good rejection of hadronic jets where a neutral meson carries most of the energy.

The longitudinal position of the diphoton vertex identified for the event is then used to correct the η coordinate (and consequently, the p_{T}) of the photons.

To further suppress hadronic backgrounds, the two photons selected for reconstruction of a Higgs candidate are required to satisfy track and calorimeter isolation requirements. The scalar sum of the p_{T} of tracks with $p_{\mathrm{T}} > 1$ GeV originating from the diphoton vertex and within $\Delta R < 0.2$ of the photon must be less than 2.6 GeV. The total calorimetric energy within a cone of $\Delta R < 0.4$ around the photon (but excluding the energy from the photon cluster itself) is required to be less than 6 GeV.

Missing Transverse Energy

The $E_{\mathrm{T}}^{\mathrm{miss}}$ is reconstructed using calibrated objects identified in the event, as described in previous sections. However, for this analysis three modifications have been made:

1. Photons are given priority over electrons. This prevents conversion photons from being counted as electrons in the $E_{\mathrm{T}}^{\mathrm{miss}}$.

2. Photons are required to pass *tight* identification cuts identical to those used for the Higgs candidate photons.

3. Topo-clusters for photons are calibrated using the same photon-specific tunes as for the analysis objects, rather than the generic EM scale.

3.2.4 Backgrounds

The largest background, before cutting aggressively on $E_{\mathrm{T}}^{\mathrm{miss}}$, is due to diphoton production. This background is nonresonant, producing a smooth, monotonically decreasing continuum of events in $m_{\gamma\gamma}$. The $p_{\mathrm{T}}^{\gamma\gamma}$ of the diphoton system in these events must be balanced by

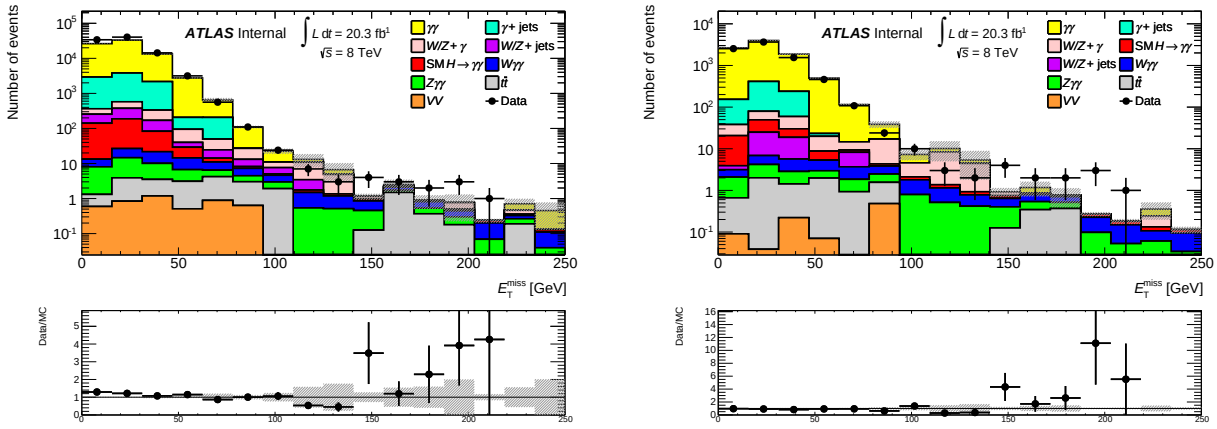

(a) (b)

Figure 3.19: Comparison of the $E_{\mathrm{T}}^{\mathrm{miss}}$ distributions for data vs. MC. In (a), neither the $p_{\mathrm{T}}^{\gamma\gamma}$ nor $E_{\mathrm{T}}^{\mathrm{miss}}$ cuts have been applied. In (b), a cut of $p_{\mathrm{T}}^{\gamma\gamma} > 70$ GeV is applied.

QCD radiation of one or more jets. The $E_{\mathrm{T}}^{\mathrm{miss}}$ in these events does not originate from invisible particles but rather from imperfect calorimeter measurements of these additional jets. Nonetheless, the cross sections are very large so a great number of events will appear in the region of $m_{\gamma\gamma}$ near 125 GeV. The second largest background is the production of single-photon+jets, where one of the jets fake a photon. As with the diphoton process, the observed $E_{\mathrm{T}}^{\mathrm{miss}}$ from these events is fake.

In Figures 3.19 and 3.20, the $E_{\mathrm{T}}^{\mathrm{miss}}$ and $p_{\mathrm{T}}^{\gamma\gamma}$ distributions for the different processes are shown, demonstrating the excellent suppression of $\gamma(\gamma) + \mathrm{jets}$ relative to other backgrounds above roughly 100 GeV. In Figure 3.21, the diphoton mass distribution is compared for different levels of cuts on $E_{\mathrm{T}}^{\mathrm{miss}}$ and $p_{\mathrm{T}}^{\gamma\gamma}$ to provide an impression of effect of these cuts as they approaching the signal region.

Other continuum backgrounds include $(W/Z) + (\gamma/\mathrm{jets})$, which require lepton or jets faking photons; and $W/Z + \gamma\gamma$, with either neutrinos or missed leptons. These backgrounds are comparable to the $\gamma(\gamma) + jets$ background in the high-$E_{\mathrm{T}}^{\mathrm{miss}}$, high-$p_{\mathrm{T}}$ signal region; however, they are difficult to model in this region due to very limited MC statistics, and the relatively poor simulation of fakes. As discussed in Section 3.2.5, our measurement strategy will

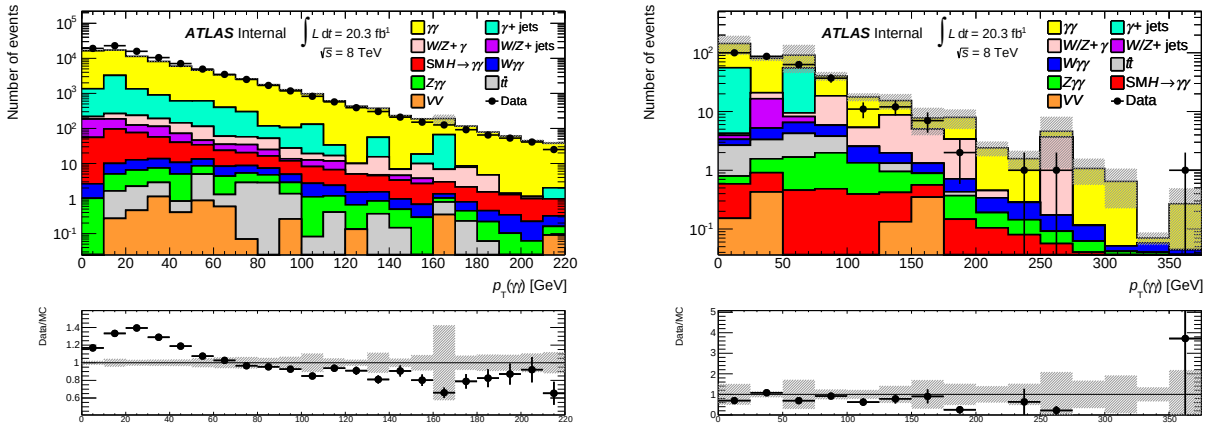

(a) (b)

Figure 3.20: Comparison of the $p_{\mathrm{T}}^{\gamma\gamma}$ distributions for data vs. MC. In (a), neither the $p_{\mathrm{T}}^{\gamma\gamma}$ nor $E_{\mathrm{T}}^{\mathrm{miss}}$ cuts have been applied. In (b), a cut of $E_{\mathrm{T}}^{\mathrm{miss}} > 70$ GeV is applied. Note that while some significant disagreement is apparent below $p_{\mathrm{T}}^{\gamma\gamma} \sim 60$ GeV, we are only concerned with events in our signal region at a higher p_{T}; moreover, these MC models are not used in the final result.

automatically provide a purely data-driven estimate of the sum total of all these backgrounds, so it is not necessary to accurately model the exact composition in MC.

The remaining backgrounds are those due to the SM production of a true Higgs boson. Although the cross sections for these processes are quite small, the resonant $m_{\gamma\gamma}$ signal is localized around $m_h = 150$ GeV. The relevant production modes are $H(\gamma\gamma) + \text{jets}$, which produces fake $E_{\mathrm{T}}^{\mathrm{miss}}$, and $H(\gamma\gamma) + W/Z$, which produces real $E_{\mathrm{T}}^{\mathrm{miss}}$ from neutrinos. Because this MC is ultimately used to estimate the yield of non-BSM events in the signal region, we must quantify the uncertainty of this yield due to theoretical errors and due to systematic differences between MC and real data.

The theoretical uncertainties on the WH and ZH production cross sections come from varying the renormalization and factorization scales and from uncertainties on the parton distribution functions [102–104] following the PDF4LHC [105] prescription. The branching fraction $H \to \gamma\gamma$ is taken from HDECAY [106] with NNLO corrections [107], with uncertainties provided by the LHC Higgs Cross Section Working Group [108, 109]. The total

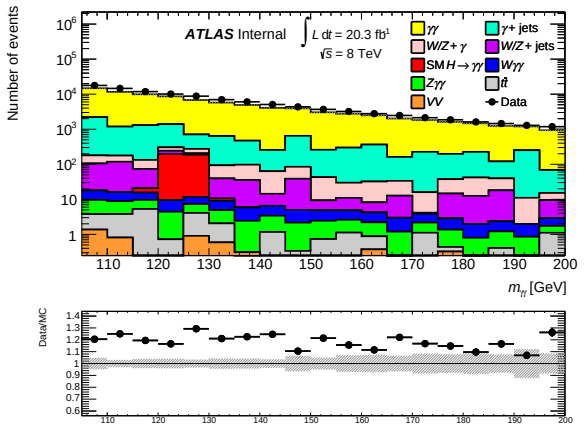

(a) No cuts

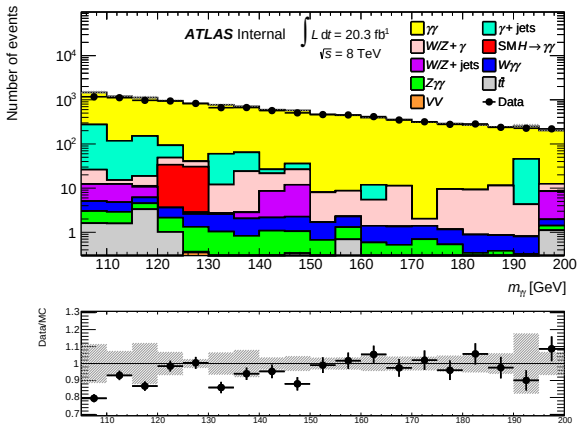

(b) $p_{\mathrm{T}}^{\gamma\gamma} > 70$ GeV

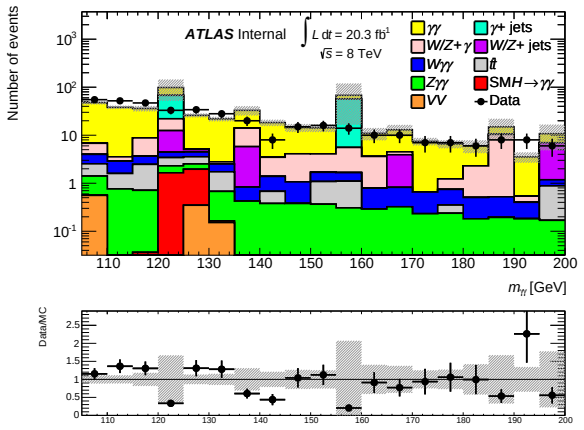

(c) $E_{\mathrm{T}}^{\mathrm{miss}} > 70$ GeV

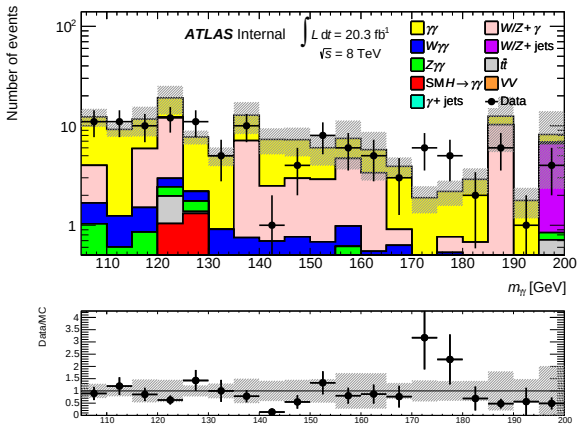

(d) $p_{\mathrm{T}} > 70$ GeV and $E_{\mathrm{T}}^{\mathrm{miss}} > 70$ GeV

Figure 3.21: Distributions of $m_{\gamma\gamma}$ in data and MC for various cuts applied on $p_{\mathrm{T}}^{\gamma\gamma}$ and $E_{\mathrm{T}}^{\mathrm{miss}}$ to illustrate the effect the signal region selection has on backgrounds.

Source	Uncertainty
Trigger	0.2%
Photon ID	2.1%
Photon Isolation	2.8%
PES	1.12%
PER	0.17%
JES	0.29%
JER	0.60%
MET Soft Terms	1.0%
Total (detector)	3.9%
Luminosity	2.8%

Table 3.4: Summary of experimental uncertainties for H+$E_{\mathrm{T}}^{\mathrm{miss}}$ MC assessed in the analysis.

theoretical uncertainty on the SM $H + E_{\mathrm{T}}^{\mathrm{miss}}$ contribution is 6%.

To estimate the experimental systematics introduced by the MC modeling of the detector, we identify the and assess the uncertainties of quantities used in the modeling of the detector response, such as trigger efficiencies and calorimeter energy scales. These quantities are then varied within the range of their uncertainties to provide a new version of each event. For each variation, the impact on the final quantity of interest, the event yield, is evaluated. The source of all non-negligible systematics and their associated fractional uncertainty on the MC event yield prediction are listed in Table 3.4.

3.2.5 Parameterization of $m_{\gamma\gamma}$ Shapes

A key feature of this analysis is the fit of the $m_{\gamma\gamma}$ observed in data to parametric background and signal shapes. For this, we construct a model consisting of three components: one monotonic continuum function representing the non-resonant backgrounds in aggregate, and two localized "peak" functions with independent normalization, representing the resonant shape of the SM Higgs background and BSM signal.

Continuum Background Model

The non-resonant continuum backgrounds are jointly modeled by a single exponential function,

$$f_{\mathcal{C}}(x) := N \exp(-x/\tau)\,, \tag{3.28}$$

where N and τ are the degrees of freedom which will be fit to observations, and x is the placeholder variable for a $m_{\gamma\gamma}$ measurement, provided in units matching those of τ.

Figure 3.22 demonstrates a fit of this function to background-only MC (excluding the resonant SM Higgs backgrounds) in order to validate that this model is able to provide a good of the expected background shape near the signal region. The fit performs well at lower $E_{\mathrm{T}}^{\mathrm{miss}}$ thresholds; at higher $E_{\mathrm{T}}^{\mathrm{miss}}$ thresholds the MC statistics for some BG components are quite poor, resulting in heavily-weighted fluctuations.

We note that any turn-on effects (i.e. non-monotonicity) at the low end of the $m_{\gamma\gamma}$ spectrum at the higher $E_{\mathrm{T}}^{\mathrm{miss}}$ and p_{T} cuts near our signal region would not be modeled well by our choice of function $f_{\mathcal{C}}(x)$. With the limited statistics of our MC model, we are unable to confirm whether such an effect is present. Instead, we perform a fit to the MC sample for the irreducible $WZ\gamma\gamma$ component of the background; because this MC has real $E_{\mathrm{T}}^{\mathrm{miss}}$, it is easy to obtain very high-statistics samples even at high $E_{\mathrm{T}}^{\mathrm{miss}}$ and p_{T} via generator-level filtering. As the diphotons in this process should be kinematically very similar to the dominant processes, it should inform whether there are issues with $m_{\gamma\gamma}$ turn-on effects in the signal region. These fits are shown in Figure 3.23.

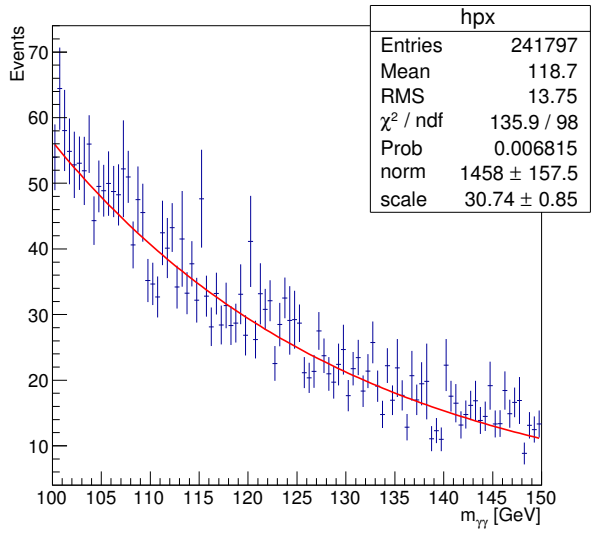

(a) $E_{\mathrm{T}}^{\mathrm{miss}} > 50$ GeV

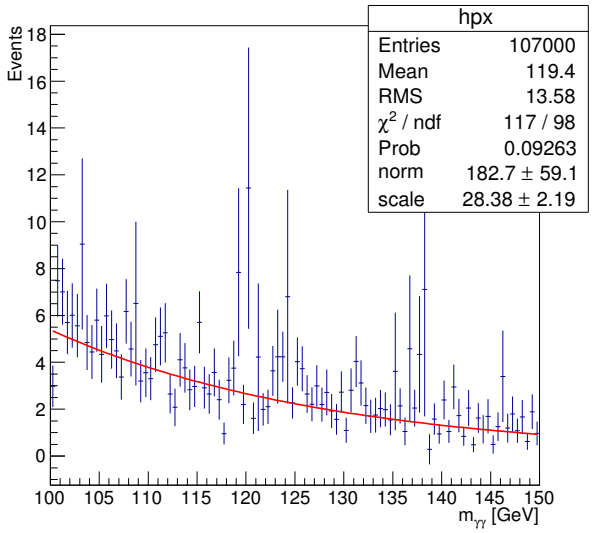

(b) $E_{\mathrm{T}}^{\mathrm{miss}} > 70$ GeV

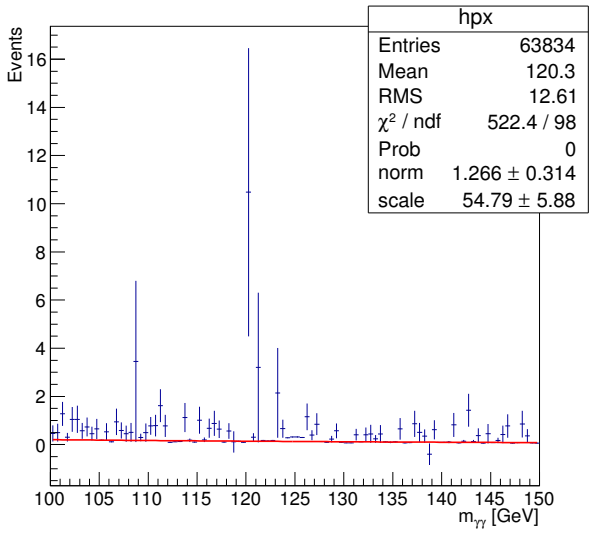

(c) $E_{\mathrm{T}}^{\mathrm{miss}} > 90$ GeV

Figure 3.22: Validation of the parameterized continuum background function fits on simulated events with various $E_{\mathrm{T}}^{\mathrm{miss}}$ thresholds. Note the large fluctuations arise from MC samples with only a small number of heavily-weighted events.

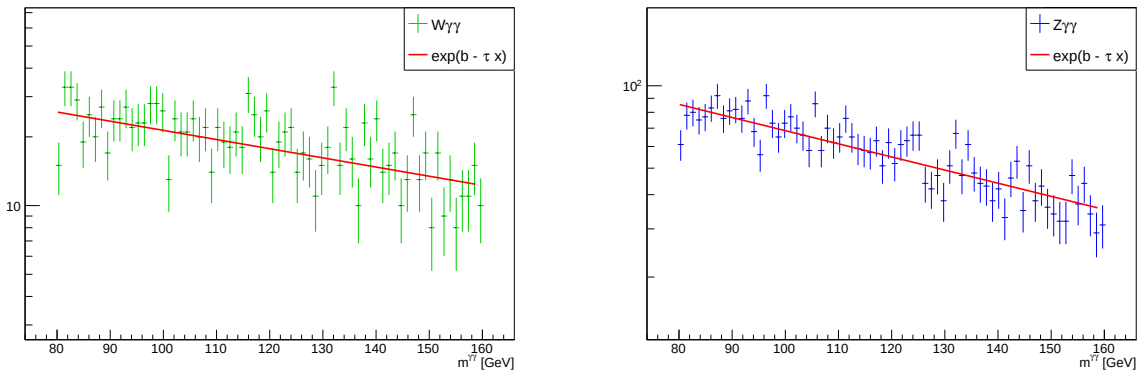

Figure 3.23: Fits of the model $f_{\mathcal{C}}$ to high-statistics $V\gamma\gamma$ MC events in the signal region. These fits clearly demonstrate there is no observable turn-on effects near the diphoton mass range of interest, 105 GeV $< m_{\gamma\gamma} <$ 160 GeV. The normalizations shown in these figures are arbitrary.

Resonant Higgs Model

The $m_{\gamma\gamma}$ profile of both the resonant SM Higgs backgrounds and the BSM signals are modeled as a double-sided Crystal Ball (DSCB) function [110]:

$$f_{\mathcal{H}}(t) = N \cdot \begin{cases} e^{-t^2/2} & \text{if} \quad -\alpha_{Low} < t < \alpha_{High} \\ \frac{e^{-\alpha_{Low}^2/2}}{\left[1-\frac{\alpha_{Low}}{n_{Low}}(\alpha_{Low}+t)\right]^{n_{Low}}} & \text{if} \quad t < -\alpha_{Low} \\ \frac{e^{-\alpha_{High}^2/2}}{\left[1-\frac{\alpha_{High}}{n_{High}}(\alpha_{High}-t)\right]^{n_{High}}} & \text{if} \quad t > \alpha_{High} \end{cases} . \tag{3.29}$$

Here, $t = (m-\mu_{\text{CB}})/\sigma_{\text{CB}}$, where μ_{CB} is the location of the peak's maximum, N is some overall normalization, and σ_{CB} is the observed width of the resonance. The other parameters are illustrated graphically in Figure 3.24. In Figure 3.25, the DSCB function is fitted to MC simulations for some example BSM signal samples. The fit performs well about the Higgs mass peak in MC for both SM Higgs backgrounds and for our signal models.

For the purposes of limit-setting, we fix the parameters $(\alpha_{Low}, n_{Low}, \alpha_{High}, n_{High})$ to their best-fit values from the SM Higgs MC. The gaussian width σ_{CB} is also set to the best-fit value, but allowed to float in the limit during the fit with a gaussian constraint of 11% to account for

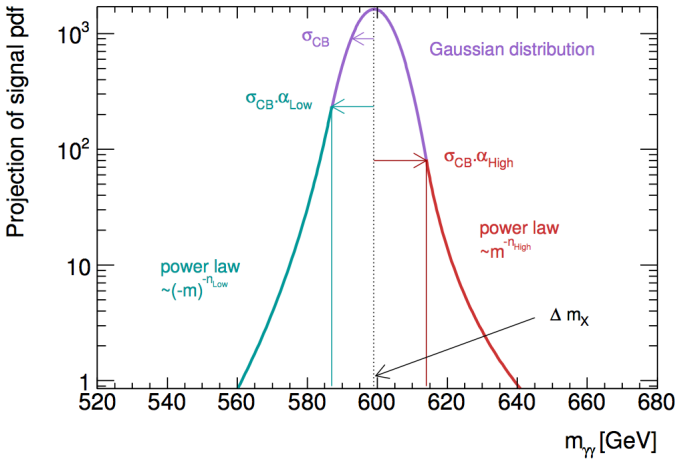

Figure 3.24: Graphical description of the double-sided Crystal Ball function, in this instance for a signal mass of 600 GeV.

systematic uncertainties in the photon energy resolution (PER). Similarly, the peak location μ_{CB} is allowed to float with a constraint of 0.3% to account for the photon energy scale (PES) uncertainty. The values of the parameters α and n fitted to the BSM signals are consistent with those fitted to the SM Higgs to within these uncertainties; therefore we fix these parameters to the values taken from the SM Higgs prediction for all signals.

3.2.6 Fitting and Limits

In this analysis, we can set limits on three types of cross sections. In order of increasing model-independence, they are:

1. **Model cross section:**

   The BSM model cross section σ^p for some model p is the total cross section limit for the specified model, which has theoretical fiducial acceptance A_p and reconstruction efficiency ϵ under the full selection of this analysis. Generally a given model will have free parameters which may be related to this cross section limit, in order to constrain the theoretical space of the model. For the models considered in this analysis, we

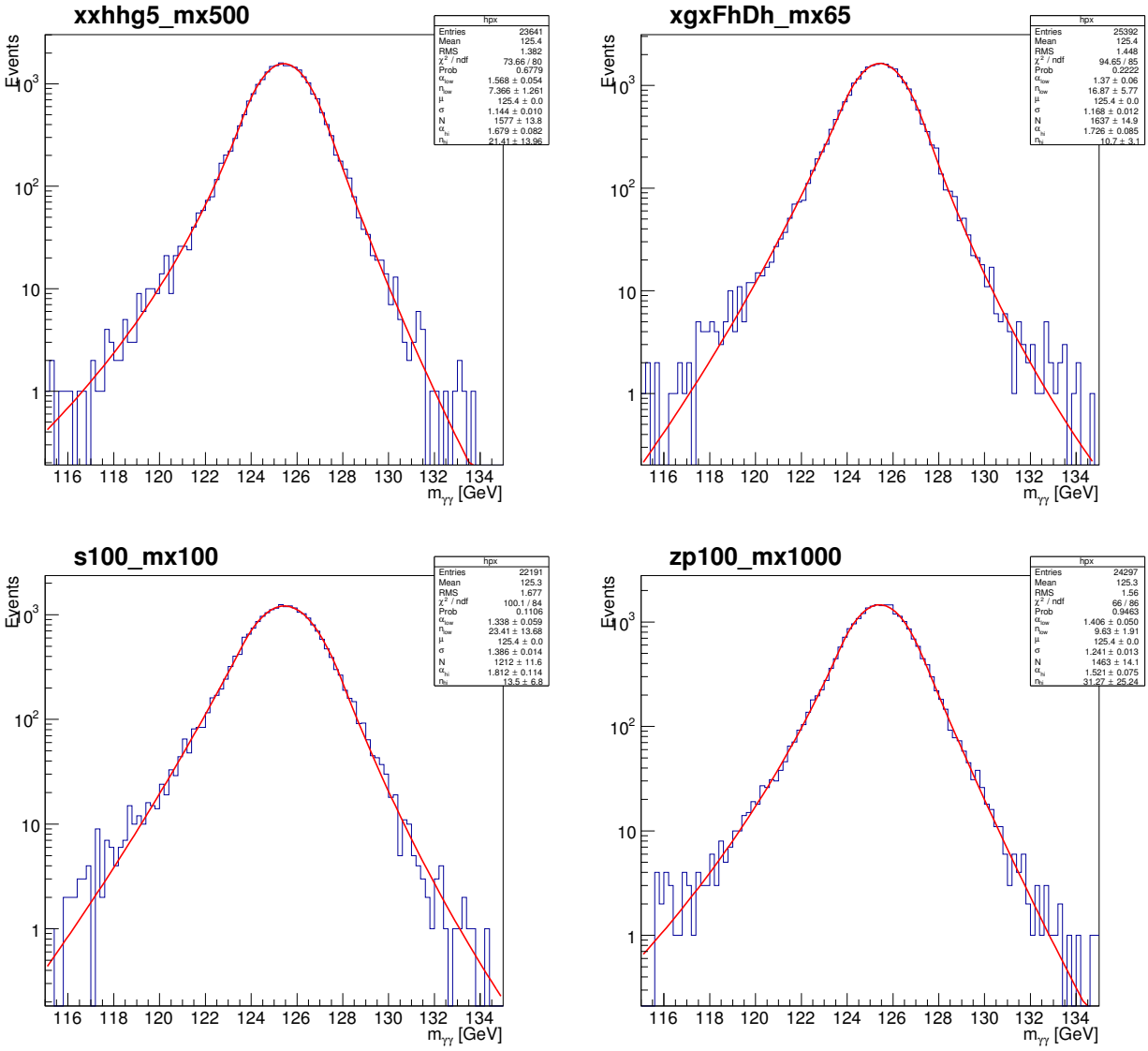

Figure 3.25: Validation of the parameterized signal function (DSCB) against the expected shape from simulated events.

provide interpretation in terms of limits on theoretical parameters in Section 3.2.7.

2. **Fiducial cross section:**

   The fiducial cross section $\sigma^{\text{fid}} = (\sigma^p \times A_p)$ is the limit on BSM $H + E_{\text{T}}^{\text{miss}}$ production cross section over a phase space compatible with our selection criteria, for any models which are expected to have reconstruction efficiencies ϵ in the detector similar to those considered here. The theoretical acceptance A_p is deliberately not factored out of this result, so that readers may apply the acceptance of their own models in order to reinterpret the measurement. Indeed, we cannot factorize A_p from the result without specifying a specific model p.

3. **Visible cross section:**

   The visible cross section $\sigma^{\text{vis}} = (\sigma^p \times A_p \times \epsilon)$ is simply the cross section such that $\mathcal{L} \times \sigma_{\text{vis}}$ is the normalization of the non-SM Higgs component of the observed peak. This result makes no assumption about the underlying physics, except that the shape of the $m_{\gamma\gamma}$ resonance is compatible with the model described in Section 3.2.5. It is therefore the most general measurement, but the most difficult to re-interpret, as the ATLAS detector efficiency ϵ is generally impossible to know without sophisticated MC studies.

All three limits will depend on the observed data, as well as the normalization and uncertainty of the SM Higgs component. The estimate from MC for the SM Higgs visible cross section is

$$\sigma_{\text{SM}}^{predicted} = 5.27 \times 10^{-2}\text{fb} \pm 7.2\%(\text{sys}) \pm 1.0\%(\text{stat})\,. \tag{3.30}$$

With these definitions in mind, we can discuss the statistical model used to extract these limits from the observed data and the SM Higgs background rate. We define an unbinned likelihood with three components, ν_{bkg}, ν_{SM}, and ν_{BSM} which represent the expected number

of events from continuum background, SM Higgs background, and the BSM signal:

$$P(n, \vec{m}|\nu_{\rm BSM}, \nu_{\rm SM}, \nu_{\rm bkg}, \tau) = {\rm Pois}(n|\nu_{\rm BSM} + \nu_{\rm SM} + \nu_{\rm bkg}) \times \prod_{i=1}^{n} \frac{(\nu_{\rm BSM} + \nu_{\rm SM}) f_{\mathcal{H}}(m_i|\mu_{\rm CB}, \sigma_{\rm CB}) + \nu_{\rm bkg} \exp(-m_i|\tau)}{\nu_{\rm BSM} + \nu_{\rm SM} + \nu_{\rm bkg}} \quad (3.31)$$

Here, n is the number of observed events in the signal region and $\vec{m} = (m_1, ..., m_n)$ is the vector of observed values for $m_{\gamma\gamma}$. $f_{\mathcal{H}}$ is the resonance-peak shape function of Equation (3.29), $(\mu_{\rm CB}, \sigma_{\rm CB})$ are the peak location and width, and τ is the free parameter of the continuum background model.

Gaussian constraints are placed on the parameters $(\mu_{\rm CB}, \sigma_{\rm CB})$, and $\nu_{\rm SM}$; the first two are constrained by the PES/PER as discussed in Section 3.2.5. The constraint on $\nu_{\rm SM}$ is necessary to break the degeneracy with $\nu_{\rm BSM}$; it is imposed by substituting with the MC-expected yield

$$\nu_{\rm SM} = \mathcal{L} \cdot \sigma_{\rm SM}^{predicted} \quad (3.32)$$

with the central value and fractional uncertainty on $\sigma_{\rm SM}^{predicted}$ corresponding to those quoted in Equation (3.30). The luminosity $\mathcal{L} = 20.3$ fb^{-1} is also allowed to float within its uncertainty of 2.8%.

The parameter of interest (POI) in the final fit depends on which type of measurement we are interested in. When considering only the absolute event yields, it is sufficient to simply extract the best-fit value of $\nu_{\rm BSM}$. However, in the case of setting limits on one of the above types of cross sections, we must include the appropriate factors (and uncertainties) in the BSM component. To extract the visible BSM cross section, we substitute

$$\nu_{\rm BSM} = \mathcal{L} \cdot \sigma^{\rm vis}\,, \quad (3.33)$$

and $\sigma^{\rm vis}$ is treated as the POI in the likelihood maximization. Thus, the POI is not only scaled

dimensionally to a cross section, but also correctly accounts for the luminosity uncertainty which is correlated with the SM Higgs component.

To extract the fiducial cross section limit σ^{fid}, we substitute

$$\nu_{\text{BSM}} = \mathcal{L} \cdot \sigma^{\text{fid}} \times \epsilon \,, \tag{3.34}$$

and must therefore specify the reconstruction efficiency ϵ to be used in the likelihood maximization. Because the details of reconstruction (such as isolation and momentum resolution) are affected by the kinematic properties of the underlying event, it is impossible to separate this factor entirely from the theoretical differences between various models. For example, a model which predicts consistently higher-p_{T} photons may be more efficiently reconstructed than another model which has softer photons. The models considered in this analysis ranged between 56–65% in reconstruction efficiency, with comparable fractional systematic uncertainties across models. We chose to report a conservative fiducial limit by assuming the lowest efficiency of $\epsilon = 0.56$ with an uncertainty of 3%.

Finally, the model-specific total cross sections σ^p are obtained for each model p by substituting

$$\nu_{\text{BSM}} = \mathcal{L} \cdot \sigma^p \times (A \times \epsilon)_p \,.$$

Here the product $A \times \epsilon$ is considered jointly for each model to properly account for the differences in reconstruction just mentioned.

3.2.7 Results

The final fit to data is shown in Figure 3.26. The best-fit component-wise event yields are 14.2 ± 4.0 for the continuum background, 1.1 ± 0.1 for the SM Higgs, and 2.7 ± 2.2 for BSM Higgs signal. This corresponds to a deviation of 1.4σ over the SM-only hypothesis, using the

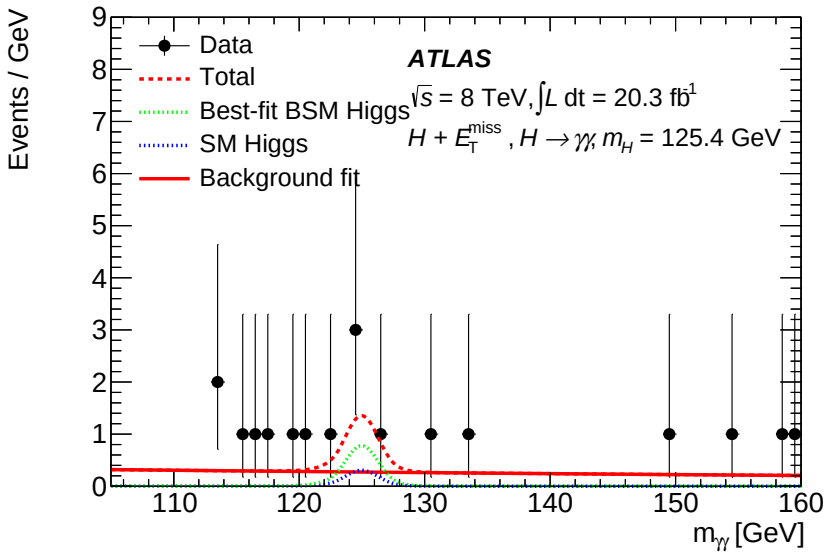

Figure 3.26: The best-fit of the 3-component $m_{\gamma\gamma}$ model over the 18 events observed in the signal region.

asymptotic formulae in Ref. [67]. As the number of BSM events observed do not constitute a statistically significant observation, we proceed to interpret this result as upper bounds on the BSM cross section. These limits are calculated using a one-sided profile likelihood ratio and the CLs technique [111, 112].

The results for the BSM visible and fiducial cross sections at 95% C.L. is

$$\sigma_{95\%}^{\text{vis}} = 0.39 \text{ fb}\,,$$

and the fiducial cross section with $\epsilon = 0.56$ is

$$\sigma_{95\%}^{\text{fid}}\big|_{\epsilon=0.56} = 0.70 \text{ fb}\,.$$

The limits of each individual model-specific cross section are calculated in the same way, and the results are presented as exclusions on the parameters of the model. These parameter exclusions are calculated using the known relationship between the cross section and the

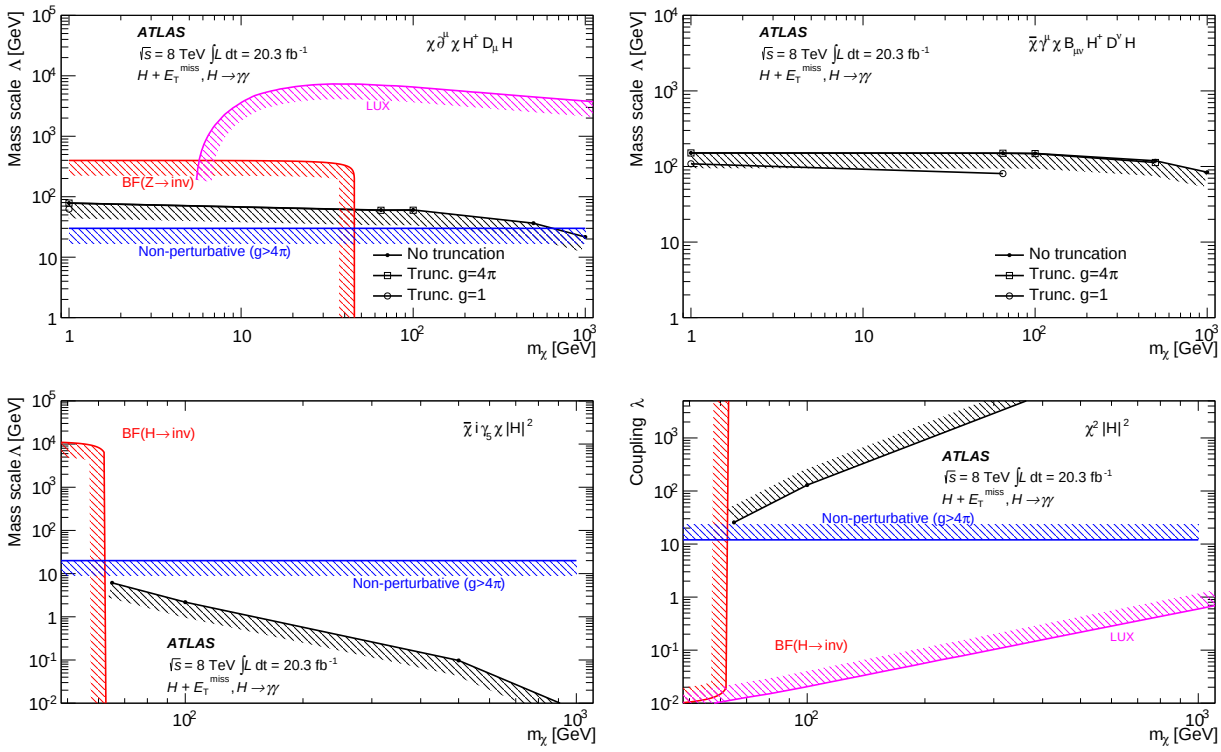

Figure 3.27: Limits at 95% CL on the mass scale Λ and coupling λ as a function of the DM mass m_χ. Solid black lines are the limits from this mono-Higgs analysis. Physical signals due to the dimension-4 operators were found to be beyond the sensitivity of this measurement.

suppression scale Λ or coupling constant λ, as discussed in Section 3.1.6. Figure 3.27 shows the results for the EFT operators, and Figure 3.28 shows the results for the scalar and vector mediator models.

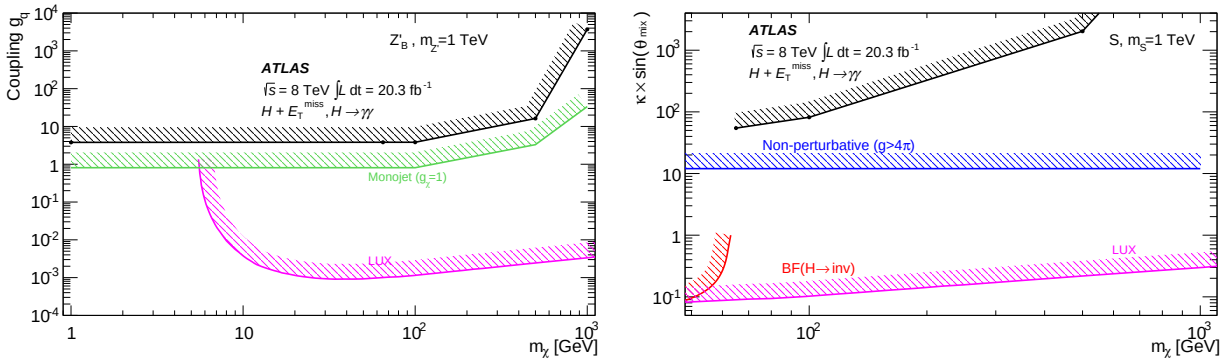

Figure 3.28: Limits on coupling parameters for the simplified models with a heavy mediator mass of 1 TeV. All constraint contours exclude larger couplings or mixing angles.

Chapter 4

A Search Method for Light Hadronic Resonances

Searches for hadronic resonances have been carried out at collider experiments for decades in the dijet channel, wherein peak-shaped features are sought in the invariant mass spectrum of two-jet events [113–118]. From a theoretical perspective, these searches are motivated by a wide range of models [119–123] that predict new s-channel resonances with couplings to quarks and/or gluons. Experimentally, the searches are well motivated because they can be carried out in a relatively model-independent manner and because incremental increases in the center-of-mass collision energy can provide new sensitivity even with limited luminosity.

The upper range of these resonance searches is limited by the center-of-mass energy of the collider. The current measurements at the LHC, therefore, are able to access masses into the TeV range, although no excesses attributable to new physics have been observed. In order to directly probe higher masses, massive investment in new, higher energy colliders is required. The lower range of masses accessible to these searches is imposed by factors that are related not to the physical limitations of the collider, but of the detector.

The ATLAS and CMS detectors employ trigger systems that aggressively remove events, recording only a small fraction of collision events deemed most interesting. Generally the trigger criterion involves a high-energy object above some threshold selected to reduce the rates to levels compatible with the computing and storage facilities available. These triggers correspond to minimum p_{T} thresholds for jets, which results in a lower bound on the dijet sensitivity at a mass of approximately $M = 2p_{\mathrm{T}}$. As a result, recent searches have no sensitivity below several hundred GeV, and no experiment has probed below $M = 300$ GeV using the dijet final state in the past two decades. Indeed, limits on the coupling between quarks and a heavy resonance in this low-mass region are weaker than limits in higher-mass regions [124].

This chapter describes an alternative method, published in [125], of searching for light hadronic resonances, and examines the possible sensitivity to low-mass hadronic resonances available in the existing LHC dataset. We are interested in particles with masses as low as roughly 20 GeV and ranging up to a couple hundred GeV, a region which has not been directly probed by collider measurements. Throughout the discussion, we will assume this resonance is a Z' vector boson decaying to quark-antiquark pairs, although the experimental method is generic to any particle which decays to jets with a narrow width.

The choice of Z' is motivated by many phenomenological models, often arising as a minimal $U(1)$ extension [91, 126, 127] to the gauge structure of the SM or by extending $SU(5)$ to $SO(10)$ [128, 129]. This is in turn motivated by the fact that $U(1)$ subgroups can naturally result from spontaneous symmetry breaking of larger groups such as $SU(N)$ or $E6$ in models which attempt to embed the SM gauge structure within a higher symmetry [90, 130].

We confine our attention to the case of a *leptophobic* Z', that is, one that couples negligibly to leptons. This is required due to stringent limits on leptonically-coupled Z' over a broad range of masses from measurements at LEP and Tevatron [131, 132].

A simple model to incorporate such a Z' is implemented by treating the observed baryon number conservation, which is normally considered an accidental symmetry of the SM, as a gauged symmetry $U_{\mathrm{B}}(1)$ [91, 133–135]. The gauge boson associated with this new $U_{\mathrm{B}}(1)$ is the Z', and it couples exclusively and equally all quarks. The relevant interaction term of the Lagrangian is

$$\mathcal{L} \supset \frac{g_{\mathrm{B}}}{6}\bar{q}\gamma^{\mu}qZ'_{\mu}\,. \tag{4.1}$$

The free parameters of the model are the boson mass $m_{Z'}$, and the quark coupling constant g_{B}, where all quarks have a $g_{\mathrm{B}}/3$ charge under the new $U(1)_{\mathrm{B}}$. This model poses serious theoretical challenges; for example, the new boson introduces gauge anomalies; however these can be canceled for example by introducing new (heavy) fermions [91, 133]. We also leave open the mechanism by which the Z' acquires mass, its kinetic mixing with the hypercharge gauge, and other model-building concerns.

Instead, we focus on the experimental details of performing a direct search for hadronic decays in this mass range. The Z' model will provide a framework for quantitatively reasoning about, for example, the relationship between observed rates and perturbative couplings, and also enables us to easily simulate the details of how such a decay process would appear in the detector.

4.1 Experimental Method

As discussed above, the conventional dijet resonance search method is limited to masses above $\sim 2p_{\mathrm{T}}^{j}$ by the jet trigger threshold p_{T}^{j}. In 2015 the lowest unprescaled single-jet triggers available in ATLAS data had a threshold $p_{\mathrm{T}}^{j} = 360$ GeV, corresponding to a minimum dijet mass of 720 GeV. We propose to eliminate this debilitating connection between signal mass and trigger thresholds by examining events in which the Z' is boosted with a large p_{T}. This

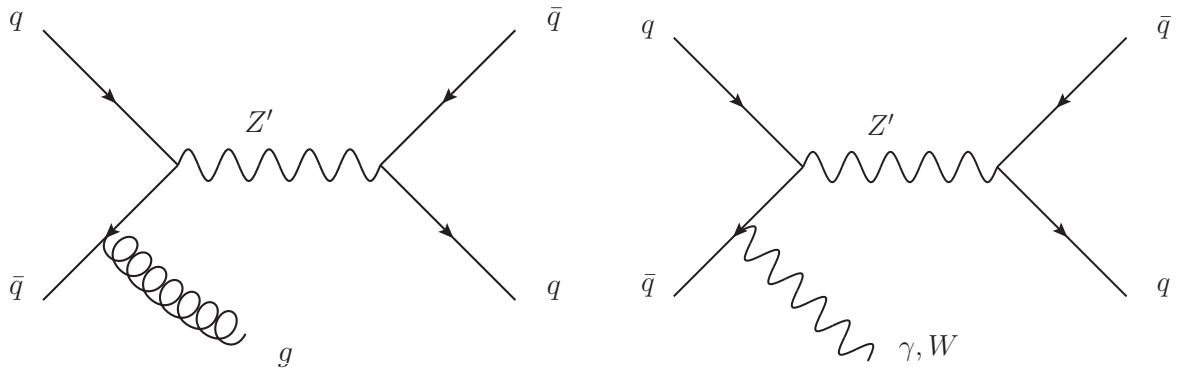

Figure 4.1: Diagrams of Z' production with recoil against ISR of either a gluon (left), a photon or W boson (right).

is the case when the Z' production is accompanied by the hard initial-state radiation (ISR) of a jet or photon, as shown in Figure 4.1. If this ISR object has a large enough p_{T}, it will satisfy the detector trigger, regardless of the mass of the Z'. Naturally, the cross section of the $Z' + \mathrm{ISR}$ process is much smaller than the exclusive Z' production; however, a larger cross section is unhelpful if the trigger efficiency is zero.

We will compare the cases of ISR from a photon, jet, and W boson where the W decays to $\mu\nu$. Each channel has different trigger thresholds which define the momentum scale of the recoiling Z' decay. When the $p_{\mathrm{T}}^{Z'}$ of the Z' is high relative to its mass $m_{Z'}$, the light decay quarks are collimated by relativistic boosting; the average angular separation of the quarks can be approximated by $\Delta R(qq) \approx 2m_{Z'}/p_{\mathrm{T}}^{Z'}$. In this case it is possible for the resulting jets from each quark to have significant overlap in the detector, which can make reconstruction of the dijet mass difficult.

To deal with this effect, we will compare two reconstruction strategies for each channel. In the first approach, referred to as the *resolved* mode, we examine events with one ISR object (jet, photon, or μ, depending on the channel) and two jets, each reconstructed by clustering with radius parameter $R = 0.4$. In the second approach, referred to as the *boosted* or *merged* mode, we examine events with one ISR object and one *large radius* jet, reconstructed with

radius parameter $R = 1.0$.

In the resolved mode, the quantity of interest will be the invariant mass m_{jj} of the two jets recoiling from the ISR trigger object. In the merged mode, we examine the mass m_J of the large-R jet. For signal events, we expect to see a peak localized about $m_{Z'}$ in these distributions. These mass spectra are then compared against expected backgrounds in order to estimate the potential sensitivity in the approximately 4 fb^{-1} of proton-proton collision data from the 2015 LHC run.

4.2 Monte Carlo Samples

Simulated event samples are used to model the kinematics of the signal and background processes produced in proton-proton collisions at $\sqrt{s} = 13$ TeV. Events with a hypothetical Z' boson are simulated at parton level with MADGRAPH5 [136], with PYTHIA [137] for showering and hadronization. In these studies, simulated signal events are generated with $g_B = 1.5$. The γ+jets background is generated using SHERPA [62], requiring 1–3 additional hard partons. The $W + jets$ background also comes from SHERPA, generating events with a final state containing $\nu + \mu$ and up to 2 additional partons; a parton-level requirement on the invariant mass $m_{\mu\nu} > 2$ GeV is imposed. The multi-jet background is also generated with SHERPA, requiring 2–4 hard partons in the final state.

All simulated events are rendered through the DELPHES [138] fast-simulation framework, configured to approximate ATLAS the detector response. The measurement of jet masses is sensitive to the presence of additional in-time pileup events. In order to emulate this effect, we overlay each event in DELPHES with random minimum-bias events, with an average number of interactions per event of $\langle\mu\rangle = 15$, which is comparable to the level observed in ATLAS 2015 data with the LHC delivering collisions at a 25ns bunch crossing interval.

The impact of pileup events on jet reconstruction can be mitigated using several techniques. For narrow-radius jets, we apply the area-based pileup subtraction technique [36]. For the reconstruction of large-radius jets, the jet-trimming algorithm [139] is applied, wherein the jet constituents are reclustered into $R = 0.2$ C/A subjets, and those subjects with less than 3% of the total jet p_{T} are removed. This method is designed to abate pileup contributions to the jet, while preserving the two-prong structure of jets from boosted decays.

4.3 Event Selections

4.3.1 $\gamma + Z'$ Channel

The photon channel benefits both from the availability of relatively low-p_{T} unprescaled trigger thresholds, as well as reduced combinatorial ambiguity in the topology of the final state compared to the jet channel.

For all events in the $\gamma + Z'$ channel, we require at least one isolated photon with $p_{\mathrm{T}}^{\gamma} > 120$ GeV, which reflects the lowest unprescaled single-photon trigger available to ATLAS in 2015 data. For signal masses of 300 GeV and above, we additionally require a leading photon with $p_{\mathrm{T}}^{\gamma} > 170$ GeV, as this provides a slight increase in sensitivity.

The key discriminating feature between the signal and background model is the presence of a resonant peak from the $Z' \to q\bar{q}$ decay in either the resolved dijet mass m_{jj} or the merged large-R jet mass m_J. To reconstruct m_{jj}, we require at least two jets with $p_{\mathrm{T}} > 20$ GeV, and select the pair of jets in the event which have the highest p_{T}^{jj}. For the merged mode, we require at least one large-R jet with $p_{\mathrm{T}}^{J} > 80$ GeV and a mass of at least 20 GeV. In the case of multiple large-R jets, the one with greatest p_{T}^{J} is selected.

Due to conservation of momentum, the p_{T} of the photon and the Z' candidate (either selected

the dijet or large-R object) should be balanced in the final state. However, due to finite detector resolution, soft radiation, and pileup contamination, the reconstructed balance is imperfect. Hence, we apply the loose requirement that $|p_{\mathrm{T}}^{Z'} - p_{\mathrm{T}}^{\gamma}|/p_{\mathrm{T}}^{\gamma} < 0.5$. This slightly improves sensitivity by rejecting background events where the jet(s) selected do not fully balance the photon, while also improving the signal shape by rejecting events where the wrong jets were selected for reconstruction.

The dominant background in this channel is due to SM prompt photon production, labeled γ+jet throughout. SHERPA has been shown [140] to accurately model events with photons and jets in various kinematic distributions. No k-factor is available in the literature, so in the results below we demonstrate the effect of a k-factor ranging from 1 to 2.

We also account for the SM $\gamma + W$ and $\gamma + Z$ production; simulated samples are generated at leading order in α with MADGRAPH; note that these processes are approximately three orders of magnitude below the γ+jet background, and approximately one order of magnitude below the predicted signal rate for the hypothesized Z' signal with $g_{\mathrm{B}} = 1.5$.

Figure 4.2 shows the distribution of reconstructed large-R or dijet masses in both signal and background processes for the $\gamma + Z'$ channel.

4.3.2 $W(\mu\nu) + Z'$ Channel

As with the photon channel, the leptonic W channel has little ambiguity in selecting the correct final state jets, and benefits from the even lower-p_{T} lepton trigger thresholds which potentially enhances resolution of very light resonances by limiting the collimation and overlap of the decay produces from the less-boosted object. This comes at the cost of lower branching fractions of both the vector boson ISR and its leptonic decay mode, which greatly reduces the signal production cross section. For simplicity, we consider only the muon final

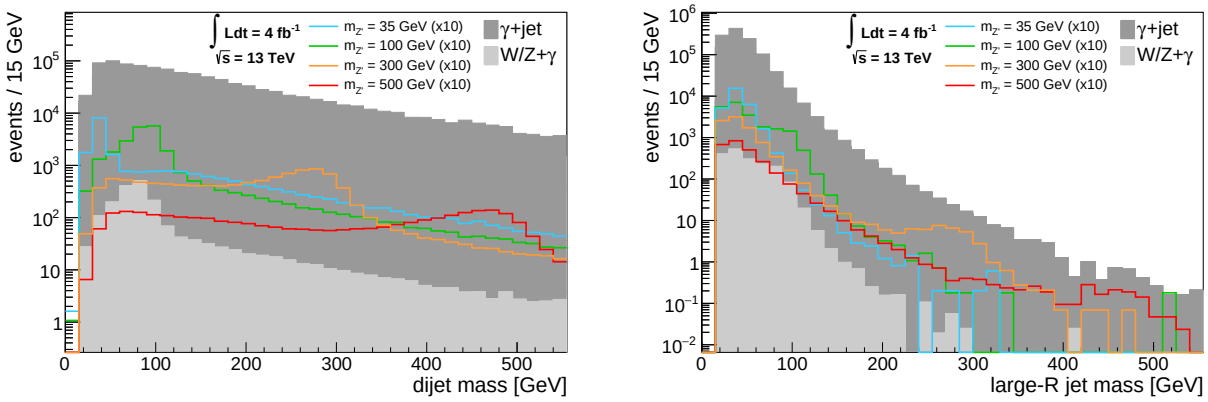

(a) (b)

Figure 4.2: Distributions for $\sqrt{s} = 13$ TeV and $\int \mathcal{L}dt = 4$ fb^{-1} of reconstructed Z' candidate masses in the $\gamma + Z'$ channel. The resolved mode is shown on the left, merged on the right. Also shown are signal distributions, generated with $g_{\mathrm{B}} = 1.5$ and scaled by a factor of 10 for visibility.

state; adding electrons increases the complexity of the analysis and at best results in a factor of $\sim \sqrt{2}$ in cross section sensitivity, translating to only approximately 9% improvement in g_{B} reach.

For all events in the $W(\mu\nu) + Z'$ channel, we require exactly one isolated muon with $p_{\mathrm{T}} > 40$ GeV, representing the muon trigger. Events containing additional electrons or muons with $p_{\mathrm{T}} > 10$ GeV are vetoed.

To select the Z' candidate, the same procedure as in Section 4.3.1 is followed. However, since the observed μ alone is not expected to balance the p_{T} of the resonance, no momentum conservation cut is applied.

In contrast to the $\gamma + Z'$ channel, backgrounds to the $W + Z'$ channel are not wholly determined by a single process. The largest source of background is due to standard model W boson production with additional ISR jets. We also account for backgrounds due to SM top single- and pair-production, Z+jets with leptonic decays, and semileptonic diboson processes; each of these is generated with MADGRAPH5. The Z+jets background is somewhat reduced by the additional lepton veto; however, due to the relatively low-p_{T} muon threshold

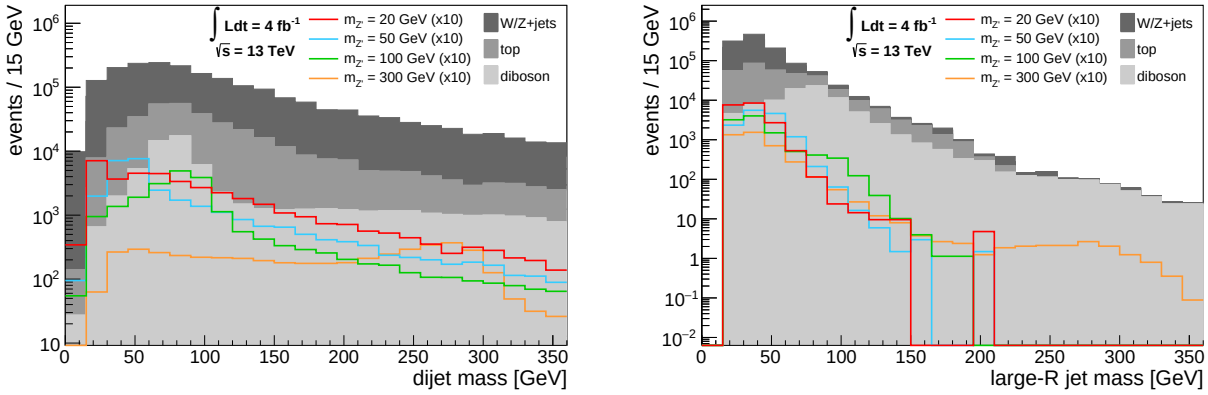

(a) (b)

Figure 4.3: Distributions for $\sqrt{s} = 13$ TeV and $\int \mathcal{L}dt = 4$ fb^{-1} of reconstructed Z' candidate masses in the $W(\mu\nu) + Z'$ channel. The resolved mode is shown on the left, merged on the right. Also shown are signal distributions, generated with $g_{\mathrm{B}} = 1.5$ and scaled by a factor of 10 for visibility.

many events contain soft additional leptons which are not reconstructed, and thus pass the selection. The sole background to show resonant structure in the reconstructed jet mass is the diboson WZ production with semileptonic decay. Figure 4.3 show the distribution of reconstructed large-R or dijet masses in both signal and background processes for the $W+Z'$ channel.

4.3.3 jet+Z' Channel

The jet+Z' channel contains only jets in the final state, leading to greater ambiguity in identifying the reconstructed Z' mass. Here we will refer to either the single large-R jet or the pair of resolved jets which are supposed to originate from the hypothetical Z' decay as the reconstructed *decay jet(s)*. We refer to the small-R jet which is opposite in momentum to the decay jet(s) as the *probe jet*. It is impossible to always assign the decay jets correctly, particularly in the presence of additional QCD radiation and pileup. While the simple heuristic approaches described below work reasonably well, further studies may benefit considerably from the use of multivariate techniques in order to select the most signal-like jet(s) from

each event.

For all events in the jet+Z' channel, we require at least one narrow-radius jet satisfying $|\eta| < 3.2$ and $p_{\mathrm{T}} > 360$ GeV; these criteria reflect the lowest-p_{T} unprescaled single-jet triggers available to ATLAS in 2015 data in the central detector. In the merged case, we avoid the possibility of selecting a probe jet overlapping with a candidate decay jet. First we examine all pairs of reconstructed $R = 0.4$ and $R = 1.0$ jets, and consider only those pairs which are separated by $\Delta R > 0.8$. We select the pair with the highest large-R jet p_{T}. In cases where this is not unique, we then choose the pair with highest small-R jet p_{T}. The small-R jet is assigned as the probe jet, and the large-R is taken as the decay jet of the Z' candidate.

For the resolved case, the Z' candidate is build from the pair of small-R jets whose combined four-momentum has the largest p_{T}. Of the remaining unassigned jets, the small-R jet with largest p_{T} is assigned as the probe jet.

As before, in order to enforce momentum balance of the underlying event, we require that the Z' candidate satisfy $|p_{\mathrm{T}}^{Z'} - p_{\mathrm{T}}^{\mathrm{probe}}|/p_{\mathrm{T}}^{\mathrm{probe}} < 0.5$.

The overwhelming background in this channel is standard model QCD multi-jet production. It is the large rate of this background that requires ATLAS and CMS to operate with single-jet p_{T} thresholds of 360 and 450 GeV, respectively.

We also account for standard model W and Z boson production, in association with one hard parton, generated with MADGRAPH. However, as in the $\gamma + Z'$ channel, the contributions are very small relative to the QCD backgrounds. Figure 4.4 shows the distribution of reconstructed Z' candidate masses in both the resolved and merged modes for signal and background processes in the jet+Z' channel.

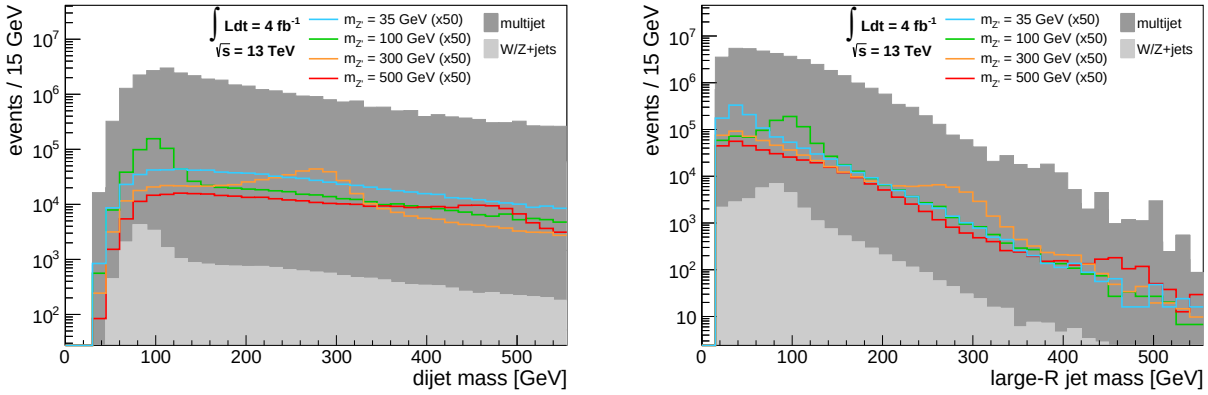

(a) (b)

Figure 4.4: Distributions for $\sqrt{s} = 13$ TeV and $\int \mathcal{L}dt = 4$ fb^{-1} of reconstructed Z' candidate masses in the jet+Z' channel. The resolved mode is shown on the left, merged on the right. Also shown are signal distributions, generated with $g_{\mathrm{B}} = 1.5$ and scaled by a factor of 50 for visibility.

4.4 Expected Sensitivity

Estimates of the signal and background yields for pp collisions at $\sqrt{s} = 13$ TeV and 4 fb^{-1} of integrated luminosity are used to calculate upper limits on the production cross section of the hypothetical Z' process that could be reasonably expected with the existing LHC dataset. Limits on the cross section are then converted into upper limits on the gauge coupling strength g_{B} using the cross section scaling relation of $\sigma \propto g_{\mathrm{B}}^4$.

Limits are calculated at 95% CL using a profile likelihood ratio [67] and the CLs technique [111, 112]. Binned histograms of the signal and background distributions of the candidate Z' mass formed from the dijet mass m_{jj} in the resolved mode and the large-R jet mass m_J in the merged mode are compared. The normalization of the signal histogram is treated as free parameter, and tested for compatibility against the background-only hypothesis by drawing pseudodata from the input distribution, taking into account the expected systematic and statistical uncertainties in the luminosity-scaled number of events. In the $\gamma + Z'$ and $W + Z'$ channels, the large-R jet mass distribution is binned from $24 - 550$ GeV, with bin widths increasing from 8–50 GeV; the dijet mass distribution is binned with bin widths

of 10 GeV between 10–520 GeV. In the jet+Z' channel, the large-R jet mass distribution is binned from 8–50 GeV, and the dijet mass is binned every 10 GeV from 80–550 GeV. Hypothetical signal masses are considered only if the reconstructed mass distribution displays a localized peak, allowing for the normalization of the background and profiling of nuisance parameters in the sidebands. Because the resolved dijet mode requires a degree of angular separation between the decay products in order for the independent jets to be successfully reconstructed, there is a minimal mass that can be successfully reconstructed in this mode for a given p_{T} scale, set by the trigger threshold. This effect can be observed in Figure 4.4a.

The detector modeling provided by DELPHES is relatively crude, particularly in modeling the precise substructure of large-R jets required for accurate mass reconstruction, and we attempt only to estimate the sensitivity of such measurements in order to assess the feasibility of carrying out the more sophisticated studies required for an accurate experimental measurement. To this end, it is not critical that the exact background rates or detector response are attained. Nonetheless, we consider some simple sources of systematic uncertainties in order to make the limit-setting process more realistic, as without any uncertainties the confidence levels would be overestimated.

The dominant γ+jet and multi-jet backgrounds are assigned a 15% uncertainty on their overall normalization. The smaller $W/Z + X$ backgrounds are assigned 5% normalization uncertainties. Accurate estimates of these uncertainties would come from studies of the scale dependence of the k-factor in collision data. As this information is not currently available in the literature, we assess these uncertainties as they are typical of QCD and EW backgrounds, respectively. We note that due to the use of the profile likelihood fitting technique, the nuisance parameters associated with these uncertainties should be well constrained in data from the background-dominated bins in the sidebands of the signal mass region. We also consider uncertainties in the expected Z' reconstructed mass distribution. A significant source of uncertainty in the reconstructed mass distribution will come from the (di)jet mass

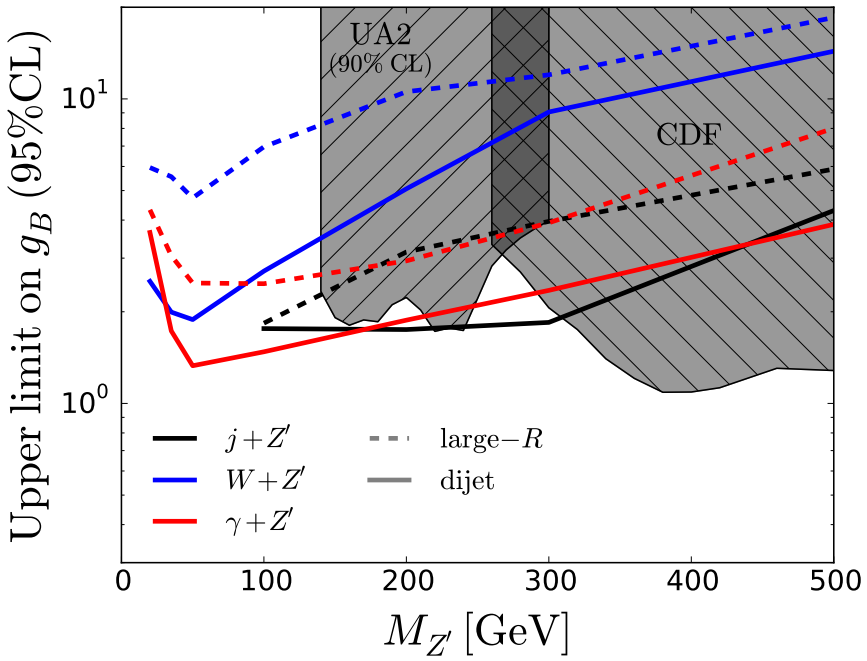

Figure 4.5: Expected upper limits at 95% CL on the coupling g_{B} between the hypothetical Z' boson and quarks for values of $m_{Z'}$ ranging from 20–500GeV. For each of the $\gamma + Z'$, $W + Z'$, and jet+Z' channels, results derived from the dijet mass (resolved mode, solid lines) and large-R mass (merged mode, dashed lines) distributions are shown. Limits are calculated assuming pp collisions at $\sqrt{s} = 13$ TeV with $\int \mathcal{L}dt = 4$ fb^{-1}. For comparison, we include existing limits from the UA2 and CDF experiments (shaded contours), as interpreted by Ref. [124].

resolution, caused by uncertainties in the hadronic response calibration. Detailed studies from the experimental collaborations themselves will be required for definitive assessment of these systematics. As a crude estimate of the energy scale uncertainties, we shift the response of all DELPHES calorimeter towers by ±5%.

The expected 95% CL limits are shown in Table 4.1 and Figure 4.5. If the k-factors for the largest backgrounds are doubled, the limits shown in these figures are weakened by approximately 17–21%. We note that while the resolved dijet technique tends to perform considerably better in this study than the merged mode at all but the very lowest masses, we expect the application of further jet substructure techniques in large-R boson tagging may prove to enhance the sensitivity of the merged method. As we shall see in Section 4.5, this has recently been shown to indeed be the case.

		$m_{Z'}$ [GeV]						
Channel	mode	20	35	50	100	200	300	500
$\gamma + Z'$	resolved	3.6	1.7	1.3	1.5	1.9	2.4	3.9
	merged	4.3	3.1	2.5	2.5	2.9	3.9	8.0
$W + Z'$	resolved	2.5	2.0	1.9	2.7	5.1	9.1	14.3
	merged	6.0	5.6	4.7	7.0	10.6	12.0	18.5
jet+Z'	resolved	–	–	–	1.8	3.1	4.0	5.9
	merged	–	–	–	1.8	1.7	1.8	4.3

Table 4.1: Expected upper limits at 95% CL on the coupling g_{B} between the hypothetical Z' boson and quarks for values of $m_{Z'}$ ranging from 20–500GeV. For each of the $\gamma + Z'$, $W + Z'$, and jet+Z' channels, results derived from the dijet mass (resolved mode) and large-R mass (merged mode) distributions are shown. Limits are calculated assuming pp collisions at $\sqrt{s} = 13$ TeV with $\int \mathcal{L}dt = 4$ fb^{-1}.

4.5 Conclusion

We have presented a method for performing searches for hadronic resonances with masses in the range 20–500 GeVat the LHC. Previously, much of this region was unprobed by direct measurements of two-jet signals due to the systematic limitations of hadronic triggers in experiments at the LHC and at previous colliders.

As a benchmark model, we consider the case of a hypothetical Z' which decays to $q\bar{q}$ in order to quantify the possible experimental sensitivity of this method in terms of exclusion reach in the coupling g_{B} between the Z' and the quarks. Expected limits on g_{B} are estimated assuming $\int \mathcal{L}dt = 4\mathrm{fb}^{-1}$ of pp collisions at $sqrts = 13$ TeV, corresponding to data already available from the 2015 run of the LHC. The limits in the mass range of approximately 160–350 GeV are conservatively found to be of comparable sensitivity to measurements conducted at much lower energies at the Tevatron and Sp$\bar{\mathrm{p}}$S colliders. Limits in the range 20–150 GeV would constitute the first direct searches for hadronic resonances at these masses.

In the time since this work was published, preliminary results from the CMS and ATLAS collaborations implementing the proposed search have begun to emerge [141, 142]. Although no excesses are observed, the resulting limits are quite consistent with the expectations

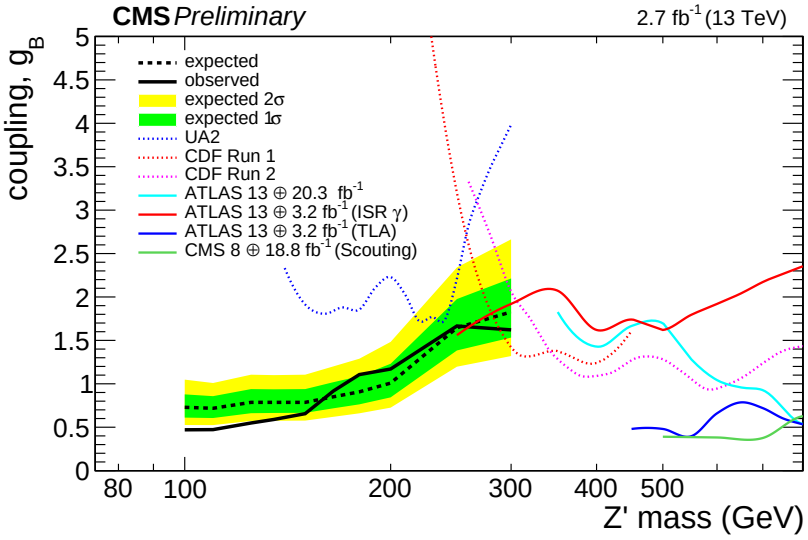

Figure 4.6: Figure from Ref. [142] showing recent limits from both CMS and ATLAS obtained from the 2015 pp collision data. The solid red line indicates limits from ATLAS in the $\gamma + Z'$ channel using the resolved reconstruction mode. The solid black line indicates limits from CMS in the jet+Z' channel using the merged reconstruction mode with large-R jets clustered with radius parameter $R = 0.8$.

derived in Section 4.4. We note however that the CMS result, which employs recently developed substructure-based jet tagging techniques [143], outperforms our expectations at low masses. Future results from both collaborations are anticipated to refine the limits and extend the reach to lower $m_{Z'}$ as more data becomes available and jet substructure techniques are developed.

Bibliography

[1] Gianfranco Bertone, Dan Hooper, and Joseph Silk. Particle dark matter: Evidence, candidates and constraints. *Phys. Rept.*, 405:279–390, 2005.

[2] P. A. R. Ade et al. Planck 2015 results. XIII. Cosmological parameters. *Astron. Astrophys.*, 594:A13, 2016.

[3] Robert J. Scherrer and Michael S. Turner. On the relic, cosmic abundance of stable, weakly interacting massive particles. *Phys. Rev. D*, 33:1585–1589, Mar 1986.

[4] Lyndon Evans and Philip Bryant. LHC Machine. *JINST*, 3:S08001, 2008.

[5] ATLAS Collaboration. The ATLAS Experiment at the CERN Large Hadron Collider. *JINST*, 3:S08003, 2008.

[6] ATLAS Collaboration. Observation of a new particle in the search for the Standard Model Higgs boson with the ATLAS detector at the LHC. *Phys. Lett. B*, 716:1, 2012.

[7] ATLAS Collaboration. A Particle Consistent with the Higgs Boson Observed with the ATLAS Detector at the Large Hadron Collider. *Science*, 338:1576, 2012.

[8] CMS Collaboration. Observation of a new boson at a mass of 125 GeV with the CMS experiment at the LHC. *Phys. Lett. B*, 716:30, 2012.

[9] Ringaile Placakyte. Parton Distribution Functions. In *Proceedings, 31st International Conference on Physics in collisions (PIC 2011): Vancouver, Canada, August 28-September 1, 2011*, 2011.

[10] ATLAS Collaboration. *ATLAS magnet system: Technical Design Report, 1.* Technical Design Report ATLAS. CERN, Geneva, 1997.

[11] ATLAS Collaboration. *ATLAS inner detector: Technical Design Report, 1.* Technical Design Report ATLAS. CERN, Geneva, 1997.

[12] ATLAS Collaboration. Early Inner Detector Tracking Performance in the 2015 data at $\sqrt{s} = 13$ TeV. Technical Report ATL-PHYS-PUB-2015-051, CERN, Geneva, Dec 2015.

[13] ATLAS Collaboration. ATLAS Insertable B-Layer Technical Design Report. Technical Report CERN-LHCC-2010-013. ATLAS-TDR-19, CERN, Sep 2010.

[14] ATLAS Collaboration. Performance of the ATLAS Trigger System in 2010. *Eur. Phys. J. C*, 72:1849, 2012.

[15] ATLAS Collaboration. *ATLAS level-1 trigger: Technical Design Report.* Technical Design Report ATLAS. CERN, Geneva, 1998.

[16] R Blair, J Dawson, G Drake, W Haberichter, J Schlereth, J Zhang, M Abolins, Y Ermoline, and B Pope. The atlas high level trigger region of interest builder. *Journal of Instrumentation*, 3(04):P04001, 2008.

[17] ATLAS Collaboration. 2015 start-up trigger menu and initial performance assessment of the ATLAS trigger using Run-2 data. ATL-DAQ-PUB-2016-001, 2016.

[18] ATLAS Collaboration. Expected electron performance in the ATLAS experiment. ATL-PHYS-PUB-2011-006, 2011.

[19] ATLAS Collaboration. Expected photon performance in the ATLAS experiment. ATL-PHYS-PUB-2011-007, 2011.

[20] Walter Lampl et al. Calorimeter Clustering Algorithms: Description and Performance. ATL-LARG-PUB-2008-002, 2008.

[21] ATLAS Collaboration. Electron reconstruction and identification efficiency measurements with the ATLAS detector using the 2011 LHC proton–proton collision data. *Eur. Phys. J. C*, 74:2941, 2014.

[22] ATLAS Collaboration. Measurement of the muon reconstruction performance of the ATLAS detector using 2011 and 2012 LHC proton–proton collision data. *Eur. Phys. J. C*, 74:3130, 2014.

[23] ATLAS Collaboration. Muon reconstruction performance of the ATLAS detector in proton–proton collision data at $\sqrt{s} = 13$ TeV. *Eur. Phys. J. C*, 76:292, 2016.

[24] Ryan Atkin. Review of jet reconstruction algorithms. *J. Phys. Conf. Ser.*, 645(1):012008, 2015.

[25] S. Catani, Yuri L. Dokshitzer, M. H. Seymour, and B. R. Webber. Longitudinally invariant K_t clustering algorithms for hadron hadron collisions. *Nucl. Phys.*, B406:187–224, 1993.

[26] Yuri L. Dokshitzer, G. D. Leder, S. Moretti, and B. R. Webber. Better jet clustering algorithms. *JHEP*, 08:001, 1997.

[27] Matteo Cacciari, Gavin P. Salam, and Gregory Soyez. The Anti-k(t) jet clustering algorithm. *JHEP*, 04:063, 2008.

[28] Stephen D. Ellis, Andrew Hornig, Tuhin S. Roy, David Krohn, and Matthew D. Schwartz. Qjets: A Non-Deterministic Approach to Tree-Based Jet Substructure. *Phys. Rev. Lett.*, 108:182003, 2012.

[29] ATLAS Collaboration. Properties of jets and inputs to jet reconstruction and calibration with the ATLAS detector using proton–proton collisions at $\sqrt{s} = 13$ TeV. ATL-PHYS-PUB-2015-036, 2015.

[30] ATLAS Collaboration. Properties of Jets and Inputs to Jet Reconstruction and Calibration with the ATLAS Detector Using Proton–Proton Collisions at $\sqrt{s} = 7$ TeV. ATLAS-CONF-2010-053, 2010.

[31] ATLAS Collaboration. Properties and internal structure of jets produced in proton–proton collisions at $\sqrt{s} = 900$ GeV. ATLAS-CONF-2010-018, 2010.

[32] ATLAS Collaboration. Jet energy measurement with the ATLAS detector in proton–proton collisions at $\sqrt{s} = 7$ TeV. *Eur. Phys. J. C*, 73:2304, 2013.

[33] ATLAS Collaboration. Jet energy scale and its systematic uncertainty in proton–proton collisions at $\sqrt{s} = 7$ TeV with ATLAS 2011 data. ATLAS-CONF-2013-004, 2013.

[34] ATLAS Collaboration. Jet Calibration and Systematic Uncertainties for Jets Reconstructed in the ATLAS Detector at $\sqrt{s} = 13$ TeV. ATL-PHYS-PUB-2015-015, 2015.

[35] ATLAS Collaboration. Pile-up subtraction and suppression for jets in ATLAS. ATLAS-CONF-2013-083, 2013.

[36] Matteo Cacciari and Gavin P. Salam. Pileup subtraction using jet areas. *Phys. Lett.*, B659:119–126, 2008.

[37] ATLAS Collaboration. Performance of algorithms that reconstruct missing transverse momentum in $\sqrt{s} = 8$ TeV proton-proton collisions in the ATLAS detector. 2016.

[38] ATLAS Collaboration. Performance of missing transverse momentum reconstruction in proton–proton collisions at $\sqrt{s} = 7$ TeV with ATLAS. *Eur. Phys. J. C*, 72:1844, 2012.

[39] CDF Collaboration. Search for dark matter in events with one jet and missing transverse energy in $p\overline{p}$ collisions at $\sqrt{s}$=1.96 TeV. *Phys. Rev. Lett.*, 108:211804, May 2012.

[40] ATLAS Collaboration. Search for dark matter candidates and large extra dimensions in events with a jet and missing transverse momentum with the ATLAS detector. *JHEP*, 04:075, 2013.

[41] ATLAS Collaboration. Search for dark matter candidates and large extra dimensions in events with a photon and missing transverse momentum in pp collision data at $\sqrt{s} = 7$ TeV with the ATLAS detector. *Phys. Rev. Lett.*, 110:011802, 2013.

[42] CMS Collaboration. Search for dark matter and large extra dimensions in monojet events in pp collisions at $\sqrt{s} = 7$ TeV. *JHEP*, 09:094, 2012.

[43] CMS Collaboration. Search for Dark Matter and Large Extra Dimensions in pp Collisions Yielding a Photon and Missing Transverse Energy. *Phys. Rev. Lett.*, 108:261803, 2012.

[44] CMS Collaboration. Search for dark matter, extra dimensions, and unparticles in monojet events in proton–proton collisions at $\sqrt{s} = 8$ TeV. *Eur. Phys. J. C*, 75:235, 2015.

[45] Andreas Birkedal, Konstantin Matchev, and Maxim Perelstein. Dark matter at colliders: A Model independent approach. *Phys. Rev.*, D70:077701, 2004.

[46] V. M. Abazov et al. Search for Large Extra Dimensions in the Monojet + $\not{E}_{\mathrm{T}}$ Channel with the D$\emptyset$ Detector. *Phys. Rev. Lett.*, 90:251802, Jun 2003.

[47] D. Acosta et al. Search for Kaluza-Klein graviton emission in $p\bar{p}$ collisions at $\sqrt{s} =$ 1.8-TeV using the missing energy signature. *Phys. Rev. Lett.*, 92:121802, 2004.

[48] S. Abachi et al. The D$\emptyset$ detector. *Nuclear Instruments and Methods in Physics Research Section A: Accelerators, Spectrometers, Detectors and Associated Equipment*, 338(2):185 – 253, 1994.

[49] F. Abe et al. The CDF Detector: An Overview. *Nucl. Instrum. Meth.*, A271:387–403, 1988.

[50] ATLAS Collaboration. Search for new phenomena in events with a photon and missing transverse momentum in pp collisions at $\sqrt{s} = 13$ TeV with the ATLAS detector. *JHEP*, 06:059, 2016.

[51] ATLAS Collaboration. Search for new phenomena in final states with an energetic jet and large missing transverse momentum in pp collisions at $\sqrt{s} = 13$ TeV using the ATLAS detector. *Phys. Rev. D*, 94:032005, 2016.

[52] Linda M. Carpenter, Andrew Nelson, Chase Shimmin, Tim M. P. Tait, and Daniel Whiteson. Collider searches for dark matter in events with a Z boson and missing energy. *Phys. Rev.*, D87(7):074005, 2013.

[53] ATLAS Collaboration. Measurement of ZZ production in pp collisions at $\sqrt{s} = 7$ TeV and limits on anomalous ZZZ and $ZZ\gamma$ couplings with the ATLAS detector. *JHEP*, 03:128, 2013.

[54] ATLAS Collaboration. Search for dark matter in events with a Z boson and missing transverse momentum in pp collisions at $\sqrt{s} = 8$ TeV with the ATLAS detector. *Phys. Rev. D*, 90:012004, 2014.

[55] ATLAS Collaboration. Search for dark matter in events with a hadronically decaying W or Z boson and missing transverse momentum in pp collisions at $\sqrt{s} = 8$ TeV with the ATLAS detector. *Phys. Rev. Lett.*, 112:041802, 2014.

[56] Jessica Goodman, Masahiro Ibe, Arvind Rajaraman, William Shepherd, Tim M. P. Tait, and Hai-Bo Yu. Constraints on Dark Matter from Colliders. *Phys. Rev.*, D82:116010, 2010.

[57] Nicole F. Bell, James B. Dent, Ahmad J. Galea, Thomas D. Jacques, Lawrence M. Krauss, and Thomas J. Weiler. Searching for Dark Matter at the LHC with a Mono-Z. *Phys. Rev.*, D86:096011, 2012.

[58] Johan Alwall, Michel Herquet, Fabio Maltoni, Olivier Mattelaer, and Tim Stelzer. MadGraph 5 : Going Beyond. *JHEP*, 06:128, 2011.

[59] Tom Melia, Paolo Nason, Raoul Rontsch, and Giulia Zanderighi. W+W-, WZ and ZZ production in the POWHEG BOX. *JHEP*, 11:078, 2011.

[60] Torbjorn Sjostrand, Stephen Mrenna, and Peter Z. Skands. A Brief Introduction to PYTHIA 8.1. *Comput. Phys. Commun.*, 178:852–867, 2008.

[61] ATLAS Collaboration. Summary of ATLAS Pythia 8 tunes. ATL-PHYS-PUB-2012-003, 2012.

[62] T. Gleisberg, Stefan. Hoeche, F. Krauss, M. Schonherr, S. Schumann, F. Siegert, and J. Winter. Event generation with SHERPA 1.1. *JHEP*, 02:007, 2009.

[63] S. Agostinelli et al. GEANT4: A Simulation toolkit. *Nucl. Instrum. Meth.*, A506:250–303, 2003.

[64] ATLAS Collaboration. The ATLAS Simulation Infrastructure. *Eur. Phys. J. C*, 70:823, 2010.

[65] ATLAS Collaboration. Tagging and suppression of pileup jets with the ATLAS detector. ATLAS-CONF-2014-018, 2014.

[66] Michelangelo L. Mangano, Mauro Moretti, Fulvio Piccinini, Roberto Pittau, and Antonio D. Polosa. ALPGEN, a generator for hard multiparton processes in hadronic collisions. *JHEP*, 07:001, 2003.

[67] Glen Cowan, Kyle Cranmer, Eilam Gross, and Ofer Vitells. Asymptotic formulae for likelihood-based tests of new physics. *Eur. Phys. J.*, C71:1554, 2011. [Erratum: Eur. Phys. J.C73,2501(2013)].

[68] E. Behnke et al. First Dark Matter Search Results from a 4-kg CF_3I Bubble Chamber Operated in a Deep Underground Site. *Phys. Rev.*, D86(5):052001, 2012. [Erratum: Phys. Rev.D90,no.7,079902(2014)].

[69] M. Felizardo et al. Final Analysis and Results of the Phase II SIMPLE Dark Matter Search. *Phys. Rev. Lett.*, 108:201302, 2012.

[70] S. Archambault et al. Constraints on Low-Mass WIMP Interactions on ^{19}F from PICASSO. *Phys. Lett.*, B711:153–161, 2012.

[71] M. G. Aartsen et al. Search for dark matter annihilations in the Sun with the 79-string IceCube detector. *Phys. Rev. Lett.*, 110(13):131302, 2013.

[72] C. E. Aalseth et al. Results from a Search for Light-Mass Dark Matter with a P-type Point Contact Germanium Detector. *Phys. Rev. Lett.*, 106:131301, 2011.

[73] E. Aprile et al. Dark Matter Results from 225 Live Days of XENON100 Data. *Phys. Rev. Lett.*, 109:181301, 2012.

[74] R. Agnese et al. Search for Low-Mass Weakly Interacting Massive Particles Using Voltage-Assisted Calorimetric Ionization Detection in the SuperCDMS Experiment. *Phys. Rev. Lett.*, 112(4):041302, 2014.

[75] R. Agnese et al. Search for Low-Mass Weakly Interacting Massive Particles with SuperCDMS. *Phys. Rev. Lett.*, 112(24):241302, 2014.

[76] D. S. Akerib et al. First results from the LUX dark matter experiment at the Sanford Underground Research Facility. *Phys. Rev. Lett.*, 112:091303, 2014.

[77] Gary Steigman, Basudeb Dasgupta, and John F. Beacom. Precise Relic WIMP Abundance and its Impact on Searches for Dark Matter Annihilation. *Phys. Rev.*, D86:023506, 2012.

[78] Linda Carpenter, Anthony DiFranzo, Michael Mulhearn, Chase Shimmin, Sean Tulin, and Daniel Whiteson. Mono-Higgs-boson: A new collider probe of dark matter. *Phys. Rev.*, D89(7):075017, 2014.

[79] Gerard Jungman, Marc Kamionkowski, and Kim Griest. Supersymmetric dark matter. *Phys. Rept.*, 267:195–373, 1996.

[80] ATLAS Collaboration. Search for Dark Matter in Events with Missing Transverse Momentum and a Higgs Boson Decaying to Two Photons in pp Collisions at $\sqrt{s} =$ 8 TeV with the ATLAS Detector. *Phys. Rev. Lett.*, 115:131801, 2015.

[81] John McDonald. Gauge singlet scalars as cold dark matter. *Phys. Rev.*, D50:3637–3649, 1994.

[82] C. P. Burgess, Maxim Pospelov, and Tonnis ter Veldhuis. The Minimal model of nonbaryonic dark matter: A Singlet scalar. *Nucl. Phys.*, B619:709–728, 2001.

[83] Brian Patt and Frank Wilczek. Higgs-field portal into hidden sectors. 2006.

[84] Yeong Gyun Kim and Kang Young Lee. Minimal model of fermionic dark matter. *Phys. Rev. D*, 75:115012, Jun 2007.

[85] John March-Russell, Stephen M. West, Daniel Cumberbatch, and Dan Hooper. Heavy Dark Matter Through the Higgs Portal. *JHEP*, 07:058, 2008.

[86] Ian Low, Pedro Schwaller, Gabe Shaughnessy, and Carlos E. M. Wagner. The dark side of the Higgs boson. *Phys. Rev.*, D85:015009, 2012.

[87] Laura Lopez-Honorez, Thomas Schwetz, and Jure Zupan. Higgs portal, fermionic dark matter, and a Standard Model like Higgs at 125 GeV. *Phys. Lett.*, B716:179–185, 2012.

[88] G. Belanger, B. Dumont, U. Ellwanger, J. F. Gunion, and S. Kraml. Status of invisible Higgs decays. *Phys. Lett.*, B723:340–347, 2013.

[89] J. Beringer et al. Review of Particle Physics (RPP). *Phys. Rev.*, D86:010001, 2012.

[90] Paul Langacker. The Physics of Heavy Z' Gauge Bosons. *Rev. Mod. Phys.*, 81:1199–1228, 2009.

[91] Christopher D. Carone and Hitoshi Murayama. Possible light U(1) gauge boson coupled to baryon number. *Phys. Rev. Lett.*, 74:3122–3125, 1995.

[92] Kaustubh Agashe and Geraldine Servant. Warped unification, proton stability and dark matter. *Phys. Rev. Lett.*, 93:231805, 2004.

[93] Pavel Fileviez Perez and Mark B. Wise. Baryon and lepton number as local gauge symmetries. *Phys. Rev.*, D82:011901, 2010. [Erratum: Phys. Rev.D82,079901(2010)].

[94] Adam Falkowski, Francesco Riva, and Alfredo Urbano. Higgs at last. *JHEP*, 11:111, 2013.

[95] Abdelhak Djouadi and Grégory Moreau. The couplings of the Higgs boson and its CP properties from fits of the signal strengths and their ratios at the 7+8 TeV LHC. *Eur. Phys. J.*, C73(9):2512, 2013.

[96] Pier Paolo Giardino, Kristjan Kannike, Isabella Masina, Martti Raidal, and Alessandro Strumia. The universal Higgs fit. *JHEP*, 05:046, 2014.

[97] John Ellis and Tevong You. Updated Global Analysis of Higgs Couplings. *JHEP*, 06:103, 2013.

[98] Tao Han and S. Willenbrock. QCD correction to the p p —¿ W H and Z H total cross-sections. *Phys. Lett.*, B273:167–172, 1991.

[99] Oliver Brein, Abdelhak Djouadi, and Robert Harlander. NNLO QCD corrections to the Higgs-strahlung processes at hadron colliders. *Phys. Lett.*, B579:149–156, 2004.

[100] M. L. Ciccolini, S. Dittmaier, and M. Kramer. Electroweak radiative corrections to associated WH and ZH production at hadron colliders. *Phys. Rev.*, D68:073003, 2003.

[101] ATLAS Collaboration. Observation and study of the Higgs boson candidate in the two photon decay channel with the ATLAS detector at the LHC. ATLAS-CONF-2012-168, 2012.

[102] A. D. Martin, W. J. Stirling, R. S. Thorne, and G. Watt. Parton distributions for the LHC. *Eur. Phys. J.*, C63:189–285, 2009.

[103] Hung-Liang Lai, Marco Guzzi, Joey Huston, Zhao Li, Pavel M. Nadolsky, Jon Pumplin, and C. P. Yuan. New parton distributions for collider physics. *Phys. Rev.*, D82:074024, 2010.

[104] Richard D. Ball, Valerio Bertone, Francesco Cerutti, Luigi Del Debbio, Stefano Forte, Alberto Guffanti, Jose I. Latorre, Juan Rojo, and Maria Ubiali. Impact of Heavy Quark Masses on Parton Distributions and LHC Phenomenology. *Nucl. Phys.*, B849:296–363, 2011.

[105] Michiel Botje et al. The PDF4LHC Working Group Interim Recommendations. 2011.

[106] A. Djouadi, J. Kalinowski, and M. Spira. HDECAY: A Program for Higgs boson decays in the standard model and its supersymmetric extension. *Comput. Phys. Commun.*, 108:56–74, 1998.

[107] Stefano Actis, Giampiero Passarino, Christian Sturm, and Sandro Uccirati. NNLO Computational Techniques: The Cases H —¿ gamma gamma and H —¿ g g. *Nucl. Phys.*, B811:182–273, 2009.

[108] S. Dittmaier et al. Handbook of LHC Higgs Cross Sections: 1. Inclusive Observables. 2011.

[109] S. Dittmaier et al. Handbook of LHC Higgs Cross Sections: 2. Differential Distributions. 2012.

[110] M. Oreglia. *A Study of the Reactions* $\psi' \to \gamma\gamma\psi$. PhD thesis, SLAC, 1980.

[111] Alexander L. Read. Presentation of search results: The CL(s) technique. *J. Phys.*, G28:2693–2704, 2002. [,11(2002)].

[112] Thomas Junk. Confidence level computation for combining searches with small statistics. *Nucl. Instrum. Meth.*, A434:435–443, 1999.

[113] ATLAS Collaboration. Search for new phenomena in dijet events collected in 2015 and 2016 *pp* collisions with the ATLAS detector at $\sqrt{s} = 8$ TeV. ATLAS-CONF-2016-069, 2016.

[114] CMS Collaboration. Search for narrow resonances decaying to dijets in proton–proton collisions at $\sqrt{s} = 13$ TeV. *Phys. Rev. Lett.*, 116:071801, 2016.

[115] ATLAS Collaboration. Search for new phenomena in the dijet mass distribution using *pp* collision data at $\sqrt{s} = 8$ TeV with the ATLAS detector. *Phys. Rev. D*, 91:052007, 2015.

[116] CMS Collaboration. Search for Resonances in the Dijet Mass Spectrum from 7 TeV *pp* Collisions at CMS. *Phys. Lett. B*, 704:123, 2011.

[117] C. Albajar et al. Two Jet Mass Distributions at the CERN Proton - Anti-Proton Collider. *Phys. Lett.*, B209:127–134, 1988.

[118] T. Aaltonen et al. Search for new particles decaying into dijets in proton-antiproton collisions at s**(1/2) = 1.96-TeV. *Phys. Rev.*, D79:112002, 2009.

[119] E. Eichten, I. Hinchliffe, Kenneth D. Lane, and C. Quigg. Super Collider Physics. *Rev. Mod. Phys.*, 56:579–707, 1984. [Addendum: Rev. Mod. Phys.58,1065(1986)].

[120] U. Baur, I. Hinchliffe, and D. Zeppenfeld. Excited Quark Production at Hadron Colliders. *Int. J. Mod. Phys.*, A2:1285, 1987.

[121] J. Bijnens, P. Eerola, M. Maul, A. Mansson, and T. Sjostrand. QCD signatures of narrow graviton resonances in hadron colliders. *Phys. Lett.*, B503:341–348, 2001.

[122] Jonathan Bagger, Carl Schmidt, and Stephen King. Axigluon Production in Hadronic Collisions. *Phys. Rev.*, D37:1188, 1988.

[123] R. S. Chivukula, Andrew G. Cohen, and Elizabeth H. Simmons. New strong interactions at the Tevatron? *Phys. Lett.*, B380:92–98, 1996.

[124] Bogdan A. Dobrescu and Felix Yu. Coupling-mass mapping of dijet peak searches. *Phys. Rev.*, D88(3):035021, 2013. [Erratum: Phys. Rev.D90,no.7,079901(2014)].

[125] Chase Shimmin and Daniel Whiteson. Boosting low-mass hadronic resonances. *Phys. Rev.*, D94(5):055001, 2016.

[126] Haipeng An, Xiangdong Ji, and Lian-Tao Wang. Light Dark Matter and Z' Dark Force at Colliders. *JHEP*, 07:182, 2012.

[127] Patrick J. Fox, Jia Liu, David Tucker-Smith, and Neal Weiner. An Effective Z'. *Phys. Rev.*, D84:115006, 2011.

[128] Richard W. Robinett and Jonathan L. Rosner. Prospects for a Second Neutral Vector Boson at Low Mass in SO(10). *Phys. Rev.*, D25:3036, 1982. [Erratum: Phys. Rev.D27,679(1983)].

[129] Paul Langacker, Richard W. Robinett, and Jonathan L. Rosner. New Heavy Gauge Bosons in p p and p anti-p Collisions. *Phys. Rev.*, D30:1470, 1984.

[130] Matthew R. Buckley, Dan Hooper, and Jonathan L. Rosner. A Leptophobic Z' And Dark Matter From Grand Unification. *Phys. Lett.*, B703:343–347, 2011.

[131] Marcela Carena, Alejandro Daleo, Bogdan A. Dobrescu, and Timothy M. P. Tait. Z' gauge bosons at the Tevatron. *Phys. Rev.*, D70:093009, 2004.

[132] CDF Collaboration. Search for High Mass Resonances Decaying to Muon Pairs in $\sqrt{s} = 1.96$ TeV $p\bar{p}$ Collisions. *Phys. Rev. Lett.*, 106:121801, 2011.

[133] Robert Foot, Girish C. Joshi, and H. Lew. Gauged Baryon and Lepton Numbers. *Phys. Rev.*, D40:2487–2489, 1989.

[134] Alfredo Aranda and Christopher D. Carone. Limits on a light leptophobic gauge boson. *Phys. Lett.*, B443:352–358, 1998.

[135] Felix Yu. A Z' Model for the CDF Dijet Anomaly. *Phys. Rev.*, D83:094028, 2011.

[136] J. Alwall, R. Frederix, S. Frixione, V. Hirschi, F. Maltoni, O. Mattelaer, H. S. Shao, T. Stelzer, P. Torrielli, and M. Zaro. The automated computation of tree-level and next-to-leading order differential cross sections, and their matching to parton shower simulations. *JHEP*, 07:079, 2014.

[137] Torbjorn Sjostrand, Stephen Mrenna, and Peter Z. Skands. PYTHIA 6.4 Physics and Manual. *JHEP*, 05:026, 2006.

[138] J. de Favereau, C. Delaere, P. Demin, A. Giammanco, V. Lemaître, A. Mertens, and M. Selvaggi. DELPHES 3, A modular framework for fast simulation of a generic collider experiment. *JHEP*, 02:057, 2014.

[139] David Krohn, Jesse Thaler, and Lian-Tao Wang. Jet Trimming. *JHEP*, 02:084, 2010.

[140] ATLAS Collaboration. Study of inclusive isolated-photon production in pp collisions at $\sqrt{s} = 13$ TeV with the ATLAS detector. ATL-PHYS-PUB-2015-016, 2015.

[141] ATLAS Collaboration. Search for new light resonances decaying to jet pairs and produced in association with a photon or a jet in proton–proton collisions at $\sqrt{s} = 13$ TeV with the ATLAS detector. ATLAS-CONF-2016-070, 2016.

[142] Search for light vector resonances decaying to quarks at $\sqrt{s} = 13$ TeV. Technical Report CMS-PAS-EXO-16-030, CERN, Geneva, 2016.

[143] James Dolen, Philip Harris, Simone Marzani, Salvatore Rappoccio, and Nhan Tran. Thinking outside the ROCs: Designing Decorrelated Taggers (DDT) for jet substructure. *JHEP*, 05:156, 2016.